LOAD-CARRYING AND ENERGY-DISSIPATION CAPACITIES OF ULTRA-HIGH-PERFORMANCE CONCRETE UNDER DYNAMIC LOADING

A Thesis
Presented to
The Academic Faculty

by

Jonathan J. Buck

In Partial Fulfillment
of the Requirements for the Degree
Master of Science in Mechanical Engineering

Georgia Institute of Technology
May 2012

LOAD-CARRYING AND ENERGY-DISSIPATION CAPACITIES OF ULTRA-HIGH-PERFORMANCE CONCRETE UNDER DYNAMIC LOADING

Approved by:

Dr. Min Zhou, Advisor
School of Mechanical Engineering
Georgia Institute of Technology

Dr. David McDowell
School of Mechanical Engineering
Georgia Institute of Technology

Dr. Beverly DiPaolo
Army Corps of Engineers Engineer Research and Development Center

Date Approved: March 26, 2012

DEDICATION

To my parents, for exemplifying diligence and commitment

and for instilling in me a lifelong love of learning.

ACKNOWLEDGMENTS

Foremost among those whom I would like to recognize is my advisor, Dr. Min Zhou. His tutelage has been essential to the successful completion of this thesis. Between classroom lectures and office meetings, he has made me a better thinker, a better writer, and a better researcher. In short, he has made me a better engineer.

I owe Dr. David McDowell many thanks for his outside opinion and reviews of my journal papers. I would also like to thank Dr. Beverly DiPaolo for agreeing to be a member of my reading committee. It has been a privilege to work with the Army Corps of Engineers at the forefront of such a promising technology as UHPC. This work was sponsored by the U.S. Department of Homeland Security, Science and Technology Directorate, Infrastructure Protection and Disaster Management Division: Ms. Mila Kennett, Program Manager. The research was performed under the direction of Dr. Beverly P. DiPaolo, Engineer Research and Development Center (ERDC), U.S. Army Corps of Engineers. Permission to publish was granted by the Director, Geotechnical and Structures Laboratory, ERDC. Approved for public release; distribution is unlimited.

Finally, I would like to acknowledge my colleagues, Brett Ellis and Chris Lammi, whose support has been invaluable throughout this process. Thank you for your technical support and for your moral support.

TABLE OF CONTENTS

LIST OF TABLES

LIST OF FIGURES

NOMENCLATURE

2D	Two-dimensional
3D	Three-dimensional
Abaqus® FEA	A commercial suite of applications for finite element analysis and computer-aided engineering. It consists of Abaqus/CAE®, Abaqus/CFD®, Abaqus/Standard®, and Abaqus/Explicit®. It can be used for material response simulations.
CFEM	Cohesive Finite Element Method
E_{total}	Total energy dissipation
E_d	Energy dissipated through interface damage and fracture
E_f	Energy dissipated through friction between fractured interfaces
E_p	Energy dissipated through plastic deformation
GPa	Gigapascal
h	A parameter used to relate energy-dissipation and load-carrying capacities in microstructure-performance relation maps
Matlab®	A commercial software platform for mathematical calculations, code development, and data processing
t_n	Traction component in the normal direction
UHPC	Ultra-High-Performance Concrete
$V_f{}^a$	Volume fraction of aggregate
$V_f{}^f$	Volume fraction of fibers
$V_f{}^p$	Volume fraction of porosity

SUMMARY

The load-carrying and energy-dissipation capacities of ultra-high-performance concrete (UHPC) under dynamic loading are evaluated in relation to microstructure composition at strain rates on the order of 10^5 s^{-1} and pressures of up to 10 GPa. Analysis focuses on deformation and failure mechanisms at the mesostructural level. A cohesive finite element framework that allows explicit account of constituent phases, interfaces, and fracture is used. The model resolves essential deformation and failure mechanisms in addition to providing a phenomenological account of the effects of the phase transformation. Four modes of energy dissipation are tracked, including pressure-sensitive inelastic deformation, damage through the development of distributed cracks, interfacial friction, and energy released through phase transformation of the quartz silica constituent. Simulations are carried out over a range of volume fractions of constituent phases to quantify trends that can be used to design materials for more damage-resistant structures. Calculations show that the volume fractions of the constituents have more influence on the energy-dissipation capacity than on the load-carrying capacity, that inelastic deformation is the source of over 70% of the energy dissipation, and that the presence of porosity changes the role of fibers in the dissipation process. The results also show that the phase transformation has a significant effect on the load-carrying and energy-dissipation capacities of UHPC for the conditions studied. Although transformation accounts for less than 2% of the total energy dissipation, the phase transformation leads to a twofold increase in the crack density and yields nearly an 18% increase to the overall energy dissipation. Microstructure-behavior relations are established to facilitate materials design and tailoring for target-specific applications.

CHAPTER I

INTRODUCTION

Ultra-high-performance concrete (UHPC) is a relatively new and advanced building material that provides several advantages over conventional concrete. Benefits include significantly enhanced ductility and energy-absorption capabilities [1-4] and compressive strengths in excess of 150 MPa and flexural strengths of over 200 times those of conventional concrete [5]. These attributes are possible because UHPC has several unique characteristics that set it apart from more conventional forms of concrete, including finer quartz sand, a lower water-to-cement ratio, and the presence of superplasticizers and fine ductile metal or polymer fibers that are intended to provide protection against a variety of threat scenarios, including blast and impact [5]. Designing UHPC structures that are resilient to such extreme loading events requires that the material have high strength, the capacity to dissipate much of the imparted energy, and the capability to attenuate the stress caused by the loading. However, it is not clear how the characteristics of UHPC at the microstructural level determine these attributes. In particular, the effects of the constituent volume fractions on load-carrying and energy-dissipation capacities under high-rate loading have not been systematically quantified using realistic micromechanical models. Complicating the issue is the fact that the intense loading regimes of the threats against which UHPC structures are intended to protect lead to elevated temperatures and pressures. Under such conditions, the material constituents can change phase, which can drastically alter the dynamic response of the material. Understanding the mechanical behavior alone, however, is not enough to characterize a material in these loading regimes. Dynamic loading of UHPC is inherently a coupled multiphysics process involving mechanical, thermal, and phase transformation

behaviors. Establishing these relationships is important, as the relations can be used to tailor UHPC structures to mitigate specific threats.

The large number of design variables at the microstructural level - such as volume fractions of constituent phases, microstructure morphology, constituent size scales, constituent behaviors, and interfacial bonding strength - pose a challenge in exploring microstructure-property/response relations. Developing comprehensive structure-property relations, however, requires that these variables and their interactions be analyzed. Such relations should account for mechanical, thermal, and phase transformation behaviors of the constituents of UHPC. The mechanical aspects - including fracture, friction, and bulk granular flow - lead to internal temperature rises within a UHPC structure and hydrostatic pressures on the order of multiple GPa. These internal temperature increases and high pressures within UHPC can induce phase transformations in the constituents [6]. One such transformation is the solid-state transformation of quartz from the α-quartz phase to the coesite phase. Increased temperature can also lead to thermal softening of the constituents. Phase transformations can lead to stiffness and density changes, as well as additional fracture that can lead to further dissipation and temperature increases, which in turn alter the mechanical behavior. This interaction among mechanical, thermal, and phase transformational processes during dynamic loading of UHPC ultimately determines its load-carrying and energy-dissipation capacities. Properly accounting for the coupling between these processes in the regime of dynamic loading environments can provide for a more complete assessment of the load-carrying and energy-dissipation capacities. Because UHPC is a complex heterogeneous material, which, like ordinary forms of concrete, contains large amounts of quartz sand [1], it is of interest to account for these behaviors to better understand and take advantage of such mechanisms. For example, to most effectively tailor

the energy-dissipation capacity of UHPC structures and enhance their survivability under extreme loading environments (e.g., blast and impact), the fundamental processes that give rise to energy dissipation must be understood.

The influence of microstructure can be investigated using experimental methods and/or numerical techniques. The use of experimental methods is expensive and lengthy for such complex systems because the number of experiments needed for such a task can quickly grow beyond allowable financial and time constraints. Additionally, deformation processes involved in the dynamic response of UHPC - including distributed microcracking, friction, and granular flow - are inherently coupled phenomena that are difficult to fully capture separately using experimental methods. Nonetheless, these processes and their interactions must be quantified to tailor materials for specific applications.

Numerical simulations offer a useful means for establishing microstructure-performance relations. Much of the published literature involving numerical simulations of concrete implements homogenized phenomenological constitutive relations on the macrostructural scale. For example, Mroz and Angelillo developed a rate-dependent model for concrete [7]. The model makes use of a damage surface with an associated flow rule to account for stiffness degradation. Voyiadjis and Taqieddin developed an elasto-plastic damage model for concrete materials that uses the crack density to model the degradation in the elasticity tensor [8]. The model is capable of reproducing the post-failure softening behavior that is representative of concrete. A similar model was also developed by Fanella and Krajcinovic [9]. A number of other hydrocode models are available for simulating the nonlinear dynamic responses of concrete structures [10].

Mesoscale simulations that fully account for the heterogeneous nature of concrete can help explain the microscale processes that give rise to the observed structural response

on the macroscale. Park, Xia, and Zhou [11] conducted numerical simulations at the mesoscale using a fully dynamic finite element model to systematically study the effect of aggregate volume fraction on the strength and energy-dissipation capacity of plain concrete. Their micromechanical model explicitly accounts for the two-phase structure of cementitious matrix and quartz aggregate of plain concrete. The simulations concerned strain rates on the order of 10^4 s^{-1} and hydrostatic pressures up to 1.5 GPa. The results showed that an aggregate volume fraction of 42% leads to a 15% improvement in energy-dissipation capacity and a 30% enhancement in strength as compared to plain mortar. Aragao et al. [12] also conducted simulations using a cohesive finite element model to analyze fracture and failure in concrete at the microstructural level in which the two-phase structure of cementitious matrix and quartz aggregate is explicitly modeled. Cohesive traction and fracture energy parameters are calibrated in a manner so as to allow the model to accurately represent experimental data from quasi-static tensile tests. Xu, Hao, and Li [13] performed a similar study involving a mesoscale numerical model of fiber-reinforced concrete that provides explicit account of the matrix, aggregate, and fiber phases. The study considered the effects of aggregate and fiber size distribution, as well as fiber volume fraction, on the dynamic compressive strength of fiber-reinforced concrete. The results showed that fiber volume fractions in the range of 0.6% to 1.8% do not appreciably change the compressive dynamic inflation factor (i.e., at a given strain rate, dynamic compressive strength is independent of fiber content).

Lammi, McDowell, and Zhou [14] investigated the dynamic fracture and dissipation behavior of concrete at several levels of hierarchy of microstructure/mesostructure using a cohesive finite element model that accounts for crack formation and frictional dissipation at crack faces. The nominal strain rate considered was on the order of 10^3 s^{-1}. Quartz aggregate

and porosity were explicitly modeled, along with the interface between the phases. The volume fractions of quartz and porosity were in the ranges of 0 - 40% and 0 - 5%, respectively. The results showed that the concrete with 40% aggregate by volume has a load-carrying capacity that is up to 12.2% higher than that of pure matrix without aggregate. A porosity level of 5% decreases the load-carrying capacity by up to 10.9%. Porosity is also found to have the most significant effect on energy dissipation by enhancing plastic deformation.

Ellis, McDowell, and Zhou [15] conducted numerical simulations of 3D microstructures with explicit resolution of porosity and steel fibers within a cementitious matrix. The interface between fibers and matrix was also explicitly modeled. At strain rates of 5×10^{2} - 10^{3} s^{-1}, increasing the fiber volume fraction from 0% to 2% increased the load-carrying capacity by up to 19%. The energy dissipation depended most significantly on the fiber volume fraction. In contrast, porosity had only a minor influence on energy dissipation.

Other studies have been conducted to account for temperature- and pressure-dependent properties in concrete, but the focus of such work has been either on thermal and mass transport properties [16] or on the static mechanical behavior [17-20]. More recent work has attempted to bridge the gap between mass transport properties and mechanical properties by simulating the damage initiation in UHPC exposed to rapid heating [21].

A number of issues have yet to be addressed. First and foremost, there has not been a thorough and systematic characterization of the dynamic behavior of UHPC. In particular, the material performance in relation to the volume fractions of constituents has not been investigated over a sufficiently wide range. Numerical simulations have not considered the essential deformation mechanisms - including fracture, friction, and inelastic granular flow - that occur at the microstructural level. There is a lack of understanding on how these

microstructural-level mechanisms affect macroscopic responses of the overall composites. Many of the analytical models in the open literature developed to characterize these relationships require an excessive number of material parameters, some of which have no basis in the physical processes underlying the material behavior [22]. Consequently, these models are often applicable only to relatively narrow ranges of compositions and loading conditions specific to the experiments upon which the phenomenological constitutive relations are based [23]. Additionally, there have been no studies on the attenuation of stress waves as they traverse heterogeneous UHPC microstructures. There have also been no studies on the relative contributions of mechanisms for energy dissipation as a stress wave propagates through the structure. Also, the constituents in UHPC are known to undergo phase transformations under conditions with high temperatures and high pressures resulting from loading of sufficient magnitudes. In particular, at pressures above 2.35 GPa, the quartz in concrete undergoes a phase transformation from α-quartz to coesite, which involves a volume change of 8.82%. The effects of such phase transformations of constituents in UHPC on the overall mechanical response of the material have not been quantified. The first part of this thesis focuses on the behavior without phase transformations; the second part analyzes the effect of the pressure-induced α-quartz-to-coesite phase transformation of the quartz aggregate.

In the analysis conducted here, a micromechanical cohesive finite element model (CFEM) is adopted to allow explicit resolution of the constituents in the concrete microstructure, including the cementitious matrix, aggregate, fibers, and voids. The model phenomenologically captures the effects of the α-quartz-to-coesite transformation in quartz silica. The model also allows explicit account of crack formation and frictional interaction between crack surfaces that come into contact under compression. This approach enables

the contributions of different dissipation mechanisms (bulk inelasticity, fracture/crack formation, and interfacial friction) to be tracked and quantified. Additionally, this approach captures the interaction and coupling of the dissipation processes at the microstructural level. The composition of the microstructure is systematically varied over a wide range to delineate the effects of each material constituent. Simulations are carried out at strain rates on the order of 10^5 s^{-1}. The analyses address two primary issues: (1) the correlation between volume fractions of constituent phases and macroscopic response in terms of load carried, stress attenuation, crack formation, and energy dissipated and (2) the effect of the aforementioned phase transformation on the macroscopic response. The results are used to develop microstructure-performance relation maps that can be used to identify desired material design parameters for specific application conditions.

CHAPTER II

CFEM FRAMEWORK

2.1. MICROSTRUCTURE INSTANTIATION

One of the goals of this thesis is to thoroughly characterize the dynamic behavior of UHPC over a wide range of constituent volume fractions. This necessitates a large number of microstructural instantiations. Sixty unique microstructures are generated with idealized 2D morphologies, reflecting all combinations of the aggregate, void, and fiber contents. The parametric range of constituent volume fractions is shown in Figure 1.

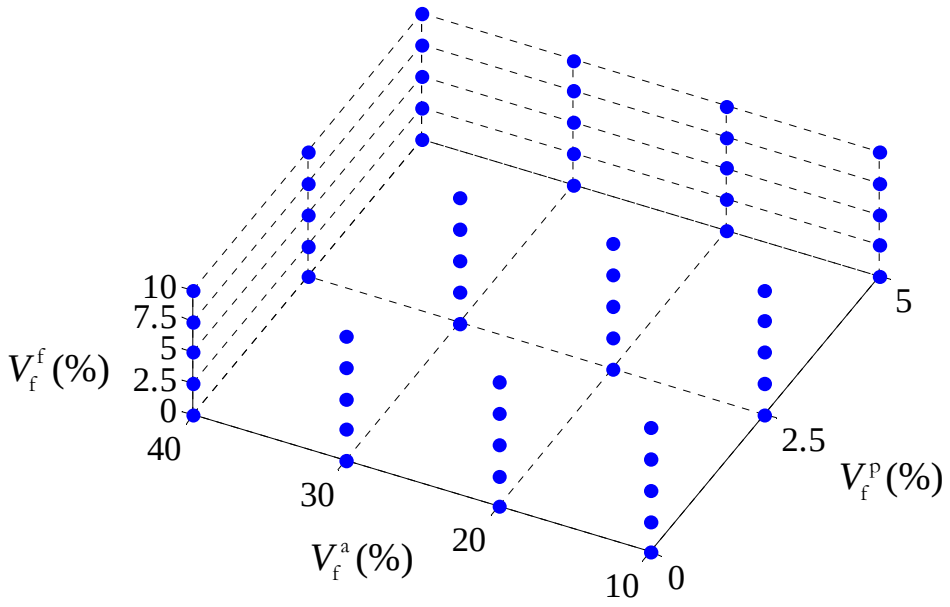

Figure 1. Microstructure design space with combinations of constituent volume fractions analyzed.

The microstructures analyzed are generated in a manner similar to that in Lammi, McDowell, and Zhou [14]. The purpose of this study is to quantify the load-carrying and energy-dissipation capacities of UHPC as functions of the volume fractions of phases, rather than phase size or size distribution. Consequently, each of the phases has a fixed size with no deviation, as shown in Table 1. The fibers, idealized as ellipses in 2D, are given a constant ellipticity ratio of 5:1. The microstructure samples are 5 × 20 mm. These constituent volume fractions and sizes are typical of UHPC fabricated at ERDC and other facilities around the world.

Table 1. Diameters of quartz, porosity, and fibers used for all microstructures in the numerical simulations.

Phase	Diameter (μm)
Quartz	600
Porosity	100
Fiber	200

2.2. CONSTITUTIVE RELATIONS

2.2.1. Cementitious Matrix

Cementitious materials are both pressure-sensitive and rate-sensitive, so the constitutive relation used must be able to capture both aspects of the behavior. In this study, the Drucker-Prager model is used for the cementitious matrix [24]. The Drucker-Prager relation assumes the yield condition

$$F = t - p\tan(\beta) - d \le 0, \tag{1}$$

where

$$t = \frac{1}{2} q \left[1 + \frac{1}{K} - \left(1 - \frac{1}{K} \right) \left(\frac{r}{q} \right)^3 \right]. \tag{2}$$

In the above equations, p is the hydrostatic pressure; β is the internal friction angle in the meridional stress plane; d is the yield stress of the material under pure shear; q is the von Mises equivalent stress, given by $q = \sqrt{\frac{3}{2}\mathbf{S}:\mathbf{S}}$; K is the ratio between the yield stress in triaxial tension and the yield stress in triaxial compression; and r is the third invariant of the deviatoric stress, given by $r = \sqrt[3]{\frac{9}{2}\mathbf{S}\cdot\mathbf{S}:\mathbf{S}}$. In the preceding relations, $\mathbf{S}$ is the deviatoric stress tensor. Parameter K allows for tension-compression asymmetry on any arbitrary π-plane. To ensure a convex yield surface, the value of K is restricted to the range $0.778 \le K \le 1.0$. Setting $K = 1$ removes the dependence on the third invariant of the deviatoric stress, and Equation (1) reduces to the classical Drucker-Prager yield criterion [25]. Furthermore, when $K = 1$ and $\beta = 0$, Equation (1) reduces to the von Mises yield criterion.

Because cementitious paste exhibits dilatation and is a non-associative material, the yield function F does not serve as the plastic flow potential. Instead, a scalar flow potential G is chosen such that

$$G = t - p\tan(\psi), \tag{3}$$

where ψ is the dilation angle. After yielding, a material with non-associated flow has the rate of plastic deformation tensor

$$\mathbf{D}^p = \frac{\dot{\bar{\varepsilon}}^p}{c} \frac{\partial G}{\partial \boldsymbol{\sigma}}, \tag{4}$$

where $\dot{\bar{\varepsilon}}^{pl}$ is the equivalent plastic strain rate, defined by

$$\dot{\bar{\varepsilon}}^{pl} = \sqrt{\frac{2}{3}\mathbf{D}^p : \mathbf{D}^p}, \tag{5}$$

and

$$c = 1 - \frac{1}{3}\tan\psi \,. \tag{6}$$

The values used for the Drucker-Prager constitutive relation in this study are provided in Table 2 [11].

Table 2. Parameters used in Drucker-Prager constitutive relation.

Density (g/cm^3)	2.4
Elastic Modulus (GPa)	22.9
Poisson's Ratio	0.2
Quasi-Static Compressive Strength (MPa)	40
Friction Angle β (degrees)	28
Dilation Angle ψ (degrees)	20
K	0.8

2.2.2. Quartz Aggregate

The phase diagram for quartz is shown in Figure 2 [26]. At ambient conditions, quartz exists as α-quartz, which exhibits a trigonal crystal structure [27]. Above a pressure of 2.35 GPa and at ambient temperature, quartz undergoes a solid-state phase transformation to coesite, which exhibits a monoclinic crystal structure. This transformation is accompanied by an 8.82% decrease in volume [28] and a 0.45% decrease in internal energy [29]. Coesite has an enthalpy of formation of -907.25 kJ/mol [30]. Although quartz contracts upon

transformation into coesite, the transformation is associated with a loss in crystallographic symmetry. This is a consequence of the change of position of SiO_2 polyeders within the second coordination sphere [31]. In the first part of this thesis, which investigates the effect of microstructure alone on the dynamic response of UHPC, the quartz aggregate is assigned rate-independent linear elastic properties with the elastic modulus and Poisson's ratio given above. In the second portion of this thesis, where the effect of phase transformation is assessed, a phenomenological model of the α-quartz-to-coesite transformation is employed as described below. This phenomenological model considers only the change in volume, and the transformation is assumed to be isothermal.

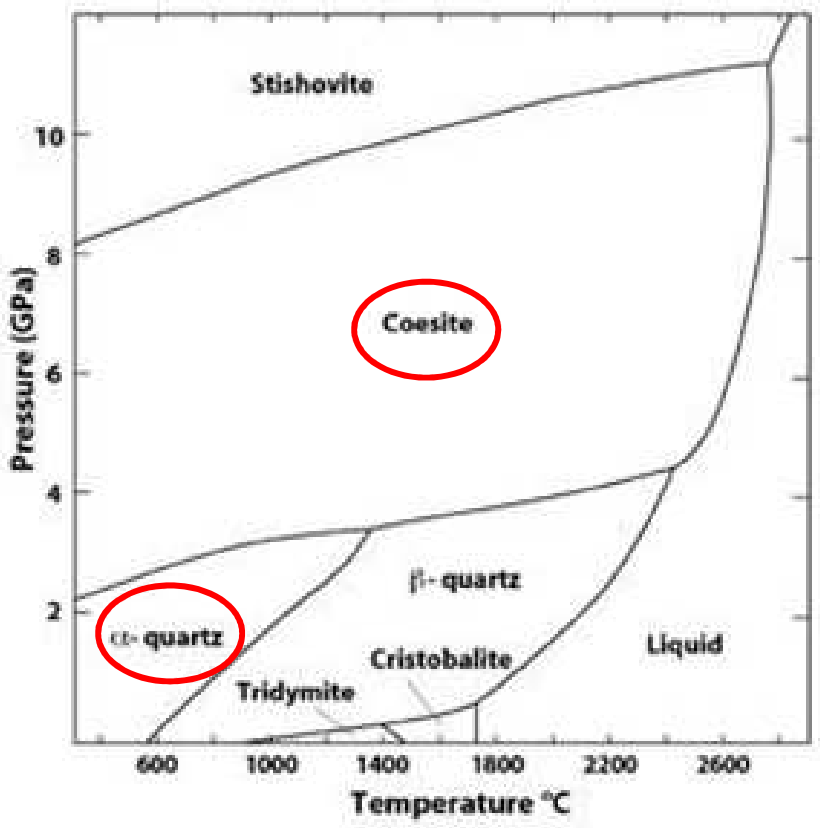

Figure 2. Phase diagram for quartz with the two phases of interest to this thesis circled in red [26].

Due to the limited symmetry of trigonal and monoclinic crystals, the crystalline natures of α-quartz and coesite dictate that they are anisotropic. However, for simplicity, quartz is modeled as an isotropic material through the use of effective isotropic properties obtained using the Voigt-Reuss-Hill averaging technique [32]. This procedure is carried out over a range of pressures so that the material properties used in the simulations reflect relevant pressure-dependence, as shown in Figure 3.

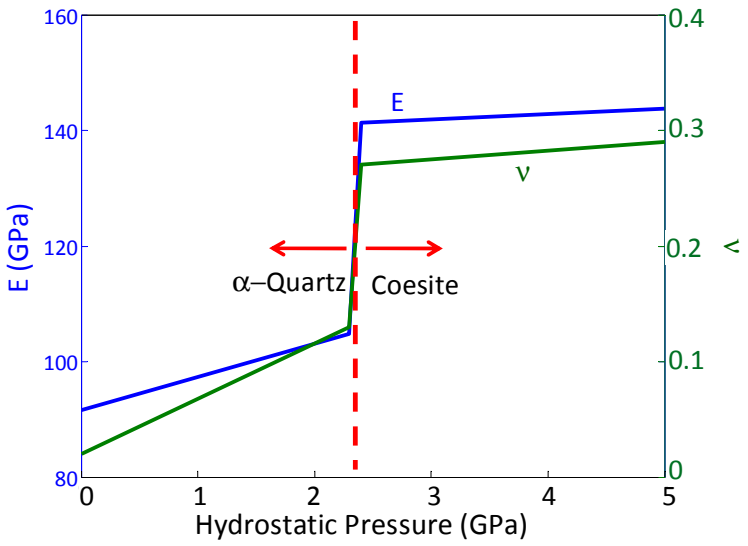

Figure 3. Effective isotropic elastic properties for α-quartz and coesite as functions of hydrostatic pressure.

The first step is the collection of elastic constants for α-quartz and coesite as a function of pressure. Trigonal crystal structures possess six independent elastic constants. Since the data available in the literature [27] extend only up to 1.0 GPa, it is necessary to extrapolate the elastic constants of α-quartz up to the transition pressure of 2.35 GPa using

a linear curve fit. The monoclinic structure of coesite possesses fewer symmetries and requires 13 elastic constants [33].

Next, four sets of values are chosen for the purpose of deriving effective isotropic properties: (1) α-quartz constants at 0.0 GPa, (2) α-quartz constants at 2.35 GPa, (3) coesite constants at 2.35 GPa, and (4) coesite constants at 10.0 GPa. The Voigt-Reuss-Hill averaging technique [32] is used at each pressure to calculate four sets of isotropic properties. Elastic constants pertaining to pressures between points 1 and 2 and between points 3 and 4 in Figure 3 can be found through interpolation.

The first step of the Voigt-Reuss-Hill averaging technique is to calculate the Voigt effective stiffness. The Voigt stiffness assumes uniform strain and provides an upper bound on elastic moduli. The Voigt effective bulk modulus K_V is defined by

$$9K_V = (c_{11} + c_{22} + c_{33}) + 2(c_{12} + c_{23} + c_{31}), \tag{7}$$

where c_{ij} are the components of the elastic stiffness tensor. The Voigt shear modulus G_V is defined as

$$15G_V = (c_{11} + c_{22} + c_{33}) - (c_{12} + c_{23} + c_{31}) + 3(c_{44} + c_{55} + c_{66}), \tag{8}$$

where c_{ij} are the components of the elastic stiffness tensor.

Similarly, the Reuss effective stiffness assumes constant stress and provides a lower bound on the elastic moduli. The Reuss effective bulk modulus K_R is defined as

$$1/K_R = (s_{11} + s_{22} + s_{33}) + 2(s_{12} + s_{23} + s_{31}), \tag{9}$$

where s_{ij} are the components of the elastic compliance tensor. The Reuss shear modulus G_R is defined as

$$15/G_R = 4(s_{11} + s_{22} + s_{33}) - 4(s_{12} + s_{23} + s_{31}) + 3(s_{44} + s_{55} + s_{66}), \tag{10}$$

where s_{ij} are the components of the elastic compliance tensor.

Finally, the Voigt-Reuss-Hill effective bulk modulus is simply the arithmetic mean of the Voigt stiffness and the Reuss stiffness, i.e.,

$$K_{VRH} = \frac{K_R + K_V}{2}. \tag{11}$$

Similarly, the Voigt-Reuss-Hill effective shear modulus is given by

$$G_{VRH} = \frac{G_R + G_V}{2}. \tag{12}$$

Since $K_R \leq K \leq K_V$ and $G_R \leq G \leq G_V$, where K and G are the true values of the stiffness and shear modulus, the Voigt-Reuss-Hill average provides a satisfactory estimate of the elastic properties if the quartz grains are assumed to be isotropic. At the grain level, the quartz aggregate is, of course, anisotropic. However, at the mesostructural level of UHPC, where more interest is in the collective response of the entire structure than in the behavior of any individual grain, isotropy of the quartz aggregate is a reasonable assumption.

The Voigt, Reuss, and Voigt-Reuss-Hill stiffness values are summarized in Table 1. For clarity, the red line demarcates the boundary between α-quartz and coesite. In the last two columns of Table 1, the elastic modulus E and Poisson's ratio ν are calculated using the Voigt-Reuss-Hill bulk modulus and shear modulus according to standard elasticity relationships.

Table 3. Voigt-Reuss-Hill average stiffness values for α-quartz and coesite at key pressure values.

Pressure (GPa)	K_V (GPa)	K_R (GPa)	K_{VRH} (GPa)	G_V (GPa)	G_R (GPa)	G_{VRH} (GPa)	E (GPa)	ν
0.0 (1 atm)	38.11	37.65	37.88	48.07	41.38	44.73	96.29	0.08
2.35	47.37	46.74	47.06	49.55	43.48	46.52	104.96	0.13
2.35	106.37	100.22	103.29	59.47	51.52	55.49	141.19	0.27
10.00	133.21	127.97	130.59	60.97	50.40	55.68	146.26	0.31

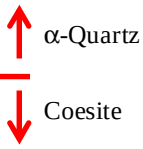

The effective isotropic elastic properties are also shown in Figure 3. As in Table 3, the division between α-quartz and coesite is indicated by a red line. The values between the numbers calculated in Table 3 represent simple linear interpolation.

The transformation of α-quartz into coesite is accompanied by a volume reduction of 8.82% [28]. The literature is not clear as to whether this volume reduction is with respect to the original, undeformed volume or with respect to the elastically deformed configuration just prior to transformation. For the purposes of this study, it is assumed that the 8.82% volume reduction is relative to the volume just prior to the transformation. To model this contraction, a methodology based on finite deformation kinematics has been developed. Assuming a multiplicative decomposition of the deformation gradient, the deformation of a quartz element can be shown schematically in Figure 4.

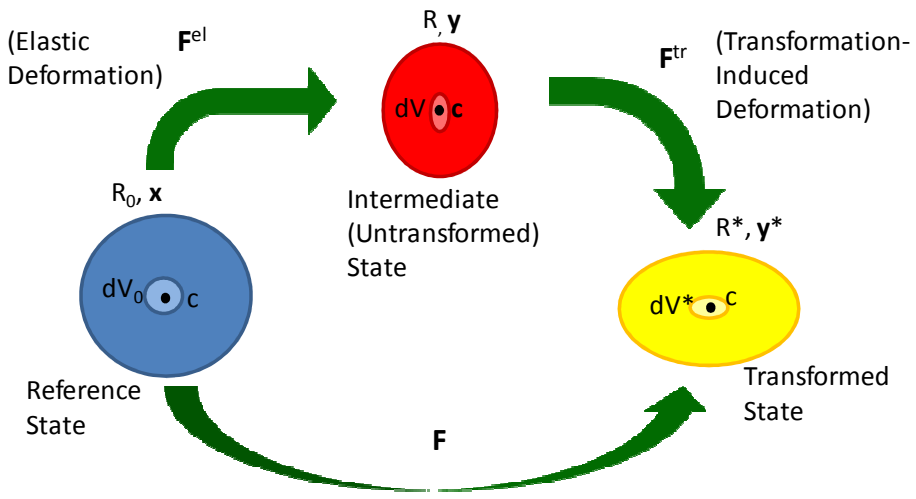

Figure 4. Multiplicative decomposition of deformation gradient accounting for the volume change associated with quartz phase change.

Here, R_0 represents the reference region, c represents the initial center of the quartz element, and **x** represents the initial position. $\mathbf{F}^{el}$ is the deformation gradient associated with the elastic deformation of the quartz. This leads to an intermediate state where R is the intermediate reference region, c is the center of the quartz element in the intermediate state, and **y** is the position. $\mathbf{F}^{tr}$ represents the deformation due to the phase transformation alone and leads to the final state where R^* is the reference region, c is the center, and y is the position. The final state can be reached through the combined deformation gradient $\mathbf{F} = \mathbf{F}^{tr} \cdot \mathbf{F}^{el}$. No other forms of inelastic deformation are considered. Natural quartz crystals do not display appreciable plastic deformation except under the combination of pressures and temperatures in excess of 1.5 GPa and 400 °C, respectively [34]. Furthermore, these data are for quasi-static strain rates. Although pressures in this study are in this regime, temperatures are not; internal temperature increases are not accounted for. Consequently, the failure mode of quartz is likely to be brittle fracture under the high-rate loading of this study.

The volumetric contraction can be described as proportional and isotropic scaling of the coordinates about the center of an element relative to the intermediate state in the form of

$$\mathbf{y}^* = \alpha(\mathbf{y} - \mathbf{c}) + \mathbf{c}. \tag{13}$$

In Equation (13), α represents the amount of scaling in any direction corresponding to the desired volume change. Note that α<1 since the volume decreases upon transformation. The deformation gradient due to the transformation alone is

$$\mathbf{F}^{\mathrm{tr}} = \frac{\partial y^*}{\partial y} = \begin{bmatrix} \alpha & 0 & 0 \\ 0 & \alpha & 0 \\ 0 & 0 & \alpha \end{bmatrix} = \alpha \mathbf{I}\,. \tag{14}$$

To determine α, note that

$$\frac{\mathrm{d}V^*}{\mathrm{d}V} = \det \mathbf{F}^{tr} = \alpha^3 = 0.9118. \tag{15}$$

Therefore, $\alpha = 0.9697.$

The total deformation gradient is

$$\mathbf{F} = (\alpha \mathbf{I}) \cdot \mathbf{F}^{\mathrm{el}} = \alpha \mathbf{F}^{\mathrm{el}}\,. \tag{16}$$

The logarithmic strain with respect to the intermediate state is then

$$\boldsymbol{\varepsilon}^{\mathrm{L}^*} = \ln\left(\mathbf{V}^*\right) = \ln(\alpha \mathbf{V}) = \mathbf{I}\ln(\alpha) + \ln(\mathbf{V}) = \mathbf{I}\ln(\alpha) + \boldsymbol{\varepsilon}^{\mathrm{L}}, \tag{17}$$

where $\mathbf{V}$ is the left stretch tensor. Finally, the Cauchy stress $\boldsymbol{\sigma}$, or the true stress in the final state, is calculated in incremental form according to

$$d\boldsymbol{\sigma} = \mathbf{C} : d\boldsymbol{\varepsilon}^{\mathrm{L}^*}, \tag{18}$$

where **C** is the fourth-order elastic stiffness tensor for quartz. To calculate the Cauchy stress at the $i+1^{th}$ time step, the Cauchy stress increment is simply added to the previous Cauchy stress, i.e.,

$$\boldsymbol{\sigma}^{i+1} = \boldsymbol{\sigma}^{i} + d\boldsymbol{\sigma}. \tag{19}$$

The above constitutive relations are implemented in the Abaqus/Explicit user material subroutine VUMAT [35]. The computational implementation of the VUMAT algorithm is shown in Figure 5. The algorithm starts by initializing all internal state variables, including one to track the phase of quartz elements, which is initialized to zero. This binary state variable is given a value of zero if the element is in the α-quartz phase or a value of one if it is in the coesite phase. The stress is then evaluated using basic equations of linear elasticity, with the values of E and ν interpolated from the α-quartz region of Figure 3, depending on the current hydrostatic pressure. At this point, the procedure checks the current hydrostatic pressure against the transformation pressure. If the current stress state is below the transformation stress, the algorithm returns to α-quartz elastic properties for the next time step. If, however, the current stress state yields a pressure above the transformation stress, the algorithm checks the status of the phase state variable. If the internal state variable is zero, the element must be reaching the transformation pressure for the first time, in which case the transformation-induced volume change must be effected. This is done by calculating the logarithmic strain according to the preceding series of equations. Then the internal state variable tracking the phase is changed from zero to one, signifying that the element has undergone the solid-state phase transformation. At this point, the stress is evaluated by interpolating elastic properties from the coesite region of Figure 3. Returning to the point at which the status of the internal state variable is checked, if the

value is already one, then the element has already undergone phase transformation. In this case, the volume does not need to be reduced again, and the algorithm proceeds directly to the calculation of stress using elastic properties interpolated from the coesite region of Figure 3.

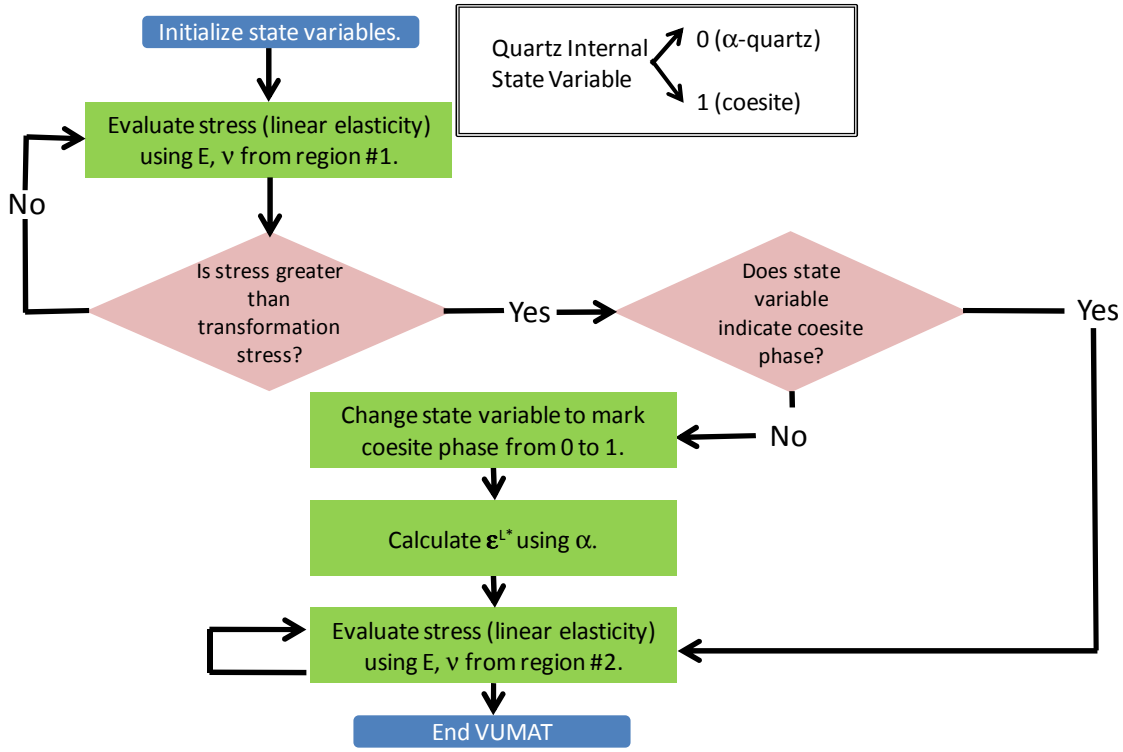

Figure 5. Flowchart summarizing computational implementation of Abaqus/Explicit VUMAT for phenomenological model of quartz phase change.

To verify the proper implementation of the constitutive relations, the behavior of a block of α-quartz under uniform hydrostatic pressure is analyzed. Equal pressure loads are applied to five of the six faces of the cube, with the rear face fixed in the Z direction, creating a hydrostatic compression state of stress in the material. The load increases

gradually from 0 to 9 GPa so that the behavior of the cube can be clearly observed both before and after the transition pressure of 2.35 GPa.

The behavior of the unit cube can be seen in Figure 6(a), which shows the hydrostatic pressure as a function of radial strain. Due to the symmetry of the model, all strain components are equal, as the strain represents the strain in any direction. A key observation from the figure is that when the transition pressure of 2.35 GPa is reached, the hydrostatic pressure remains nearly constant as the transformation occurs and the volume contracts. Below and above this transition pressure, however, the stress is linearly related to the strain, as expected.

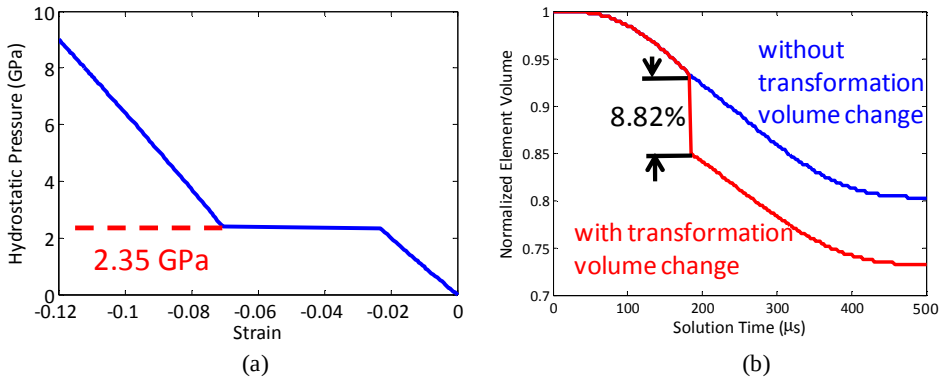

Figure 6. Validation of the phase transformation algorithm through the consideration of the response of a unit cube under hydrostatic pressure: (a) hydrostatic pressure as a function of radial strain and (b) unit cube volume as a function of time with and without transformation.

The change in the element volume can be seen in Figure 6(b), where the normalized element volume is plotted as a function of time. The two curves represent the case without the phase transformation (blue) and with the phase transformation (red). Once the critical transformation pressure is reached, phase transformation occurs and a sudden decrease of 8.82% in volume is seen, indicating the occurrence of the phase transformation.

2.2.3. Steel Fibers

The Johnson-Cook model, which allows for the modeling of the rate-dependent hardening of steel, was used to describe the behavior of the steel fibers. The Johnson-Cook constitutive relation can be expressed as

$$\bar{\sigma}\left(\bar{\varepsilon}^{p},\dot{\varepsilon}^{p},T\right)=\left(A+B\bar{\varepsilon}^{n}\right)\left[1+C\log\left(\frac{\dot{\varepsilon}^{p}}{\dot{\varepsilon}_{0}}\right)\right]\left[1-\left(\frac{T-T_{\text{room}}}{T_{\text{melt}}-T_{\text{room}}}\right)^{m}\right]. \tag{20}$$

Here, A, B, C, and m are material parameters that are calibrated using experimental data [36]. The first expression on the right hand side accounts for strain hardening, the second expression accounts for strain-rate hardening, and the third expression accounts for thermal softening. Model parameters are listed in Table 4. The introduction of reinforcing steel fibers also requires the appropriate calibration of cohesive elements bonding the fibers to the cement matrix. The peak traction and fracture energy of the fiber-cement interface are in line with values taken from experimental data for fiber-reinforced cement [37, 38].

Table 4. Parameters used in Johnson-Cook model for reinforcing steel fibers.

Density (g/cm^3)	7.8
Young's Modulus E (GPa)	203
Poisson's Ratio ν	0.28
A (MPa)	792
B (MPa)	510
n	0.26
C	0.014
T_{room} (K)	300
T_{melt} (K)	1793
m	1.03
$\dot{\varepsilon}_0$ (s^{-1})	1
Specific heat (J/kg-K)	477

2.2.4. Interfaces

Cohesive elements are specified between all bulk elements boundaries with the exception of elements in the fibers, which are assumed to undergo no fracture. The cohesive elements allow for damage initiation and development. A bilinear traction-separation law is adopted to govern the behavior of the cohesive elements [39].

The linear-elastic part of the traction-separation law relates the traction vector **t** to the element stiffness **K** and the separation **u** resulting from the traction vector **t**. This relationship is given by

$$\mathbf{t} = \mathbf{K}\mathbf{u}. \tag{21}$$

The above equation can be expressed in matrix form to indicate coupling between the normal and shear components of the traction-separation relationship, i.e.,

$$\begin{pmatrix} t_n \\ t_s \\ t_t \end{pmatrix} = \begin{bmatrix} K_{nn} & K_{ns} & K_{nt} \\ K_{ns} & K_{ss} & K_{st} \\ K_{nt} & K_{st} & K_{tt} \end{bmatrix} \begin{pmatrix} u_n \\ u_s \\ u_t \end{pmatrix}. \tag{22}$$

Full coupling between normal and shear components in the traction-separation response is represented by the off-diagonal terms. For the purposes of this thesis, however, an uncoupled relation is chosen, i.e.,

$$\begin{pmatrix} t_n \\ t_s \\ t_t \end{pmatrix} = \begin{bmatrix} K_{nn} & 0 & 0 \\ 0 & K_{ss} & 0 \\ 0 & 0 & K_{tt} \end{bmatrix} \begin{pmatrix} u_n \\ u_s \\ u_t \end{pmatrix}. \tag{23}$$

Although the linear-elastic part of the response has no coupling between shear and normal components, damage initiation and evolution have a mixed-mode form. Damage initiation follows the quadratic interaction relationship shown in Equation (24), where t_n is

the normal stress in a cohesive element, t_s and t_t are the shear stresses, and t_n^0, t_s^0, and t_t^0 are, respectively, the critical values of t_n, t_s, and t_t, which represent the cohesive strength. In this thesis, both t_s^0 and t_t^0 are assumed to have the same value. Because it is not physically meaningful for compressive tractions to contribute to damage initiation, only non-negative (tensile) normal tractions are considered in the damage initiation rule. This is indicated by the presence of the Macaulay brackets around t_n. Damage is initiated when

$$\left(\frac{\langle t_n \rangle}{t_n^0}\right)^2 + \left(\frac{t_s}{t_s^0}\right)^2 + \left(\frac{t_t}{t_t^0}\right)^2 = 1. \tag{24}$$

A schematic representation of the bilinear traction-separation law is shown in Figure 7. Loading initially proceeds from point A to point B, at which point softening occurs with increasing strain until failure at a separation of δ.

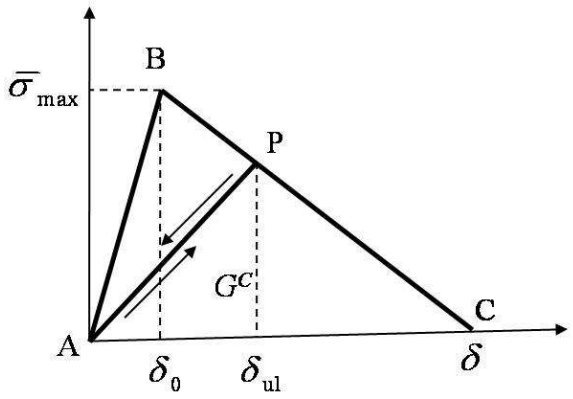

Figure 7. Bilinear traction-separation law for cohesive elements.

Once damage initiates in a cohesive element, the interface follows the mixed-mode fracture criterion of Benzeggagh and Kenane given in Equation (25) [40]. In this relationship,

G_n, G_s, and G_t are the work done by tractions t_n, t_s, and t_t, respectively. G_n^C, G_s^C and G_t^C are the critical fracture energies in the normal and shear directions, respectively. These quantities are used to determine the degree of damage in a cohesive surface pair. For convenience, the critical fracture energies in the two shear directions are treated as equal (i.e., $G_s^C = G_t^C$). The criterion is written as

$$G_n^C + \left(G_s^C - G_n^C\right)\left(\frac{G_s + G_t}{G_n + G_s + G_t}\right)^{\eta} = G^C. \tag{25}$$

There are four interface zones in the model: paste-paste, quartz-quartz, quartz-paste, and fiber-paste. The constitutive behavior of all cohesive elements modeled in this study follows the same constitutive law; however, the calibration of the traction-separation stiffness, the peak traction across the element (t_i^0), and the normal and shear fracture energies (G_n^f and G_s^f) is specific to each type of interface. The parameters for all cohesive relations used in this study are presented in Table 5.

Table 5. Cohesive element properties for each interface.

Material	Cement	Quartz Aggregate	Cement-Aggregate Interface	Cement-Fiber Interface
K_n (TPa)	22.9	96.6	22.9	22.9
$K_{s/t}$ (TPa)	9.5	44.7	9.5	9.5
t_n^0 (MPa)	40.0	50.0	10.0	10.0
$t_{s/t}^0$ (MPa)	25.0	40.0	6.0	6.0
G_n^C (J/m^2)	40.0	15.0	5.0	5.0
$G_{s/t}^C$ (J/m^2)	40.0	15.0	5.0	5.0
η	1.45	1.45	1.45	1.45

As shown in Table 5, the traction-separation stiffness for cohesive elements along interfaces between the phases and within the bulk phases is a factor of 10^3 times the stiffness of the corresponding bulk elements. This choice has two benefits. First, artificial softening of the model is avoided. Second, the work of separation associated with the linear-elastic portion of the cohesive behavior is minimized, ensuring that the bulk of the work is in the fracture energy, providing adequate softening in the cohesive response.

2.2.5. Interfacial Contact and Friction

After the failure of cohesive elements, contact between bulk elements leads to frictional sliding. Contact between element faces is incorporated into the model using a contact algorithm similar to that developed by Camacho and Ortiz [41]. The algorithm identifies free surfaces and fractured surfaces as potential contact surfaces in each time step of the simulation. Nodal coordinates at the end of every time step are used to define master and slave surfaces for the next time step. Nodal displacements are then calculated at the beginning of every time step. The corresponding nodal coordinates are used to check whether nodes of one internally defined surface have penetrated other internally defined surfaces. If penetration is predicted, then penalty forces of sufficient magnitude are applied to the surfaces in the direction of their normal vector such that there is contact between them but no interpenetration. For surfaces that are in contact, the Coulomb friction law governs the interfacial friction force. The coefficient of sliding friction for all interfaces is chosen to be 0.6, a typical value for cement-on-cement sliding [42]. It is assumed that the static and dynamic coefficients of friction are the same.

2.3. COHESIVE FINITE ELEMENT MODEL

Figure 8 illustrates the configuration of the computational model along with the loading and constraint conditions. The particular microstructure shown has 10% aggregate, 2.5% porosity, and 2.5% fibers by volume. Compressive loading is effected by the imposition of a boundary velocity normal to the top surface. For all calculations, the imposed velocity is 1000 m/s, giving rise to a nominal strain rate of 5×10^4 s^{-1} if the deformation in the whole model is uniform. The calculations consider the first 6 μs of deformation, resulting in a total strain of 30% in the vertical direction. Rigid boundary conditions are applied at the lateral sides of the microstructure, allowing the computations to approximate the overall conditions of uniaxial strain with significant lateral confining stresses.

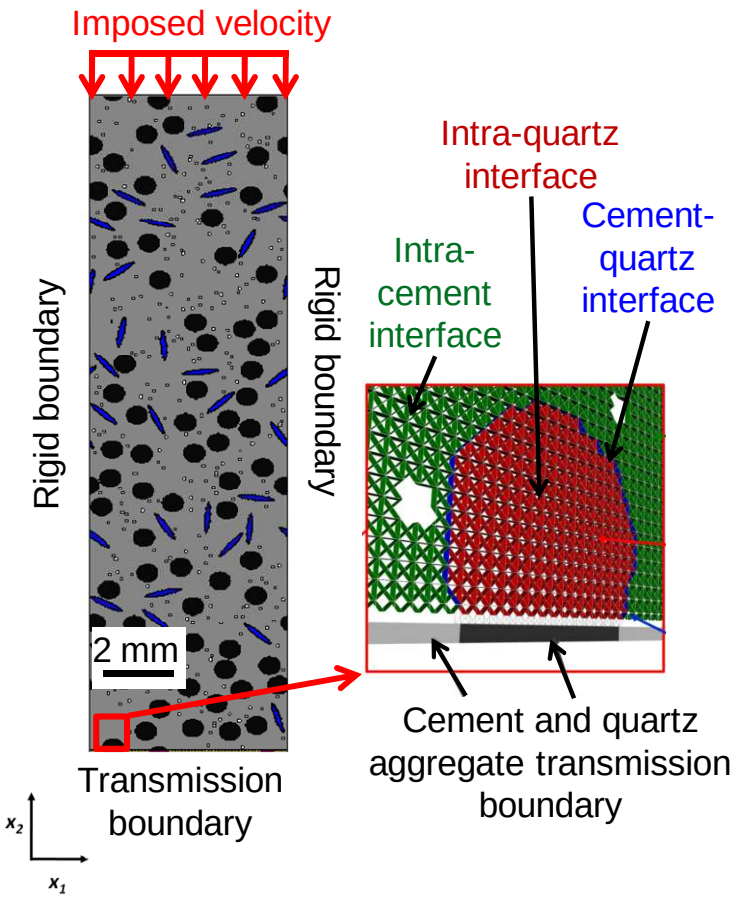

Figure 8. Cohesive finite element model for UHPC microstructures with four constituent phases of UHPC, imposed velocity, periodic boundary conditions, cohesive elements, and infinite elements.

The cohesive finite element model has a mesh resolution of 33.3 μm/element. In the absence of pores, the mesh consists of 360,000 six-noded triangular prism (type C3D6 in Abaqus) bulk elements and 1,438,800 eight-noded (type COH3D8) cohesive elements. Cohesive elements are present at all phase boundaries of all bulk elements; consequently, fracture between the constituent phases can be resolved. Additionally, cohesive elements are present within regions of quartz and matrix bulk elements, allowing for fracture within the quartz and cementitious matrix to be resolved. The cohesive elements also allow fracture

energy and subsequent dissipation through interfacial friction to be analyzed. Infinite elements (type CIN3D8) are specified at the bottom to allow stress waves to pass through the material and minimize reflection back into the microstructure. Despite the presence of this transmission boundary, partial reflections are seen in the calculations because material properties change during deformations and a perfect match of impedance cannot be maintained throughout the duration of the loading events. In this thesis, only data prior to the arrival of the stress wave at the bottom are used; therefore, the possible reflection of the stress is irrelevant.

2.4. Evaluation of Energy Dissipation

Four modes of energy dissipation (damage/fracture, friction, plasticity, and phase transformation) are tracked throughout the deformation process to assess the energy-dissipation capacity of the microstructures. The first three quantities are provided by Abaqus as the output variables ALLDMD, ALLFD, and ALLPD, respectively. In the first portion of this thesis, which investigates the effect of microstructure alone, only these first three modes are considered. In the second portion, which investigates the effect of phase transformation, the energy released by the quartz aggregate upon transformation into coesite is also considered.

The energy dissipated through damage and fracture of interfaces between the phases is defined in Equation (26), where **v** is the relative velocity vector between the pair of surfaces, **t** is the traction vector across the surfaces, and S is the surface of the material in the current configuration. The traction across the cohesive surfaces is determined by the traction-separation law discussed in Section 2.2.4. Only tensile tractions contribute to damage initiation and dissipation in this thesis.

$$E_d = \int_0^t \left(\int_S \mathbf{v} \cdot \mathbf{t} \, dS \right) d\tau \tag{26}$$

After failure of cohesive elements at interfaces, surfaces come into frictional contact, as discussed in Section 2.2.5. This contact generates energy dissipation through friction. The frictional dissipation is defined in Equation (27), where **v** is the relative velocity vector between the pair of surfaces, **t** is the traction vector across the surfaces, and S is the surface over which contact occurs. Although Equations (26) and (27) appear identical, their usage differs in application. Equation (26) pertains to interfaces that have not yet fractured. No frictional dissipation is possible between these surfaces. Equation (27) is applicable to interfaces that have fractured, allowing for surfaces to come into contact.

$$E_d = \int_0^t \left(\int_S \mathbf{v} \cdot \mathbf{t} \, dS \right) d\tau \tag{27}$$

The energy dissipated through inelastic deformation of the bulk constituents is defined in Equation (28), where $\boldsymbol{\sigma}$ is the Cauchy stress tensor, $\dot{\boldsymbol{\varepsilon}}^{\mathrm{p}}$ is the plastic strain rate tensor, and V is the volumetric domain in the reference configuration.

$$E_p = \int_0^t \left(\int_V \boldsymbol{\sigma} : \dot{\boldsymbol{\varepsilon}}^p \, dV \right) d\tau \tag{28}$$

Although friction and inelastic deformation typically generate heat, thermomechanical coupling is not considered in this thesis.

CHAPTER III

RESULTS, ANALYSIS, AND DISCUSSION

After all the microstructures are instantiated, the simulations are performed using the commercial finite element analysis software package Abaqus/Explicit [24].

3.1. EFFECT OF MICROSTRUCTURE

3.1.1. Load-Carrying Capacity

In response to the imposed velocity on the upper surface, a stress wave propagates through the microstructure in the direction parallel to the direction of the imposed velocity. The average normal traction on the upper face of the microstructures (t_n) is taken as a measure of the load carried. The averaging is carried out over all elements having a node on the top face. The traction is averaged at each time step of the simulation to provide a single value of the load-carrying capacity at that time. The length of the microstructure in the x_2 direction allows sufficient time for the stress wave to develop so that an accurate representation of the load-carrying capacity can be captured without introducing an artificial response due to interaction with the transmission boundary on the bottom surface.

Figure 9 shows the normal stress component in the vertical direction in a microstructure with 40% aggregate, 0% porosity, and 10% fibers at three different times in the simulation. The first time is 0.5 μs, which illustrates the initial response of the microstructure. This time is the first point at which stress data are stored in the course of the simulation. The second time is 3.0 μs, which provides a view of the stress in the microstructure at an intermediate time in the simulation. The final time is 6.0 μs. At this point in time, the stress wave has very nearly reached the bottom surface of the

microstructure. The implied wave speed is approximately 3.3 km/s. This value agrees reasonably well with the theoretical longitudinal wave speed in cement paste, which is given by $c_d = \sqrt{E(1-\nu)/(1+\nu)(1-2\nu)\rho} \approx 3.3 km \cdot s^{-1}$. During the next time step in the simulation, the stress wave reaches the bottom boundary and distorts the results. The microstructure discussed here, having 40% aggregate, 0% porosity, and 10% fibers, is the densest microstructure over the range of constituent volume fractions considered and therefore has the highest longitudinal wave speed. As such, the stress wave will also not have reached the bottom surface in any of the other microstructures. A dynamic loading event is an evolutionary process, so there is no single point at which the strength of the material can be defined. However, the proper comparison of 60 unique microstructures necessitates a common point of comparison. The choice of this point is somewhat arbitrary, but is based upon consideration of the propagation of the stress wave through the microstructure as well as the evolution of the traction on the upper surface.

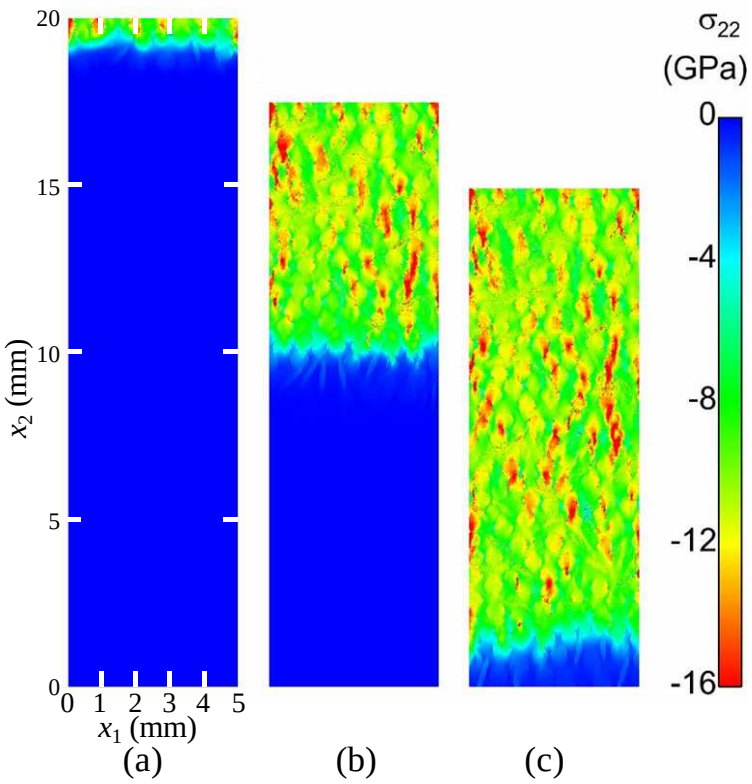

Figure 9. Propagation of stress wave through a microstructure with 40% aggregate, 0% porosity, and 10% fibers at three different times: (a) 0.5 μs, (b) 3.0 μs, and (c) 6.0 μs.

Figure 10 shows the evolution of the average traction on the upper face of a microstructure with 10% aggregate, 0% porosity, and 0% fibers by volume. Two distinct regions can be seen in the response. The first is a linear, rapidly increasing regime. In the second region, where the stress reaches a plateau, granular flow of the cementitious matrix is the dominant deformation mechanism. The microstructures will be compared at 6.0 μs, which provides a comparison during the relatively constant plateau region before the stress wave has reached the bottom surface.

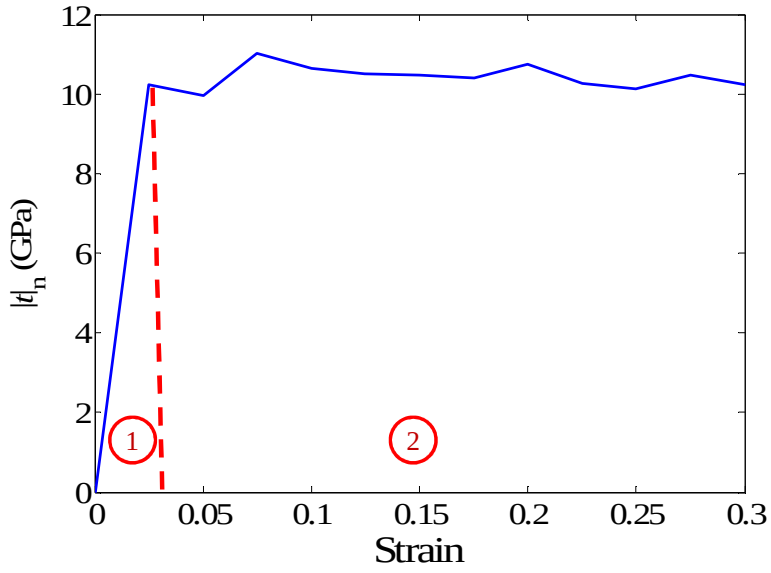

Figure 10. Evolution of the average normal traction on the upper surface showing two distinct stages for a microstructure with 40% aggregate, 10% fibers, and 0% porosity.

The load-carrying capacities for all 60 unique microstructures are shown in Figure 11. Four subplots are shown, each corresponding to a different aggregate volume fraction, to more easily present four-dimensional data. Within each plot, the horizontal axes indicate the fiber and porosity volume fractions. The vertical axis shows the normalized load-carrying capacity. The data are normalized to the load-carrying capacity of a microstructure comprised of 100% cementitious matrix. This baseline value is 7.6 GPa. At any time step within the plateau region mentioned above, the traction on the upper face exhibits some degree of variation due to the heterogeneity of UHPC microstructures. However, over the entire plateau region, the traction is relatively constant. Consequently, the load-carrying capacity shown in Figure 11 is the traction on the upper surface averaged over all time steps in the plateau region. Fibers play a significant role in the load-carrying capacity, while the aggregate and porosity play a lesser role. As expected, the microstructure with the largest

load-carrying capacity has 40% aggregate, 10% fibers, and 0% porosity. This provides a 38% improvement in the load-carrying capacity as compared to 100% cementitious matrix.

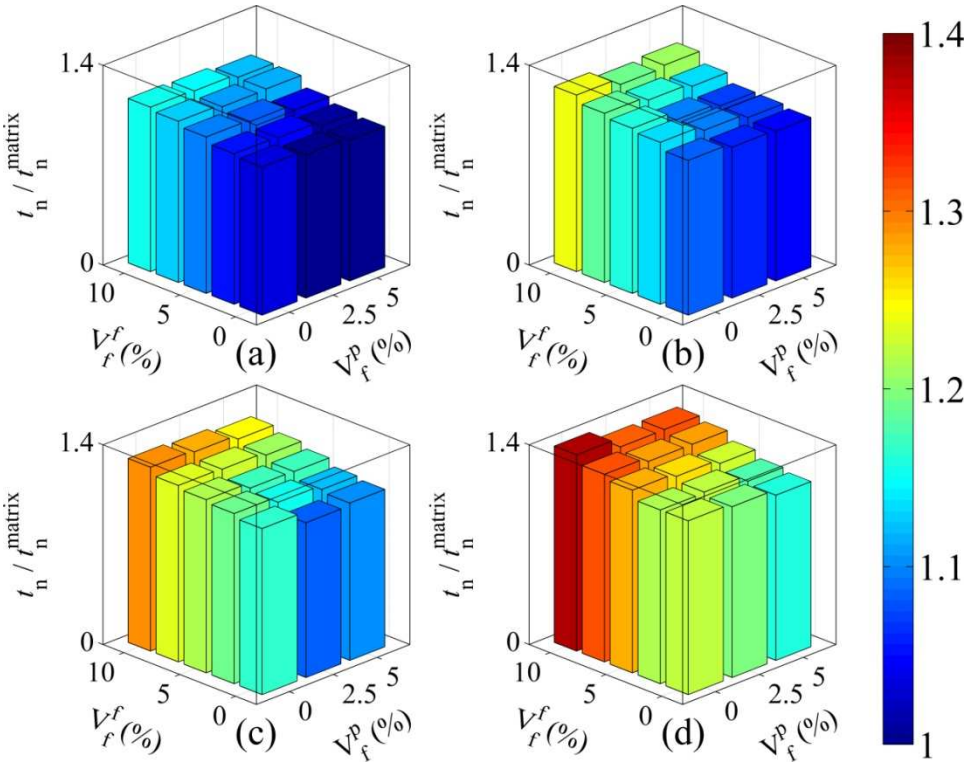

Figure 11. Normalized load-carrying capacity for all microstructures at four different aggregate volume fractions: (a) 10%, (b) 20%, (c) 30%, and (d) 40%. The normalizing factor $t_n^{\text{matrix}} = 7.6$ GPa.

Lammi, McDowell, and Zhou [14] concluded that there is a synergistic effect between the aggregate and porosity whereby the detrimental effect of porosity is compounded when the aggregate volume fraction is largest. No such trend is found in this analysis. Voids do have a measurable, but minor, effect on the load-carrying capacity. For example, a microstructure with 40% aggregate and 10% fibers experiences a 7% decrease in load-carrying capacity as the porosity is increased from 0% to 5%. This illustrates the need

to carefully control porosity in designing UHPC structures. Based on observation of the stress wave as it develops throughout a microstructure, the voids collapse under pressures in the range of 2-3 GPa.

It can be seen here that increasing aggregate and fiber volume fractions increases the load-carrying capacity. Subsequent sections will show that increasing aggregate and fiber volume fractions also increases the energy dissipation. The fact that the load-carrying capacity increases despite the increase in energy dissipation indicates that the damage within the UHPC microstructure does not have a measurable effect on the load-carrying capacity under the loading conditions considered. The foregoing observations suggest that the load-carrying capacity is in reality more of a reaction force at the impact site and that the load carried is primarily determined by the density of a given microstructure. This is illustrated in Figure 12, which shows the normalized load-carrying capacity of all 60 microstructures as a function of the average microstructure density. A clear upward trend in the data can be seen. However, the scatter in the data indicates that density alone does not explain the variation in the results. At a common density, the load-carrying capacity of two different microstructures can vary by as much as 20%. The figure also delineates aggregate volume fraction by color. This illustrates that for a common aggregate volume fraction, the linear trend has significantly less scatter than the entire data set. Because the average density shown on the horizontal axis is calculated as the sum of constituent density weighted by constituent volume fraction, the trends in this figure suggest that a more complex relationship is necessary to relate the load carried to the volume fractions of constituents. This will be discussed further in Section 3.1.3.

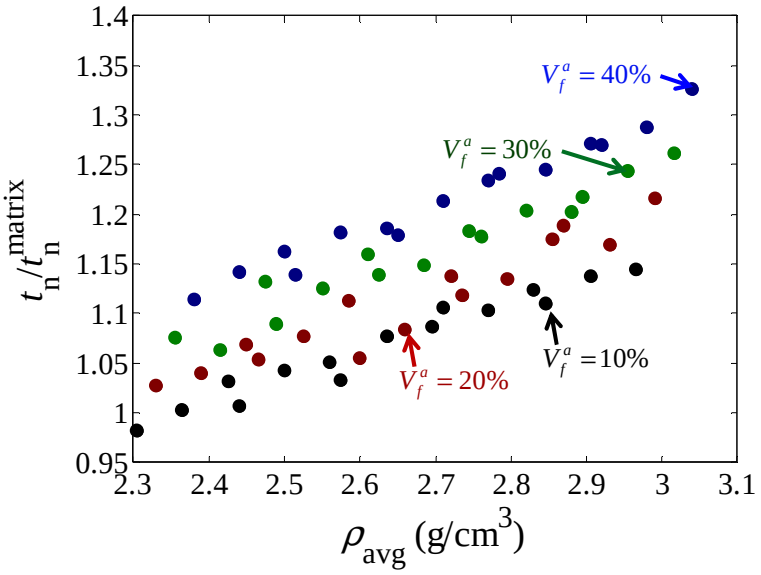

Figure 12. Normalized load-carrying capacity as a function of the overall density of the materials.

The spatial distribution of the stress component in the vertical direction in microstructures at the extremes, or "corners," in Figure 1 of the simulated parametric ranges of microstructures can be seen in the eight plots in Figure 13. This figure shows the stress at 0.5 μs, 2.0 μs , and 4.0 μs. The preceding analysis showed that the load-carrying capacity increases with increasing aggregate and fiber volume fractions, despite the fact that they also serve to increase the energy dissipation as well. However, the load-carrying capacity is measured in this study as the traction on the upper surface of a microstructure. Although there is no attenuation of this load, there may be attenuation within the microstructures. Figure 13, however, shows that there is no appreciable attenuation of the stress wave over the distance analyzed even as it traverses the microstructure. Although there is moment-to-moment fluctuation, the stress remains relatively constant throughout the microstructure. The fluctuation is due to the heterogeneity of the microstructure. Over the length and time

scales considered in this study, the stress throughout a microstructure is governed more by the material's short-term elastic response.

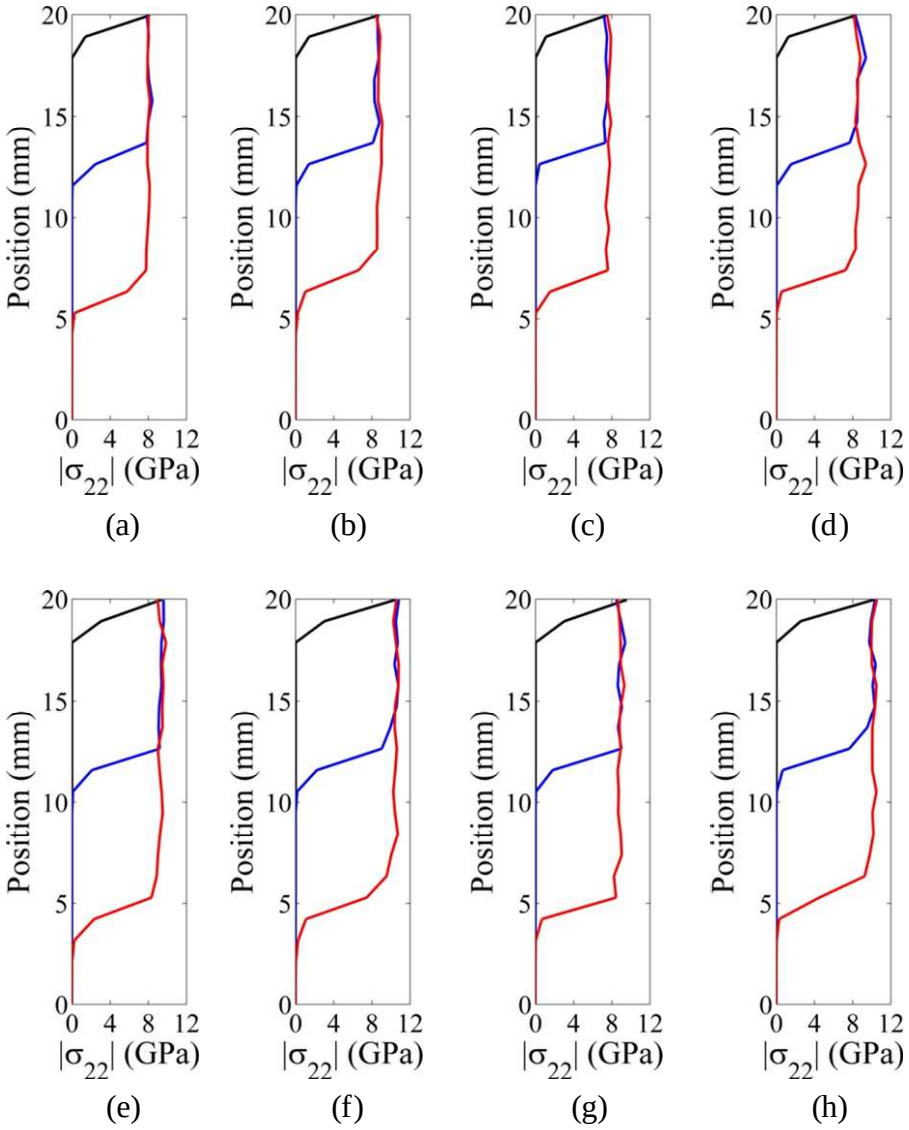

Figure 13. Stress propagation in microstructures at the eight extremes of the design space at 0.5 μs, 2.0 μs, and 4.0 μs: (a) 10% aggregate, 0% porosity, 0% fibers; (b) 10% aggregate, 0% porosity, 10% fibers; (c) 10% aggregate, 5% porosity, 0% fibers; (d) 10% aggregate, 5% porosity, 10% fibers; (e) 40% aggregate, 0% porosity, 0% fibers; (f) 40% aggregate, 0% porosity, 10% fibers; (g) 40% aggregate, 5% porosity, 0% fibers; and (h) 40% aggregate, 5% porosity, 10% fibers.

3.1.2. Energy-Dissipation Capacity

Three modes of energy dissipation are tracked in this set of simulations: plastic dissipation due to inelastic deformation in the steel fibers and granular flow of the cementitious paste, damage due to fracture and distributed cracking, and friction at cracked interfaces.

3.1.2.1. Total Energy Dissipation

The total energy dissipation is the sum of the three modes of energy dissipation, but each mode does not play an equal role. The exact proportion of energy dissipated by each mode depends on the volume fractions of the constituents. However, some general observations can be made. Figures 14(a)-(b) show the energy dissipation components as a function of strain for two microstructures with a common aggregate volume fraction of 20% but different porosity and fiber volume fractions. It can be seen that increasing porosity and fiber volume fractions increases the portion of energy dissipation attributable to friction but decreases the portion attributable to inelastic deformation. Figure 14(a) shows porosity and fiber volume fractions of 0%, while Figure 14(b) shows porosity and fiber volume fractions of 5% and 10%, respectively. The vertical axes on these plots have been normalized such that the sum of the three energy dissipation components is exactly unity at a strain of 0.3. The two plots appear similar, but there are several differences that arise due to the different volume fractions of the constituents. At a strain of 0.3, inelastic deformation, friction, and fracture contribute 88.1%, 11.7%, and 0.2%, respectively, of the total energy dissipation in the first microstructure. In the second microstructure, inelastic deformation, friction, and fracture contribute 84.9%, 15.0%, and 0.1%, respectively, of the total energy dissipation. Although the presence of fibers and porosity is seen here to decrease the portion of energy

dissipation due to inelastic deformation, Section 3.1.2.4 will show that fibers and porosity in fact increase the plastic component of energy dissipation.

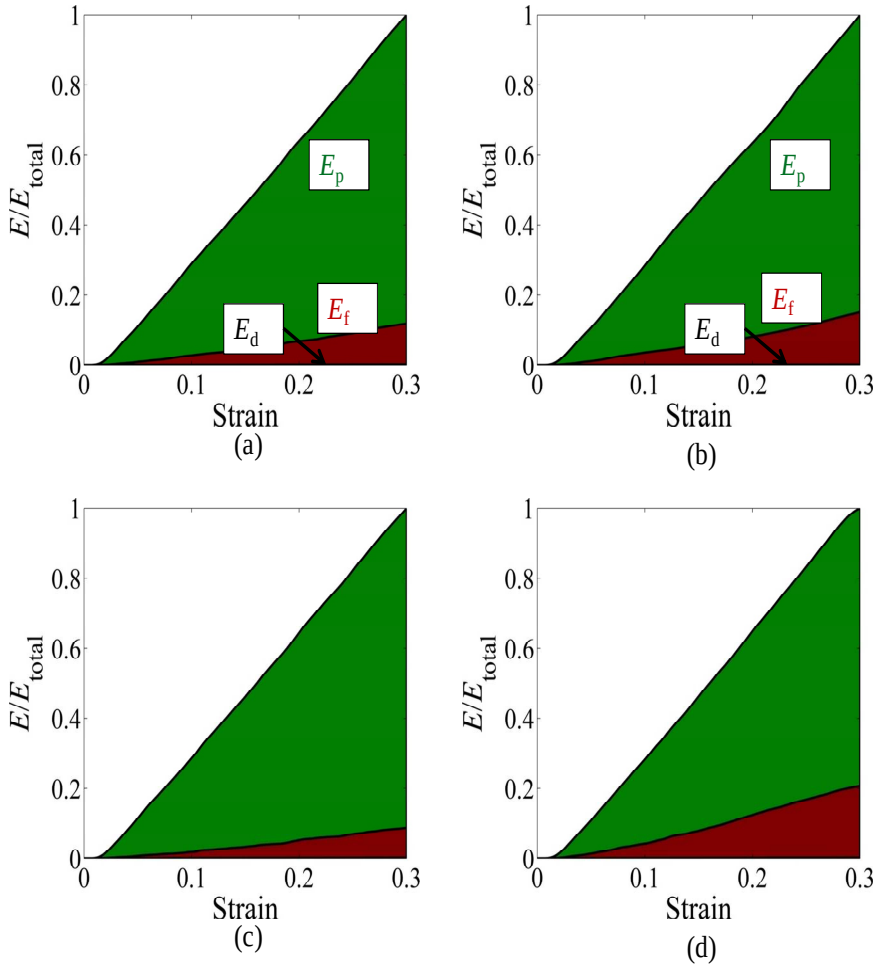

Figure 14. Components of the total energy dissipated as a function of strain for microstructures with (a) 20% aggregate, 0% porosity, 0% fibers; (b) 20% aggregate, 5% porosity, 10% fibers; (c) 10% aggregate, 0% porosity, 0% fibers; and (d) 40% aggregate, 0% porosity, 0% fibers.

Figures 14(c)-(d) show that increasing the aggregate volume fraction increases the portion of energy dissipation attributable to friction but decreases the portion attributable to plastic deformation. Figures 14(c)-(d) also show the energy dissipation components as a

function of strain in two microstructures with common porosity and fiber volume fractions of 0% at two different aggregate levels, 10% and 40%. In the first microstructure, inelastic deformation, friction, and fracture contribute 91.3%, 8.9%, and 0.2%, respectively, of the total energy dissipation. In the second microstructure, inelastic deformation, friction, and fracture contribute 79.2%, 20.6%, and 0.2%, respectively, of the total energy dissipation. In order to increase the energy dissipation of UHPC, emphasis should be placed on enhancing frictional and plastic work in the microstructure. Changing either of these by a given percentage will have a far larger effect on the overall total than changing the damage energy by the same percentage.

Figure 14 shows the evolution of the energy dissipation components in four individual microstructures. Displaying the total energy-dissipation capacity in all 60 microstructures necessitates a more concise format. Figure 15 shows the total energy dissipation capacity in all 60 microstructures. The horizontal axes indicate the fiber and porosity volume fractions. The vertical axis shows the normalized total energy-dissipation capacity. The data are normalized by the total energy dissipation of a baseline case, a microstructure comprised of 100% cementitious matrix. This normalizing factor $E_{\text{total}}^{\text{matrix}} = 135\ \text{MJ/m}^3$. The values correspond to a simulation time of 6.0 μs.

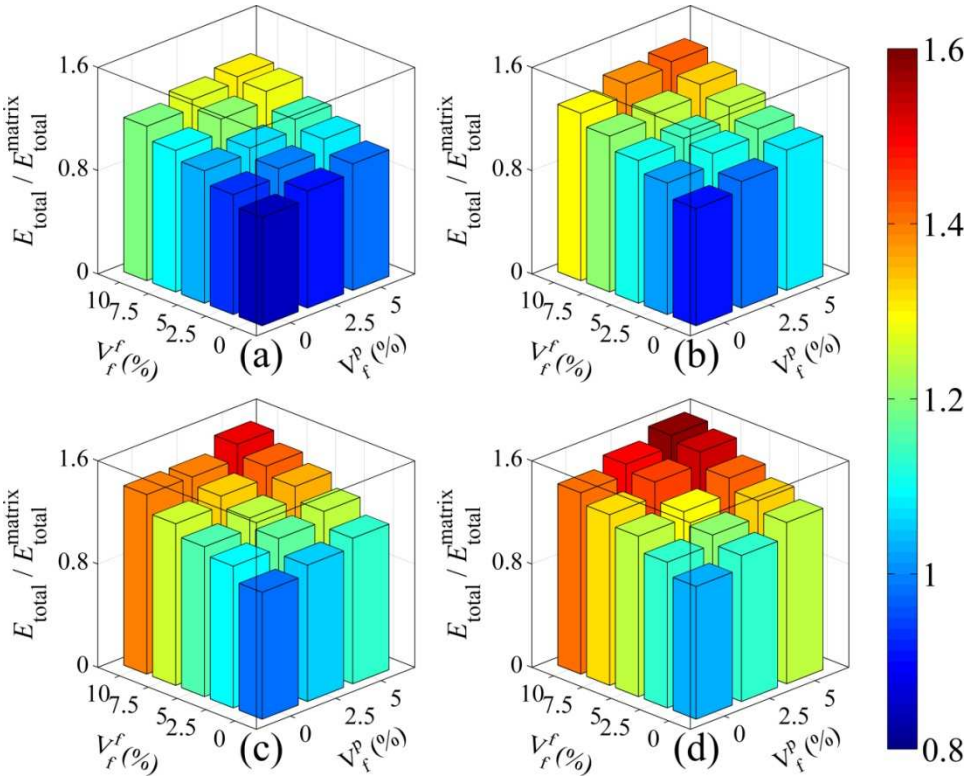

Figure 15. Normalized total energy-dissipation capacity at 6.0 μs for all 60 microstructures at four different aggregate volume fractions: (a) 10%, (b) 20%, (c) 30%, and (d) 40%. The normalizing factor $E_{total}^{matrix} = 135\ \mathrm{MJ/m^3}$.

As predicted, increasing the volume fraction of all three constituent phases serves to increase the total energy dissipation. However, the addition of a small amount of aggregate alone decreases the total energy dissipation. Specifically, the microstructure with 10% aggregate and no fibers or porosity has an energy-dissipation capacity of 84% of the baseline case. Even the microstructure with 40% aggregate and no fibers or porosity has an energy-dissipation capacity just 3% higher than that of the baseline case. Despite the fact that aggregate alone does little to improve the energy-dissipation capacity, and in fact diminishes it at low volume fractions, the aggregate has a synergistic effect with porosity. That is, increasing porosity provides a greater benefit to the energy dissipation at larger aggregate

volume fractions. In particular, at 10% aggregate and 0% fibers, increasing the porosity from 0% to 5% increases the energy dissipation by 14%, relative to the baseline. At 40% aggregate, however, the same increase in porosity yields an energy dissipation 22% larger than that of the baseline.

Finally, the total energy dissipation in all microstructures is less than 10% of the total external work. This is likely the reason that the stress does not exhibit measurable attenuation, as discussed in Section 3.1.1. This is not to say that UHPC structures are incapable of attenuating an applied load. Rather, larger size and time scales, which would allow for a larger percentage of the external work to be dissipated, would likely be necessary for the stress to show signs of attenuation. The low percentage of external work dissipated may also be due to the rigid lateral boundary conditions, which restrict motion in the x_1 (horizontal) direction. Identical simulations with traction-free boundary conditions dissipate up to approximately 20% of the total external work. Nonetheless, the trends in the data agree with experimental findings. Increased porosity and fibers allow for a greater percentage of the external work to be dissipated.

The unique nature of the cohesive finite element model presented herein allows for the energy dissipation to be broken down into three constituent components: damage through interface fracture, inelastic deformation and granular flow of the cementitious paste, and interfacial friction along cracked interfaces. The components of the total energy dissipation will be discussed in more thorough detail below, beginning with the energy dissipated through damage and fracture of interfaces, proceeding to the energy dissipated through friction between fractured interfaces, and ending with the energy dissipated through inelastic deformation.

3.1.2.2. Energy Dissipated Through Interface Fracture

Figure 16 shows the energy dissipation through interface damage and fracture in all 60 microstructures. The normalizing factor $E_{\mathrm{d}}^{\mathrm{matrix}} = 0.3\,\mathrm{MJ/m^3}$. Note that nearly all microstructures dissipate less energy through damage than the baseline case. It is not until volume fractions of 40% aggregate and 5% porosity that more energy is dissipated through damage than in the baseline microstructure. Specifically, the microstructure with 40% aggregate, 5% porosity, and 0% fibers dissipates 15% more energy than the baseline case. As fibers are added, the energy dissipated through damage decreases. At 40% aggregate, 5% porosity, and 10% fibers, the energy dissipated through damage is 97% of the damage dissipated in the baseline case.

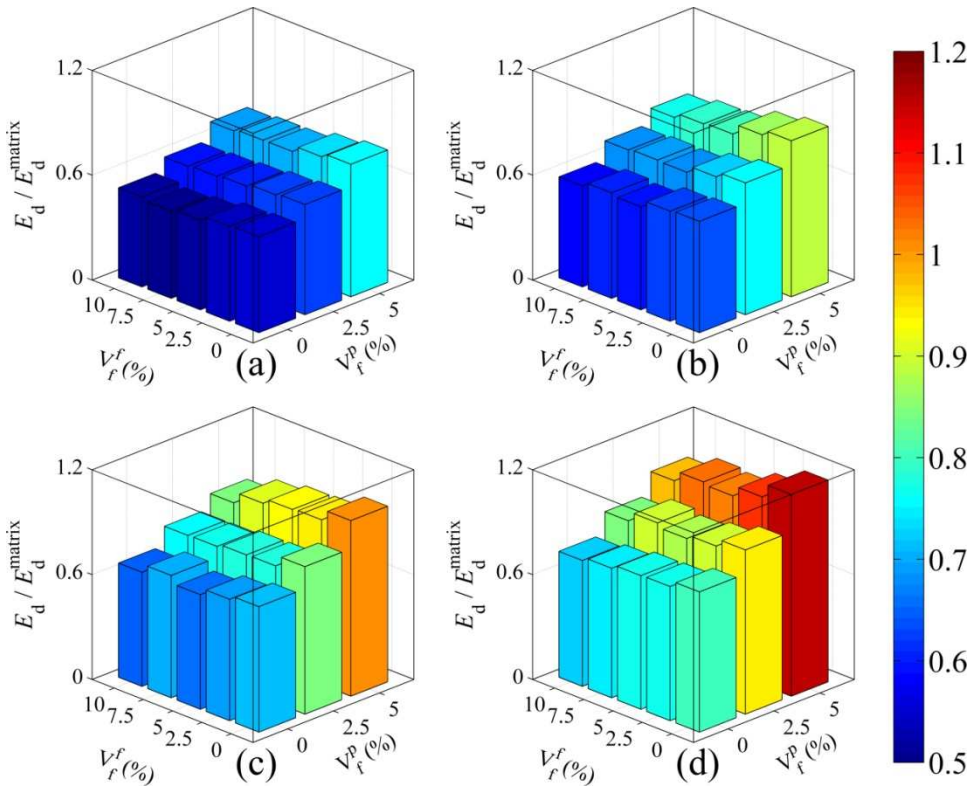

Figure 16. Normalized energy dissipation through interface damage and fracture at 6.0 μs for all 60 microstructures at four different aggregate volume fractions: (a) 10%, (b) 20%, (c) 30%, and (d) 40%. The normalizing factor $E_d^{matrix} = 0.3\ \mathrm{MJ/m^3}$.

The porosity has a synergistic effect with the aggregate on the energy dissipated through interface damage, similar to the trend observed in the total energy dissipation. That is, the benefit of porosity increases with increasing aggregate volume fractions. For example, at 10% aggregate and 0% fibers, increasing the porosity from 0% to 5% increases the energy dissipated through interface damage by 21% with respect to the baseline. At 40% aggregate, the same increase in porosity yields a 35% increase in the energy dissipated through interface, relative to the baseline.

Fibers and porosity have a competing effect on the energy dissipated through interface damage and friction. The benefit of porosity diminishes with increasing fiber volume fractions. For example, at 10% aggregate, increasing the porosity from 0% to 5%

can increase the energy dissipated through damage by as much as 21% in the absence of fibers or as little as 17% in the presence of a 10% fiber volume fraction. This competing effect is even more pronounced at high aggregate volume fractions. For example, at 40% aggregate, increasing the porosity from 0% to 5% can increase the energy dissipated through damage by up to 35% in the absence of fibers or as little as 25% in the presence of a 10% fiber volume fraction.

The energy dissipated through damage and fracture is by definition due in part to the energy dissipated in the pre-failure elastic softening of interfaces. This energy dissipation component, therefore, does not provide an accurate representation of the degree of cracking. Two common metrics for assessing the extent of cracking in solids are the scalar crack density parameter and the crack density tensor [43, 44]. The 2D scalar crack density D_A is given by $D_A = \frac{1}{A}\sum_{k=1}^{N} l_k^{\,2}$, where A is the 2D area of averaging, l_k is the half-length of the k^{th} crack, and N is the total number of cracks. More useful than the scalar parameter is the crack density tensor, which provides information about the degree of anisotropy of cracking in a solid. The components of the crack density tensor are given by $D_{ij} = \frac{1}{A}\sum_{k=1}^{n} l_k^{\,2} n_i^k n_j^k$, where $\boldsymbol{n}^k$ is the unit vector normal to the k^{th} crack. Provided the directional distribution of damage is adequately represented by a second rank tensor, the relationship between the scalar crack density parameter and the tensor is simply $D_A = tr(\mathbf{D})$. The significance of the crack density tensor is that it provides insight into both the extent of cracking and the degree to which it is anisotropic, which can influence the material's effective elastic properties if the cracking has a preferred orientation. For purely vertical cracking, the corresponding crack density tensor

has only one non-zero component: the (1,1) position. For purely horizontal cracking, the only non-zero component of the crack density tensor is in the (2,2) position, for example.

The crack density tensor is calculated for each microstructure at each time step of the analysis. Because each volume fraction of phases within a microstructure results in an associated second-rank crack density tensor, the space of damaged microstructures becomes a five-dimensional data set.

To effectively show this five-dimensional data set, four 2D grids of 2D plots are developed, as seen in Figure 17. Each plot in the figure corresponds to a separate aggregate volume fraction. The horizontal and vertical axes in each plot correspond to the porosity and fiber volume fractions, respectively. Each of the 15 grids within each plot conveys the second-order crack density tensor. The upper left dot in each grid corresponds to component $\mathbf{D}_{11}$, the upper right dot corresponds to component $\mathbf{D}_{12}$, the lower left dot corresponds to component $\mathbf{D}_{21}$, and the lower right dot corresponds to component $\mathbf{D}_{22}$. The colors of the dots indicate the magnitude of the tensorial component according to the color bar shown alongside the plots. Examination of Figure 17 reveals that the $\mathbf{D}_{11}$ component is the largest of all the components in every microstructure. This indicates that the cracking is predominately vertical. Note that the $\mathbf{D}_{22}$ is non-zero. In fact, it is the second largest component in every microstructure. It may be presumed that, given the direction of the loading, horizontal cracks (perpendicular to the direction of loading) will not develop. However, the crack density tensor clearly shows that there is a measurable amount of horizontal cracking. The off-diagonal terms of the crack density tensor are nearly zero and are not nearly as large as the terms on the main diagonal, indicating that any diagonal cracks are closer to vertical and/or horizontal than they are to 45 degrees.

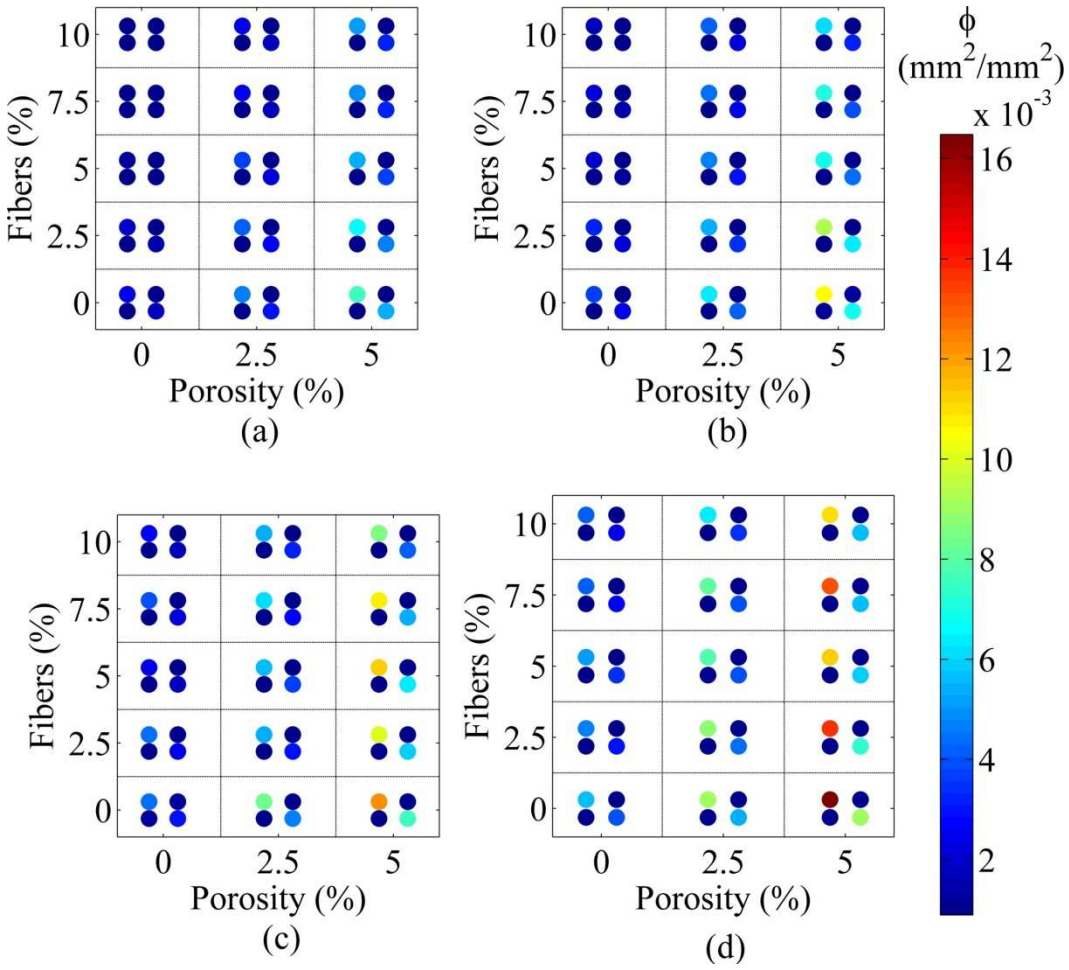

Figure 17. 2D crack density tensor at 6.0 μs for all 60 microstructures with four different aggregate volume fractions: (a) 10%, (b) 20%, (c) 30%, and (d) 40%.

Figure 18 shows the scalar crack density parameter in all 60 microstructures. It can be seen that the constituent phase with the greatest influence on the scalar crack density parameter is porosity. For example, at 40% aggregate and 0% fibers, increasing the porosity from 0% to 5% increases the scalar crack density by 193%. As with the energy dissipated through damage and fracture, porosity and fibers have competing effects on the crack density. Increasing the porosity serves to drastically increase the crack density. Fibers serve not only to decrease the scalar crack density but also to diminish the effect of porosity. For

example, the 193% increase in the scalar crack density discussed previously is diminished to a 158% increase when the microstructure has a fiber volume fraction of 10% instead of 0%. This is indicative of the ability of fibers to arrest the crack development facilitated by porosity.

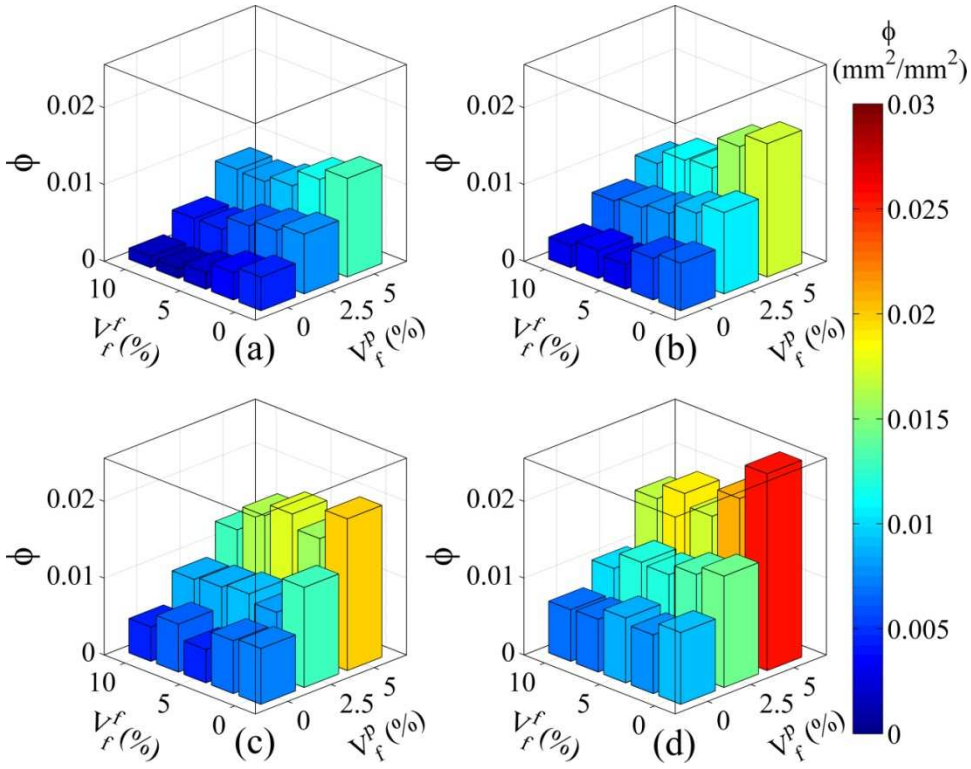

Figure 18. Scalar crack density parameter at 6.0 μs for all 60 microstructures with four different aggregate volume fractions: (a) 10%, (b) 20%, (c) 30%, and (d) 40%.

The crack density is intimately related to the energy dissipated through interface damage and fracture. The scalar crack density parameter quantifies the extent or magnitude of cracking within a material. It can be regarded as a normalized average crack length. The energy dissipated through damage and fracture is the product of a cracked interface's fracture energy and its area. Thus, the crack density is directly proportional to the energy

dissipated through fracture, and the constant of proportionality is equal to the average interface fracture energy. Figure 19 shows the energy dissipated through interface damage and fracture along with the corresponding scalar crack density parameter as a function of strain in microstructures with 0% fiber and 0% porosity. The blue curves represent the energy dissipation, while the red curves represent the scalar crack density parameter. The line style (e.g., dashed, dotted, etc.) represents different porosity volume fractions. As the energy dissipation rises, so too does the crack density.

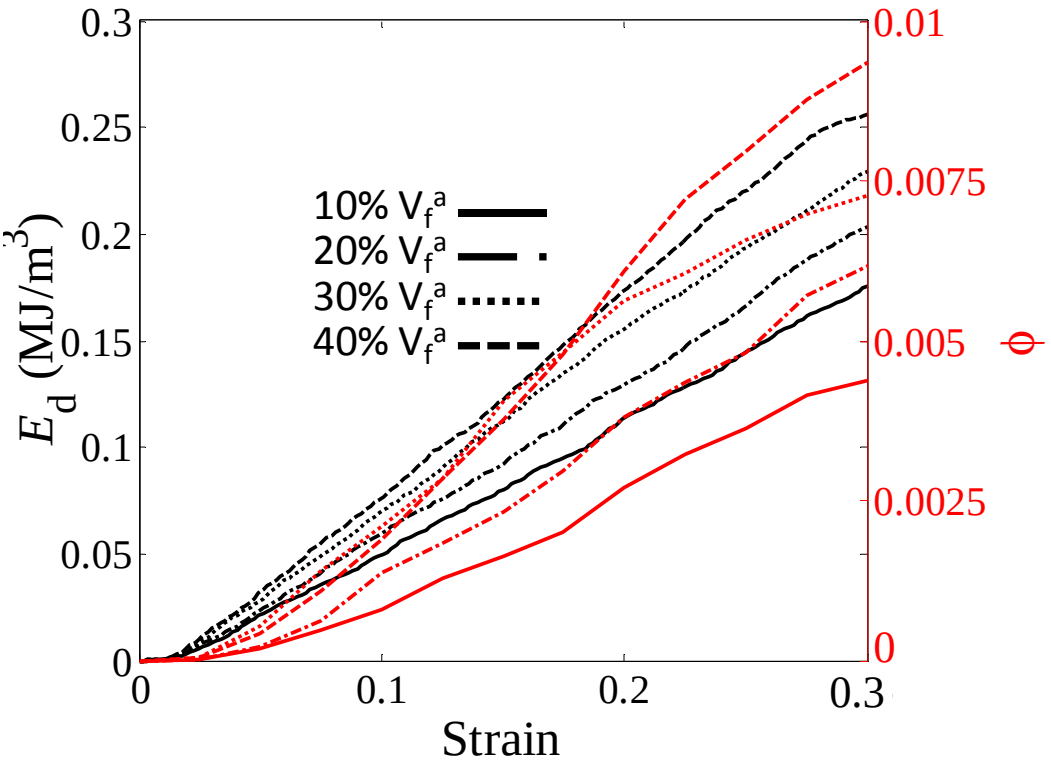

Figure 19. Energy dissipated through interface damage and fracture along with the corresponding scalar crack density parameter as a function of strain in microstructures with 0% fibers and 0% porosity over a range of aggregate volume fractions.

3.1.2.2.1. Spatial distribution of damage dissipation

The previous set of results shows the cumulative energy dissipated through interface damage and fracture in the entire microstructure. It is also of interest to investigate how the energy dissipation is distributed throughout the microstructure. In particular, the rate of energy dissipation through damage as a function of vertical position in the microstructure can provide insight into regions that have the most influence on the total energy dissipation.

Figure 20 shows the spatial distribution of the rate of energy dissipation through interface damage at three instants in time: 0.5 μs, 2.0 μs, and 4.0 μs. Eight subplots are shown, each corresponding to a microstructure at the corners of the 3D parameter space. The vertical axes correspond to vertical position within a microstructure. The horizontal axes show the rate of energy dissipation through interface damage. The rate is normalized to the applied external power for a given microstructure. A number of trends should be noted in the two aforementioned plots. First, the figures show distinct peaks. These peaks correspond to the front of the propagating stress wave. Behind the stress wave, the rate of energy dissipation is on the order of 10^3 times smaller than the rate on the cusp of the wave front. This suggests that as the stress wave propagates through the microstructure, damage and fracture primarily occur at the wave front. The figures also corroborate the result shown in the 3D bar charts in Figure 18. The peaks in the bottom row of subplots of Figure 20, which shows data from microstructures with 40% aggregate, are clearly higher than the peaks in the top row of subplots, which shows data from microstructures with only 10% aggregate. This agrees with the previous finding that higher aggregate content leads to higher energy dissipation due to interface damage.

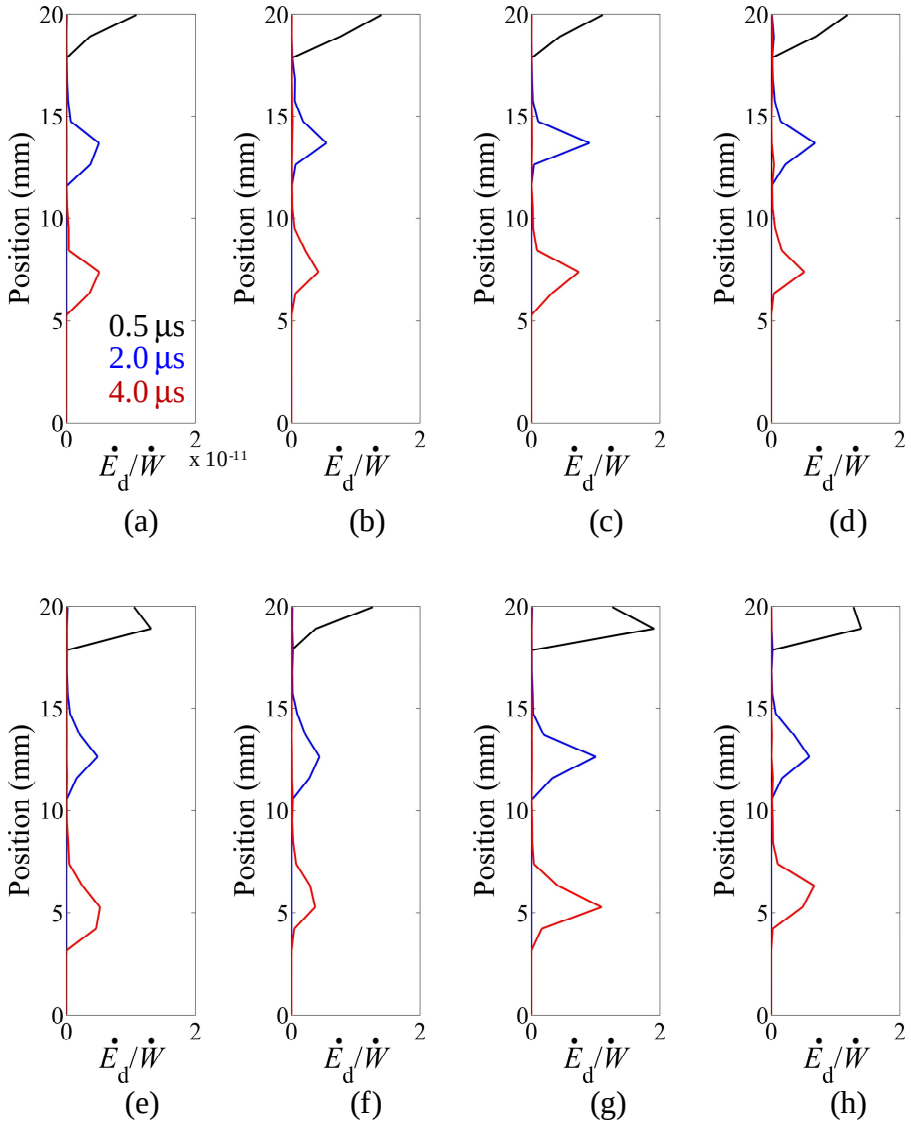

Figure 20. Spatial distributions of the normalized rate of energy dissipation through interface damage in microstructures at the eight extremes of the design space at 0.5 μs, 2.0 μs, and 4.0 μs: (a) 10% aggregate, 0% porosity, 0% fibers; (b) 10% aggregate, 0% porosity, 10% fibers; (c) 10% aggregate, 5% porosity, 0% fibers; (d) 10% aggregate, 5% porosity, 10% fibers; (e) 40% aggregate, 0% porosity, 0% fibers; (f) 40% aggregate, 0% porosity, 10% fibers; (g) 40% aggregate, 5% porosity, 0% fibers; and (h) 40% aggregate, 5% porosity, 10% fibers.

3.1.2.3. Energy Dissipated Through Interfacial Friction

Figure 21 shows the energy dissipation through friction between fractured interfaces in all 60 microstructures. The normalizing factor $E_{\mathrm{f}}^{\mathrm{matrix}} = 45\ \mathrm{MJ/m^3}$. This figure shows many similarities to the data shown in Figure 16 and discussed in Section 3.1.2.2. This is expected: friction along crack faces cannot occur until fracture has taken place. Constituents that contribute to interface fracture will thus also contribute to frictional dissipation.

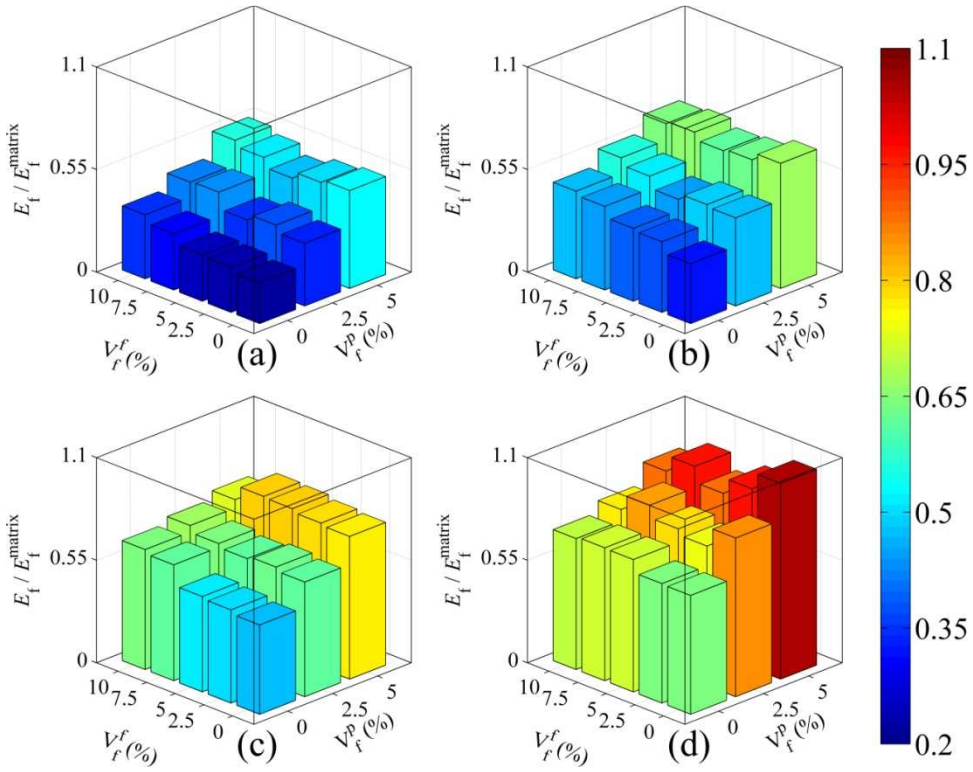

Figure 21. Normalized energy dissipation through interfacial friction at 6.0 μs for all 60 microstructures at four different aggregate volume fractions: (a) 10%, (b) 20%, (c) 30%, and (d) 40%. The normalizing factor $E_{\mathrm{f}}^{\mathrm{matrix}} = 45\ \mathrm{MJ/m^3}$.

As with the crack density and damage energy dissipation, porosity and fibers have competing effects on the frictional energy dissipation. Increased porosity leads to higher

energy dissipation, but this influence is mitigated by the presence of fibers. For example, at an aggregate volume fraction of 10% without any fibers, increasing the porosity from 0% to 5% increases the frictional energy dissipation by 31% relative to the baseline case. However, when the fiber volume fraction is 10%, the same increase in porosity yields only a 21% increase in the frictional energy dissipation. While this is still a large increase, it is significantly less than the increase observed when the fiber volume fraction is 0%. This suggests that at low porosity and low fiber volume fractions, increasing the porosity is the best means of increasing the frictional energy dissipation.

A key difference between the trends in energy dissipated through interface fracture and friction is that increasing fiber volume fractions decreases the energy dissipated through fracture at all porosity volume fractions. In contrast, increasing fiber volume fractions *increases* the energy dissipated through friction at low porosity volume fractions but *decreases* the energy dissipated through friction at high porosity volume fractions. This indicates that the role of fibers in the energy dissipation process shifts depending on the amounts of the other constituents. In the presence of high porosity volume fractions, which contribute to a greater degree of cracking, as seen in Figure 18, fibers serve to arrest crack propagation and constraint the resultant frictional dissipation. It will be seen in the next section that porosity facilitates a greater degree of cracking by allowing for more distributed plastic strain and granular flow of the cementitious matrix. In the absence of porosity, this deformation mechanism is not available to the cementitious matrix, and so the friction between the matrix and the fibers has a more pronounced effect.

3.1.2.4. Energy Dissipated Through Inelastic Deformation

Figure 22 shows the energy dissipation through inelastic deformation in all 60 microstructures. The normalizing factor $E_{\mathrm{p}}^{\mathrm{matrix}} = 90\ \mathrm{MJ/m^3}$. Unlike the other two components of energy dissipation, where large volume fractions of the constituents are necessary to generate energy dissipation values in excess of those of the baseline case, the energy dissipated through inelastic deformation is higher than that of the baseline cases for all volume fractions considered. Specifically, at 10% aggregate, 0% porosity, and 0% fibers, the plastic energy dissipation is 15% higher than that of the baseline case. Increasing the volume fraction of any of the constituents increases the plastic dissipation.

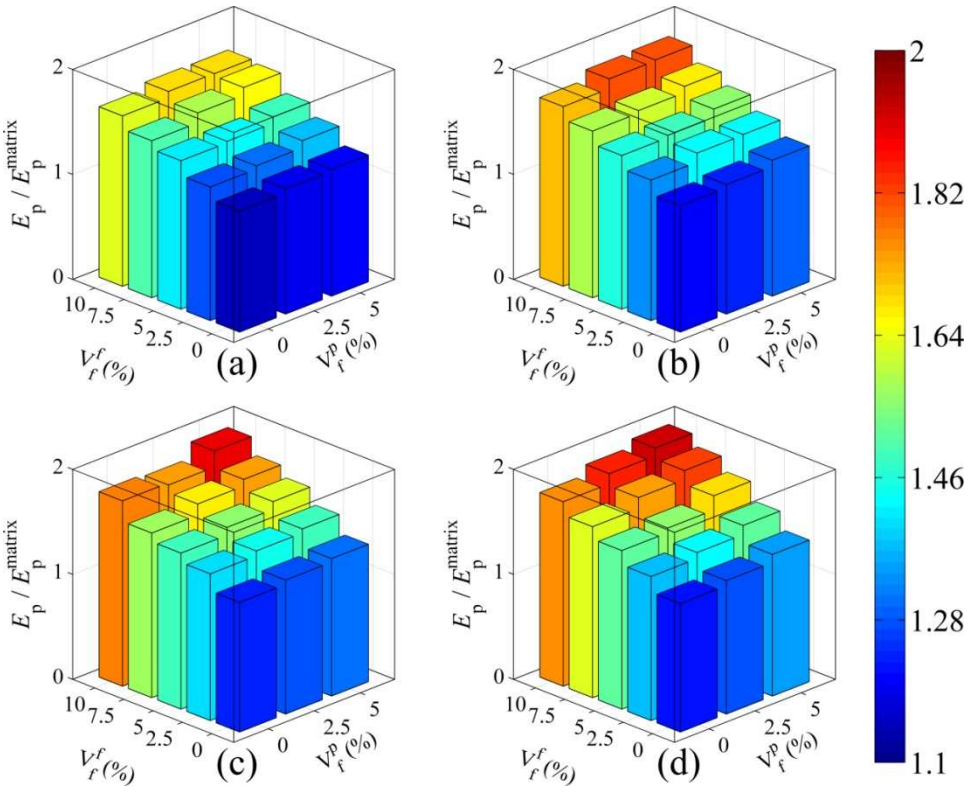

Figure 22. Normalized energy dissipation through inelastic deformation at 6.0 μs for all 60 microstructures at four different aggregate volume fractions: (a) 10%, (b) 20%, (c) 30%, and (d) 40%. The normalizing factor $E_{\mathrm{p}}^{\mathrm{matrix}} = 90\ \mathrm{MJ/m^3}$.

The fiber volume fraction has a substantial influence on the energy dissipated through inelastic deformation. At all levels of aggregate and porosity, increasing the fiber volume fraction from 0% to 10% increases the energy dissipation through inelastic deformation by over 45% relative to the baseline case. The aggregate and porosity phases have only a slight influence on the amount of energy dissipated through inelastic deformation. At a given fiber volume fraction, changing either the aggregate or porosity volume fractions within the range considered changes the plastic energy dissipation by less than 10% relative to the baseline.

The effect of the fibers and porosity on the energy dissipated through inelastic deformation is shown in Figure 23. This figure compares the equivalent plastic strains in three microstructures with a common aggregate fraction of 10% but with different fiber and porosity volume fractions. Figure 23(a) shows a microstructure with 0% fibers and 0% porosity, Figure 23(b) shows a microstructure with 10% fibers and 0% porosity, and Figure 23(c) shows a microstructure with 0% fibers and 5% porosity. The color map scales are identical in each image to facilitate direct comparison among the three microstructures. Figure 23(a) shows the highest levels of plastic strain concentrated above and below the quartz grains. This is consistent from the theoretical consideration of spherical inclusions in an elasto-plastic matrix. Figure 23(b) shows substantially more plastic strain than Figure 23(a). The areas of highest plastic strain correspond to fiber locations. This is indicative of the significant effect of fibers on the inelastic deformation and the slight influence from porosity. Figure 23(c) shows elevated plastic strain around collapsed voids.

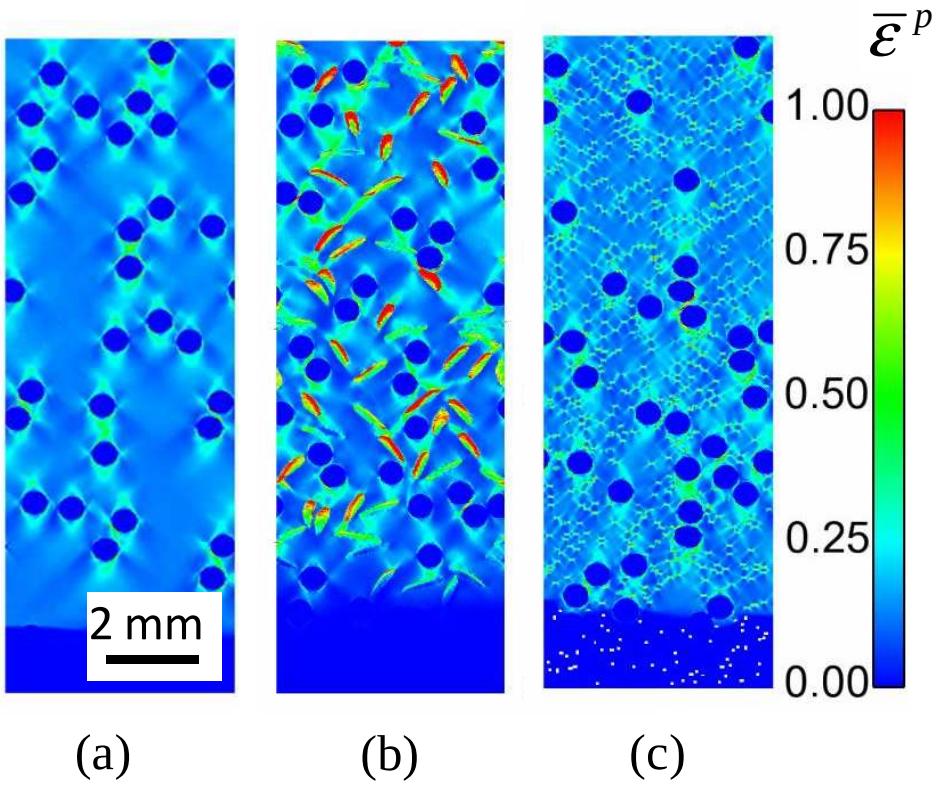

Figure 23. Distributions of equivalent plastic strain at 6.0 μs in microstructures with 10% aggregate and (a) 0% porosity, 0% fibers; (b) 0% porosity, 10% fibers; and (c) 5% porosity, 0% fibers.

3.1.2.4.1. Spatial distribution of inelastic dissipation

The previous set of results shows the cumulative energy dissipated through inelastic deformation in the entire microstructure. It is also of interest to understand how the energy dissipation is distributed throughout the microstructure. In particular, the rate of plastic energy dissipation as a function of vertical position in the microstructure can provide insight into regions that have the most influence on the total energy dissipation.

Figure 24 shows the spatial distribution of the rate of energy dissipation through interface damage at three instants in time: 0.5 μs, 2.0 μs, and 4.0 μs. Eight subplots are

shown, each corresponding to a microstructure at the corners/limits of range of the parametric study. The vertical axes correspond to vertical position within a microstructure. The horizontal axes show the rate of energy dissipation through plastic deformation. The rate is normalized to the applied external work input rate for a given microstructure. This input rate is on the order of 10^5 W. To obtain a complete picture of the spatial distribution of the energy dissipation, it is necessary to consider different times. Several trends can be identified from these plots, and all are similar to the trends previously observed in the distributions of the energy dissipated through interface damage. First, the figures show distinct peaks. These peaks correspond to the front of the propagating stress wave. Behind the stress wave front, the rate of energy dissipation is on the order of 10^3 times smaller than the rate on the cusp of the wave front, suggesting that as the stress wave propagates through the microstructure, inelastic deformation occurs primarily at the wave front and little deformation occurs behind the front. In this regard, the spatial distribution of energy dissipation through inelastic deformation is similar to the distribution of energy dissipation through interface damage.

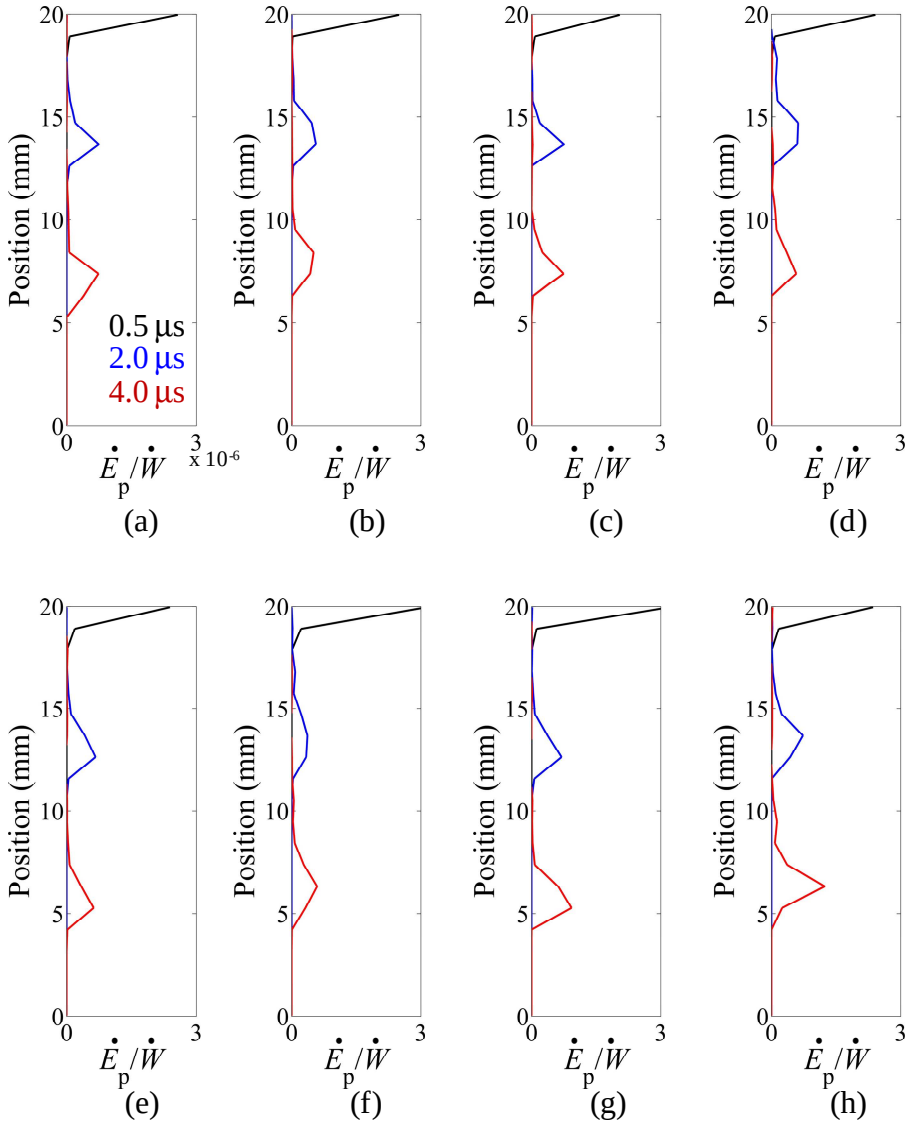

Figure 24. Spatial distributions of the normalized rate of energy dissipation through inelastic deformation in microstructures at the eight extremes of the design space at 0.5 μs, 2.0 μs, and 4.0 μs: (a) 10% aggregate, 0% porosity, 0% fibers; (b) 10% aggregate, 0% porosity, 10% fibers; (c) 10% aggregate, 5% porosity, 0% fibers; (d) 10% aggregate, 5% porosity, 10% fibers; (e) 40% aggregate, 0% porosity, 0% fibers; (f) 40% aggregate, 0% porosity, 10% fibers; (g) 40% aggregate, 5% porosity, 0% fibers; and (h) 40% aggregate, 5% porosity, 10% fibers.

3.1.3. Microstructure Performance Relation Maps

The preceding discussion focused on the load-carrying and energy-dissipation capacities, and their individual components. In particular, the results of parametric studies were shown in a format wherein the response variables were functions of the volume fractions of constituent phases. However, the process of materials design flows in the opposite direction, from the top down. Performance objectives are specified, and then the necessary material attributes are identified. Structure-property/response trends shown in Figure 25, which relate the load-carrying and energy-dissipation capacities to the volume fractions of constituents, provide potential input into the design process.

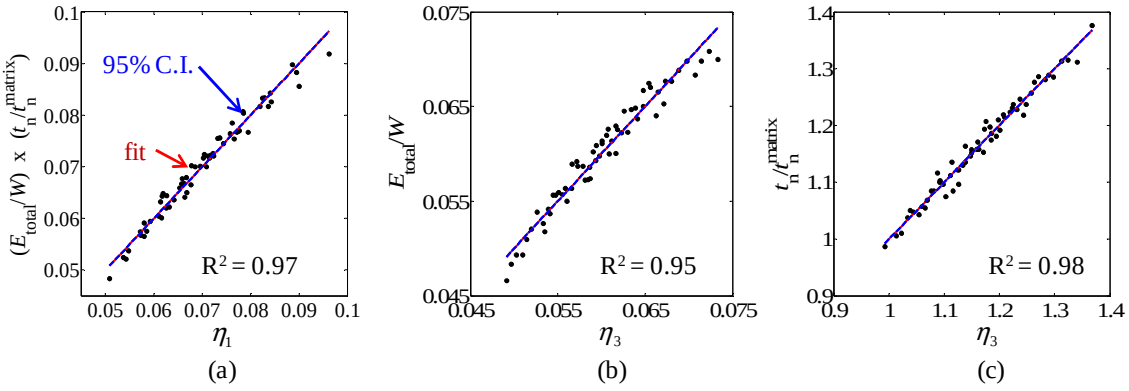

Figure 25. Microstructure performance relations relating (a) energy-dissipation and load-carrying capacities to volume fractions of constituents through parameter η_1, (b) energy-dissipation capacity to volume fractions of constituents through microstructure parameter η_2, and (c) load-carrying capacity to volume fractions of constituents through microstructure parameter η_3.

In Figure 25(a), the vertical axis shows a combined performance metric defined as the product of the energy-dissipation capacity and the load-carrying capacity. Here, the energy-dissipation capacity is expressed as the total energy dissipation normalized by the

total external work; that is, the total work dissipated as a fraction of the total work imparted into the material. The load-carrying capacity is expressed as the traction on the upper surface of a given microstructure normalized by the traction on the upper surface of a microstructure comprised of 100% cementitious matrix. The horizontal axis is a parameter that depends on the volume fractions of the constituents in microstructures. This parameter is obtained through a linear regression analysis and takes the form of

$$\eta_1 = \frac{0.048}{\left(1-V_f^a\right)^{0.47}\left(1-V_f^f\right)^{3.0}\left(1-V_f^p\right)^{2.6}}, \tag{29}$$

which provides the best description of the correlation among dissipation, loading carried, and microstructure.

Figure 25(a) allows the selection of a specific material microstructure design for any given combination of desired load-carrying capacity and energy-dissipation. It is useful for identifying microstructure settings that may meet desired performance objectives and allows the trade-offs between conflicting requirements to be explored. It should be noted, however, that these maps are applicable only to loading under conditions of nominally uniaxial strain and consider only the volume fractions of constituents as design variables. The relation captures the trade-offs between energy dissipation and strength clearly; increasing the load-carrying capacity will likely reduce the energy-dissipation capacity.

Figure 25(b) relates the energy-dissipation capacity to microstructure. As in the first relation, the parameter that provides the best description of the correlation between the dissipation and microstructure is

$$\eta_2 = \frac{0.049}{\left(1-V_f^a\right)^{0.09}\left(1-V_f^f\right)^{1.81}\left(1-V_f^p\right)^{3.38}}. \tag{30}$$

With all other parameters fixed, increasing any of the three constituents increases the energy dissipation capability of the materials, with porosity having the most significant influence, followed by the fibers and then the aggregate.

Figure 25(c) relates the load-carrying capacity to the volume fractions of the constituents. The parameter that provides the best description of the correlation between the load carried and microstructure is

$$\eta_3 = \frac{0.99\left(1-V_f^p\right)^{0.80}}{\left(1-V_f^a\right)^{0.38}\left(1-V_f^f\right)^{1.2}}. \tag{31}$$

This relation highlights the fact that fibers have the most influence over the load-carrying capacity, and the correlation is positive. Porosity is the next most influential constituent, and the correlation is negative. Finally, aggregate has the least influence, and the correlation is positive.

The parameters η_1, η_2, and η_3 express the same information; the three formulations merely represent three different ways of looking at the data. This implies that the three parameters are not fully independent; the combined performance metric η_1 is approximately equal to the product of η_2 and η_3. The relationship is not exact due to the error encountered in performing a least-squares regression on the three parameters separately.

3.2. EFFECT OF SILICA PHASE TRANSFORMATION

To delineate the effect of the phase transformation on the response of UHPC, the results of simulations not accounting for the phase transformation (as discussed in Section 3.1) are compared with the results of calculations that do account for the transformation. The two sets of calculations are carried out under the same loading and constraint conditions.

The former set of simulations will be referred to as the "baseline" simulations. The latter set of simulations will be referred to as the "transformation-enabled simulations."

3.2.1. Load-Carrying Capacity

As the stress wave propagates through a microstructure, the hydrostatic pressure exceeds the threshold of 2.35 GPa behind the wave front, causing the quartz aggregate to transform into coesite, as shown in Figure 26. The particular microstructure shown contains 40% aggregate, 0% porosity, and 10% fibers by volume. Figure 26(a) shows the microstructure at 0.5 μs. At this early stage, the stress wave has just begun to propagate through the material; only quartz at the very top of the microstructure has transformed into coesite. In Figure 26(b), which corresponds to 3.0 μs, the stress wave has traversed approximately half the length of the structure. All quartz behind the wave front has transformed into coesite, while all the quartz ahead of the wave front remains in the α-quartz phase. Figure 26(c) shows the microstructure at 6.0 μs, where the stress wave has nearly reached the bottom surface and essentially all quartz in the structure is in the coesite state.

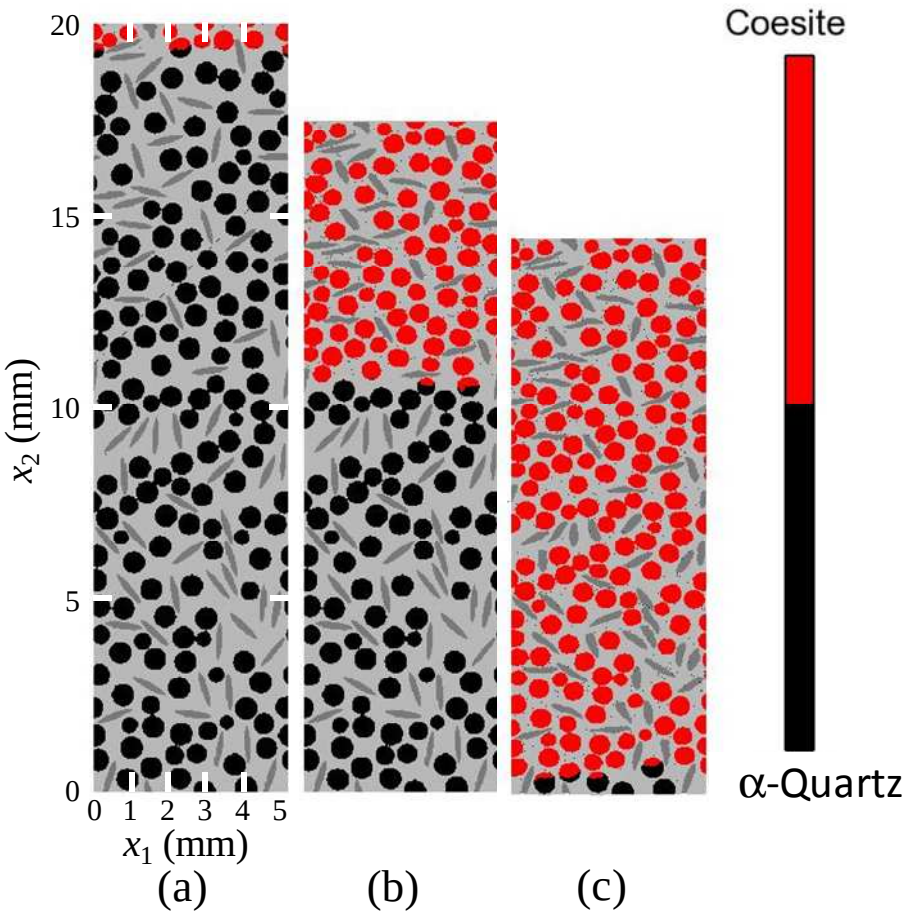

Figure 26. Phase of quartz aggregate as deformation progresses at (a) 0.5 μs, (b) 3.0 μs, and (c) 6.0 μs.

The load-carrying capacity as measured from the transformation-enabled simulations is compared to results from the baseline simulations in Figure 27. As described in Section 3.1.1, the average traction in the vertical direction on the upper surface of a microstructure at any single time step is taken to be a measure of the load carried. This figure shows four subplots, each corresponding to a different aggregate volume fraction. The horizontal axes correspond to the fiber and porosity volume fractions. The vertical axis shows the ratio of the load-carrying capacity as calculated from the simulations with the quartz phase change to

the load-carrying capacity from the baseline simulations without the phase change. The results show a minor downward shift in the load-carrying capacity. In particular, the load-carrying capacity calculated from the simulations with the phase change is in the range of +1.5% to -10.1% of the load-carrying capacity calculated from the baseline simulations.

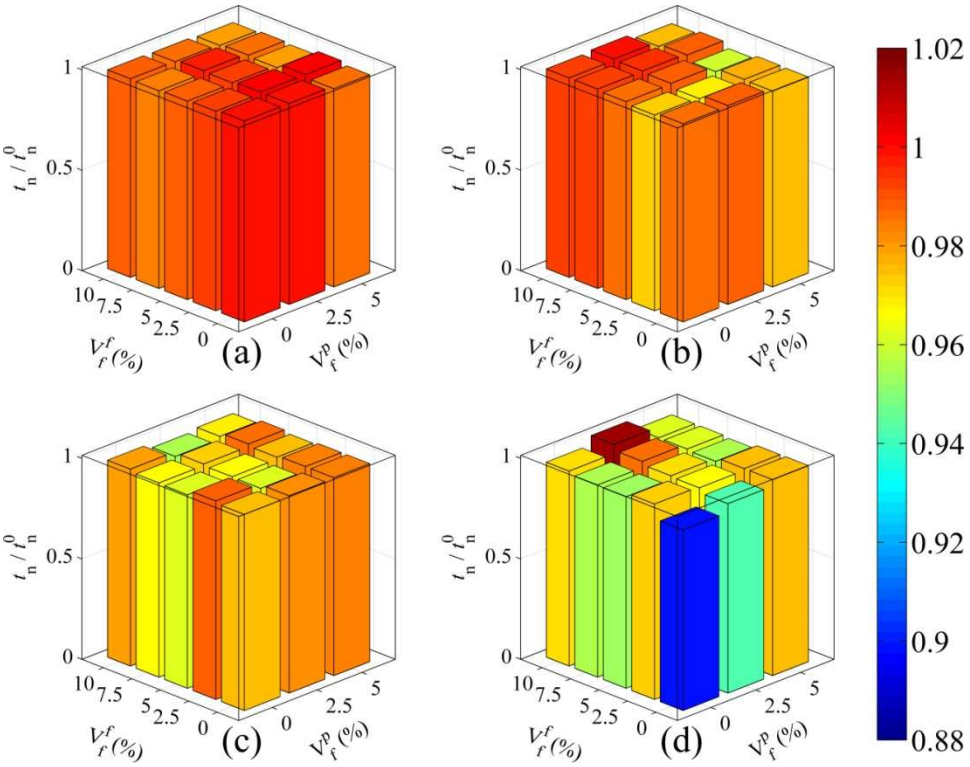

Figure 27. Ratio between the load-carrying capacities for cases with and without (baseline cases) quartz phase transformation with (a) 10% aggregate, (b) 20% aggregate, (c) 30% aggregate, and (d) 40% aggregate.

As Figure 27 shows, the load-carrying capacity ratio decreases continuously as the aggregate volume fraction increases. The load-carrying capacity ratio is relatively insensitive to fiber or porosity content; that is, it is rather constant at a given aggregate volume fraction. The fact that the load-carrying capacity decreases with increasing aggregate content relative

to the baseline case suggests that the phase transformation leads to more internal damage within the aggregate, which, in turn, reduces the load carried by the material.

3.2.2. Energy-Dissipation Capacity

In addition to the three modes of energy dissipation discussed in Section 3.1.2, a fourth mechanism that arises from the phase change of the quartz aggregate is introduced in this section.

3.2.2.1. Total Energy Dissipation

The quartz phase transformation has a more significant effect on the total energy dissipation than on the load-carrying capacity. The ratio of the total energy dissipation calculated from the transformation-enabled simulations to the total energy dissipation calculated from the baseline simulations is shown in Figure 28. The simulations with the phase transformation lead to higher energy-dissipation values. Specifically, the total energy dissipation calculated from the simulations with the phase change is in the range of +0.3% to +18.5% of the energy dissipation calculated from the baseline simulations. At low aggregate volume fractions, the total energy ratio is almost unity, indicating that the energy dissipation has not changed appreciably. However, as the aggregate volume fraction increases, the energy dissipation relative to the baseline increases. At 10% aggregate, the maximum energy ratio is 1.03. At 20% aggregate, the maximum total energy ratio is 1.08. At 30% aggregate, the maximum total energy ratio is 1.12. At 40% aggregate, the maximum energy ratio is 1.20. This suggests that the transformation of the aggregate enhances various mechanisms of energy dissipation, as increasing aggregate levels lead to increasing energy dissipation relative to the baseline cases. This will be analyzed in more detail in subsequent

sections, when the contributions from different mechanisms to the total energy dissipation are considered individually.

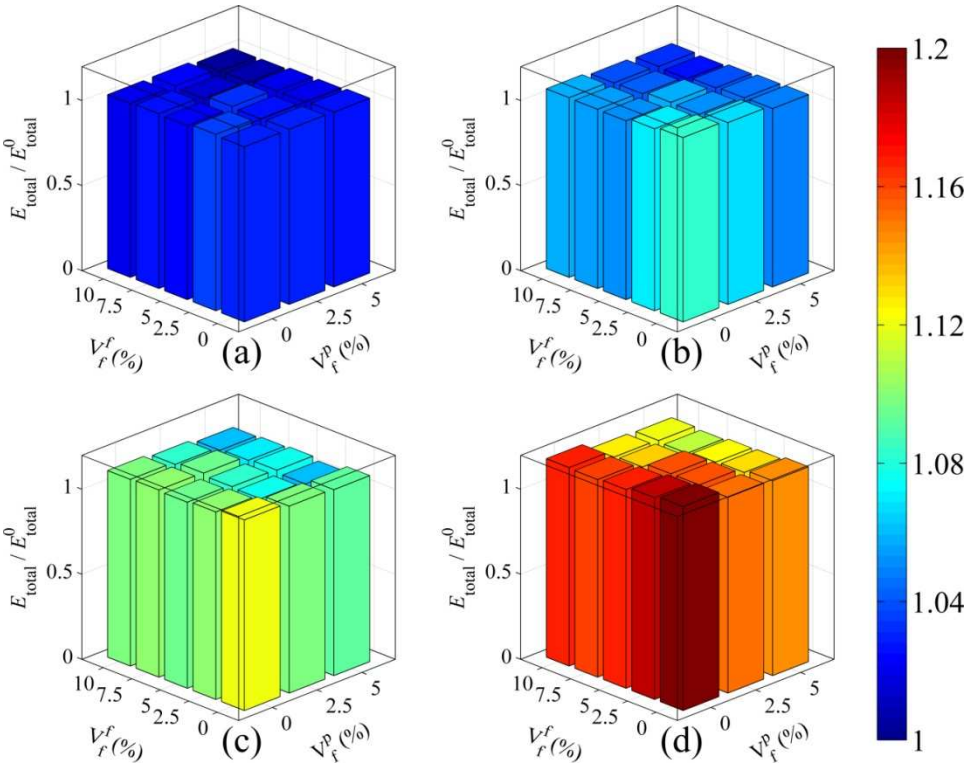

Figure 28. Ratio between total energy dissipation for cases with and without (baseline cases) quartz phase transformation for microstructures with (a) 10% aggregate, (b) 20% aggregate, (c) 30% aggregate, and (d) 40% aggregate.

At a given aggregate volume fraction, the effects of fibers and porosity on the total energy ratio are more complex than the relationship seen in the load-carrying capacity ratio. Note in Figure 28(a) that at 10% aggregate the energy dissipation ratio is relatively constant over all porosity and fiber volume fractions. In contrast, in Figure 28(d), which corresponds to an aggregate volume fraction of 40%, the energy dissipation ratio is still relatively constant at a given porosity level, but increasing the porosity decreases the ratio. Since the only difference between the two simulations is the treatment of the quartz aggregate, it is natural

to think that only the aggregate volume fraction changes the results. However, the fact that increasing porosity decreases the energy dissipation relative to the baseline cases indicates that there is a coupling between the porosity volume fraction and the quartz phase transformation. In particular, low porosity volume fractions yield a higher total energy dissipation than that of the baseline case, while high porosity volume fractions decrease the additional energy dissipation induced by the phase transformation. Although the highest porosity volume fraction considered in this study, 5%, still produces a total energy ratio above unity, the foregoing discussion suggests that there is a porosity volume fraction at which the total energy ratio is exactly one. Such a result may conceal the fact that the quartz phase transformation leads to more fracture and friction within the aggregate phase.

The quartz phase transformation introduces a new component of energy dissipation. When the phase transformation initiates, the volume of the quartz aggregate reduces. This reduction in volume is an energy-consuming process. The energy dissipated through this mechanism is related to the volume of the aggregate that has undergone transformation, the change in volume, and the threshold pressure of transformation. This component is included along with interface damage, friction, and inelastic deformation in the computation of the total energy dissipation. The magnitudes of these four energy dissipation modes relative to each other will be discussed further in the next section.

3.2.2.2. Energy Dissipation Modes

This section considers how the quartz phase transformation affects the contributions of different mechanisms to the total dissipation over the course of the deformation process. Subsequent sections will consider the effect of phase transformation on the individual energy dissipation modes. Figure 29 shows the evolution of the energy dissipation modes in

a microstructure with 40% aggregate, 0% porosity, and 0% fibers. Recall that this microstructure provides the highest total energy-dissipation ratio (see Figure 28). Figure 29(a) corresponds to the simulation with account of the quartz phase transformation, while Figure 29(b) corresponds to the simulation without account of the phase transformation. It can be seen that in the transformation-enabled simulations, a larger percentage of the energy dissipation is due to friction, and a smaller percentage is due to inelastic deformation. In particular, friction accounts for 36.9% and inelastic deformation accounts for 62.3% of the total energy dissipation in the transformation-enabled simulation. In the baseline simulation, friction accounts for 20.6% and inelastic deformation accounts for 79.2% of the total energy dissipation. In both cases, the energy dissipated through interface damage and fracture is less than 0.5%. However, differences are evident. Interface damage and fracture dissipate 0.29% of the total energy imparted into the material by the applied load in the transformation-enabled simulation, whereas dissipation through interface damage and fracture constitutes only 0.13% of the total energy input in the baseline simulations. Because the loading and constraint conditions are identical in all cases, an increase in frictional dissipation is not possible without an increase in interface fracture. Clearly, then, the quartz phase transformation leads not merely to more interface damage, but also to a higher crack density. This increased crack density then gives rise to the significant increase in energy dissipation discussed previously. This will be further analyzed in the next section.

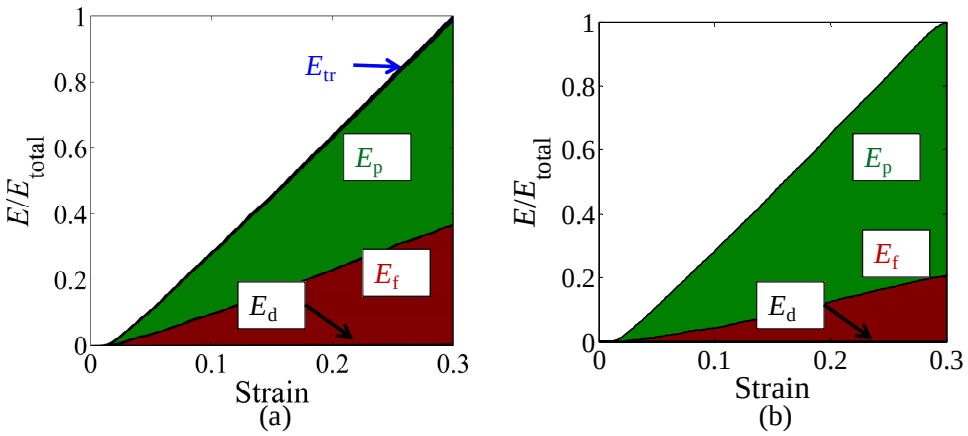

Figure 29. Evolution of the energy dissipated through different mechanisms in a microstructure with 40% aggregate, 0% porosity, and 0% fibers for simulations (a) with quartz phase transformation and (b) without quartz phase transformation.

Figure 29(a) also shows the energy dissipated through phase transformation of the quartz aggregate for a microstructure with 40% aggregate, 0% porosity, and 0% fibers. At 6.0 μs, the phase transformation contributes less than 1.5% of the total energy dissipation. All other microstructures show even smaller proportions of energy dissipated through phase transformation. Although the transformation itself dissipates a relatively small amount of energy, it induces substantially higher energy dissipation by enhancing other dissipation mechanisms. This will be quantified in the next three sections, which address the mechanisms of interface damage, interface friction, and inelastic deformation individually.

Further insight into the relationships between the phase volume fractions, the quartz phase transformation, and energy dissipation can be gained by considering the three components of energy dissipation.

3.2.2.3. Energy Dissipated Through Interface Fracture

Figure 30 shows the ratio of the energy dissipation through interface damage in the transformation-enabled simulations to that of the baseline simulations. For the sake of brevity, this ratio will be referred to as the "damage dissipation ratio." In all microstructures, the damage energy ratio is higher than one, indicating that the phase transformation leads to greater frictional dissipation. The quartz phase transformation has a strong effect on the energy dissipated via interface damage and fracture. The phase transformation yields damage dissipation levels that are up to 94.0% higher than those of the baseline cases.

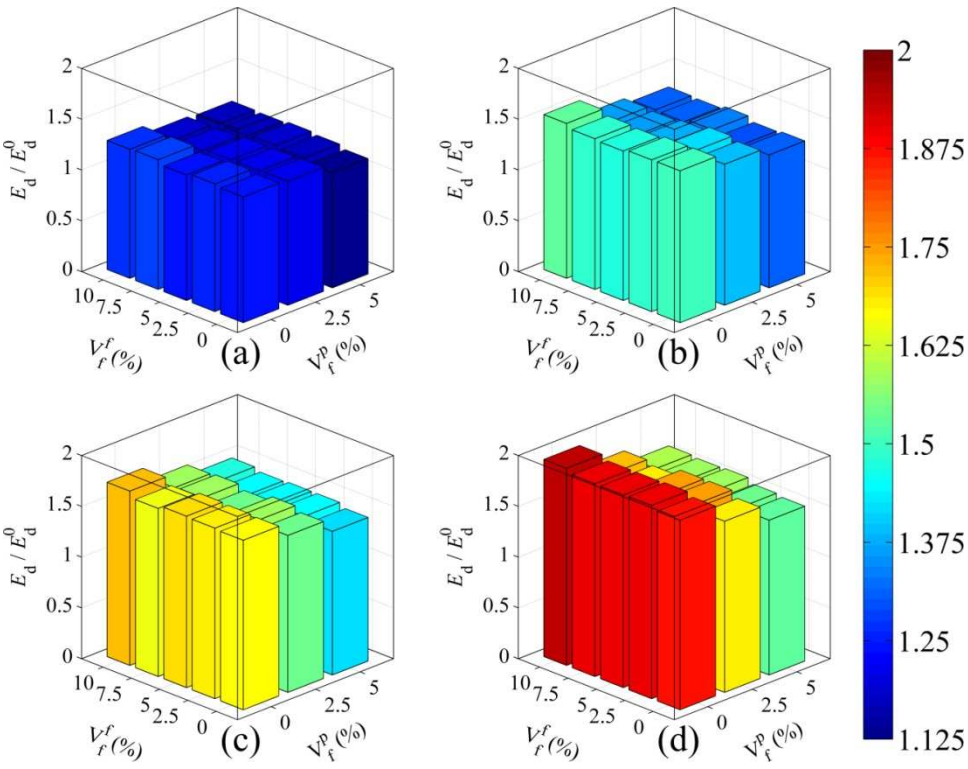

Figure 30. Ratio between the energy dissipated through damage for cases with and without (baseline cases) the phase transformation for microstructures with (a) 10% aggregate, (b) 20% aggregate, (c) 30% aggregate, and (d) 40% aggregate.

Aggregate and porosity have competing effects on the damage dissipation ratio, and this trend becomes more pronounced at higher aggregate volume fractions. At 10% aggregate and 0% fibers, decreasing the porosity from 5% to 0% increases the damage energy ratio from 1.13 to 1.23, giving a net change of 0.1. At 40% aggregate and 0% fibers, decreasing the porosity from 5% to 0% increases the damage energy ratio from 1.52 to 1.87, a net change of 0.35. The highest ratios are seen at an aggregate volume fraction of 40% and a porosity volume fraction of 0%. The lowest ratios are seen at an aggregate value fraction of 10% and a porosity volume fraction of 5%

The trends in the damage dissipation ratio bear resemblance to the trends in the total energy dissipation ratio. Both ratios increase with increasing aggregate fraction. Both ratios are negatively affected by the porosity volume fraction, and the influence of porosity becomes more pronounced at high aggregate volume fractions. The underlying cause for the coupling between aggregate and porosity can be explained by looking at the energy dissipated through damage and fracture along different types of interfaces.

Figure 31 shows the energy dissipated through damage and fracture of the cement phase, fracture of the quartz phase, and debonding along the cement-quartz interfaces in microstructures with 40% aggregate and 0% fibers. Figures 31(a) and (b), the top row, correspond to microstructures with 0% porosity. Figures 31(c) and (d), the bottom row, correspond to microstructures with 5% porosity. Figures 31(a) and (c), the left column, correspond to cases without the quartz phase transformation. Figures 31(b) and (d), the right column, correspond to cases with the quartz phase transformation. First, consider the left column. Without the phase transformation, damage and fracture within the cementitious matrix and quartz aggregate comprise roughly half of the overall damage dissipation regardless of the porosity level. In particular, at 0% porosity, damage dissipation within the

cementitious matrix and quartz aggregate constitute 51.2% and 47.8%, respectively, of the overall damage dissipation. At 5% porosity, damage dissipation within the cementitious matrix and quartz aggregate constitute 52.0% and 47.1%, respectively, of the overall damage dissipation. Clearly, the porosity does not have an appreciable influence on the locations of interface damage in the absence of the phase transformation. Now consider the right column. At 0% porosity, a much larger proportion of the damage dissipation is attributable to intra-quartz fracture with the phase transformation. Specifically, 72.1% of the total is attributable to fracture surfaces inside the quartz phase, while only 27.2% is attributable to fracture surfaces within the cementitious matrix. Also, note that increasing porosity lowers the fraction dissipation attributable to the quartz aggregate. At 5% porosity, damage and fracture within the quartz aggregate drop to 65.1% of the total, while damage and fracture dissipation within the cementitious matrix increase to 34.2% of the total. Since increasing the porosity decreases the damage energy ratio, as seen in Figure 30, the shift cannot be simply due to increased damage and fracture within the cementitious matrix, resulting from higher porosity when phase change is considered. Rather, the shift is due to the lower stresses in the quartz aggregate at higher porosity levels. Such lower stresses make transgranular fracture less likely. A look at the crack density provides more insight in this regard.

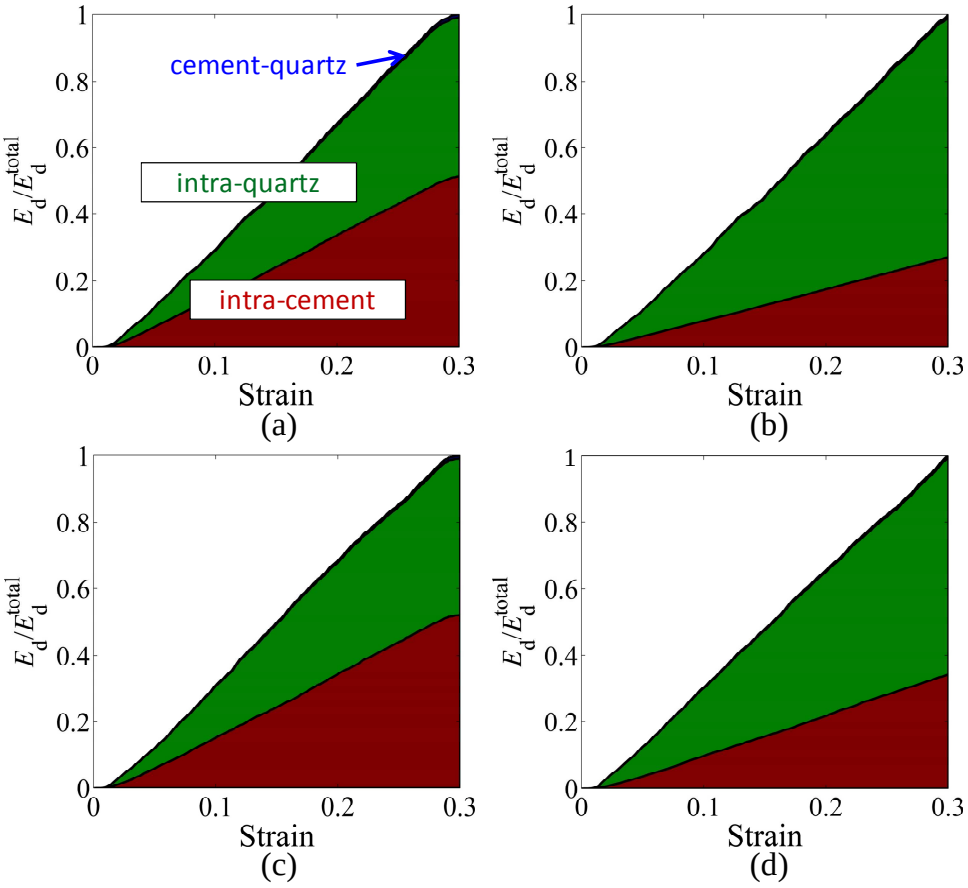

Figure 31. Fraction of energy dissipated through damage and fraction of energy dissipated through fracture (intra-cement, intra-quartz, and along cement-quartz interfaces) in microstructures with 40% aggregate, 0% fibers, and (a) 0% porosity without phase transformation, (b) 0% porosity with phase transformation, (c) 5% porosity without phase transformation, and (d) 5% porosity with phase transformation.

In Section 3.1.2.2, the crack density is used to quantify the extent of cracking within the UHPC microstructures. The same technique is used in the transformation-enabled simulations. Due to the complexity in comparing the 2D crack density tensor among microstructures with three constituent phases, the scalar crack density parameter is used to assess the influence of the quartz phase transformation. Figure 32 shows the ratio of the scalar crack density parameter in the transformation-enabled simulations to the scalar crack density parameter in the baseline simulations. At all aggregate volume fractions, the case with

phase transformation has at least twice the amount of cracking of the case without phase transformation. At high fiber volume fractions and low porosity volume fractions, the case with phase transformation leads to almost five times the amount of cracking of the case without transformation. As the porosity volume fraction increases, the crack density ratio decreases, even for large fiber volume fractions. This trend is similar to the trend observed in the damage energy dissipation ratio. This indicates that increasing the porosity volume fraction brings the amount of cracking in the baseline and transformation-enabled simulations closer together. In other words, increasing the porosity volume fraction provides stress relief within the quartz aggregate, leading to less cracking within the quartz aggregate than would otherwise occur at lower porosity levels.

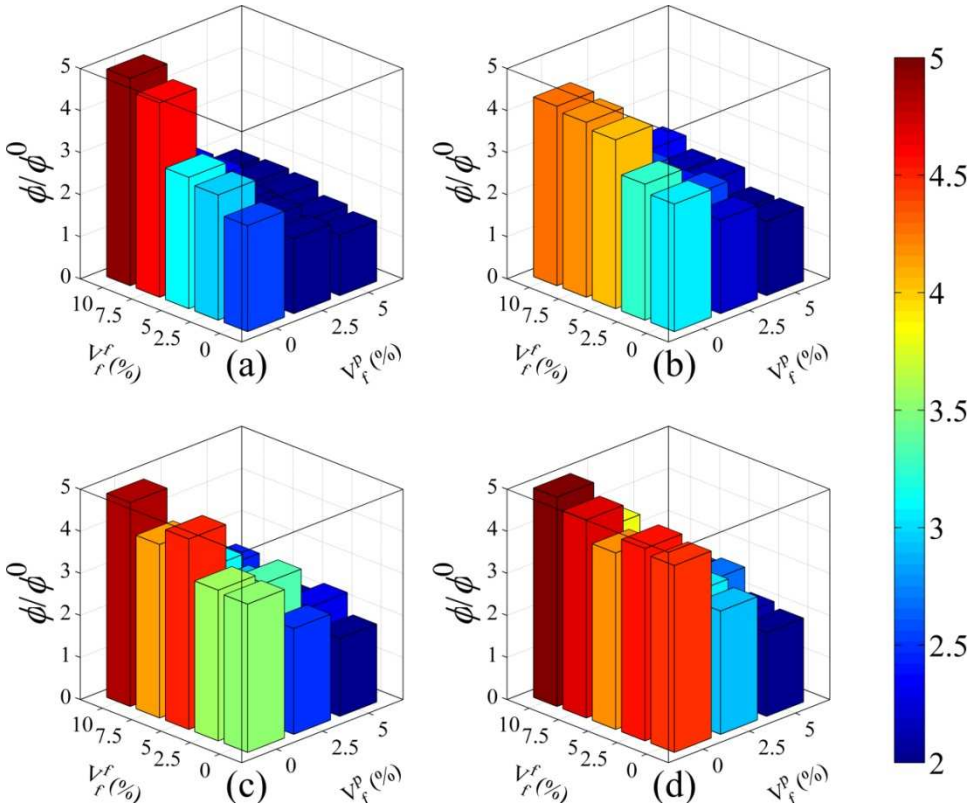

Figure 32. Ratio of scalar crack density parameter in simulations with account of quartz phase transformation to the baseline simulations in microstructures with (a) 10% aggregate, (b) 20% aggregate, (c) 30% aggregate, and (d) 40% aggregate.

3.2.2.4. Energy Dissipated Through Interfacial Friction

The ratio of the frictional energy dissipation as calculated from the transformation-enabled simulations to the frictional energy dissipation as calculated from the baseline simulations is shown in Figure 33. For the sake of brevity, this ratio will be referred to as the "friction energy ratio." The quartz phase transformation has a drastic effect on the energy dissipated through friction between fractured interfaces. In particular, the phase transformation yields frictional energy dissipation levels that are up to 113% higher than those of the baseline simulations. The trends in the friction energy ratio bear resemblance to

the trends in the damage energy ratio. The friction energy ratio increases with increasing aggregate content and decreasing porosity content. However, there is one exception to the similarities with the damage energy ratio. The previous section showed that the damage energy ratio is independent of the fiber volume fraction. In this case, higher fiber volumes tend to decrease the friction energy ratio.

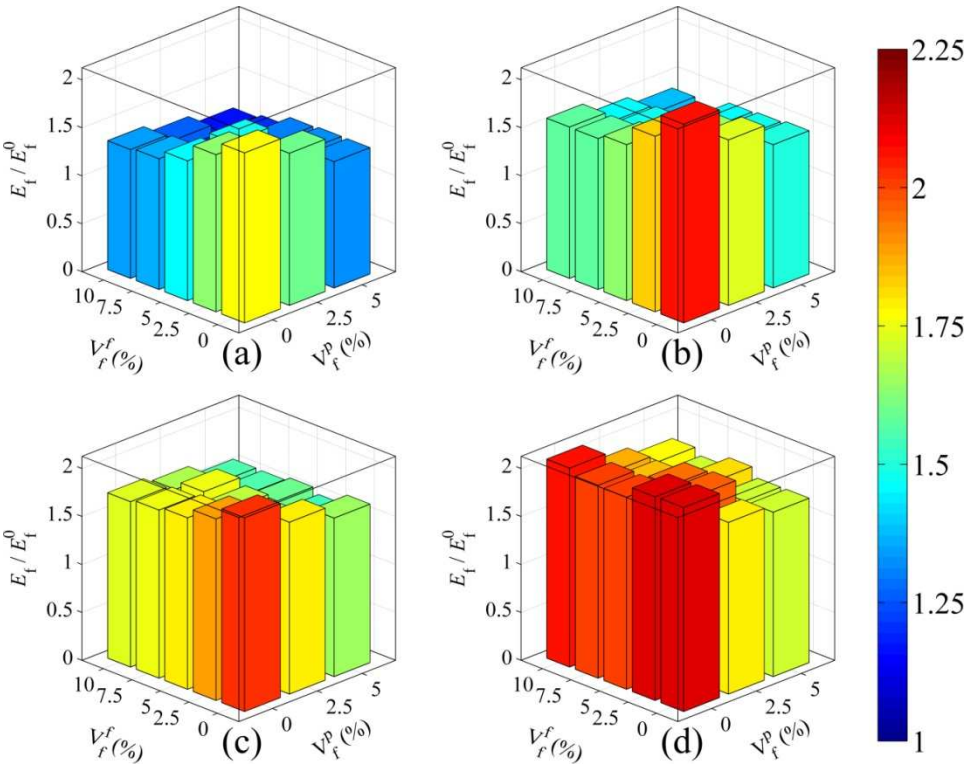

Figure 33. Ratio of energy dissipated through interfacial friction as calculated from simulations with account of quartz phase transformation to the energy dissipated through interfacial friction as calculated from baseline simulations in microstructures with (a) 10% aggregate, (b) 20% aggregate, (c) 30% aggregate, and (d) 40% aggregate.

There is a competition between the effects of aggregate and fibers on the friction energy ratio. The influence of fibers is most pronounced at low aggregate volume fractions. For example, at 10% aggregate and 0% porosity, increasing the fiber volume fraction from 0%

to 10% decreases the friction energy ratio from 1.77 to 1.34. In contrast, at 40% aggregate, increasing the fiber volume fraction from 0% to 10% decreases the friction energy ratio only from 2.13 to 2.07. This suggests that at low aggregate volume fractions, fibers can effectively reduce the increase in frictional dissipation caused by the quartz phase transformation. At high aggregate volume fractions, however, increasing the fibers has only a minimal effect on the frictional dissipation enhancement due to the phase transformation.

3.2.2.5. Energy Dissipated Through Inelastic Deformation

The ratio of the inelastic energy dissipation as calculated from the transformation-enabled simulations to that as calculated from the baseline simulations is shown in Figure 34. For the sake of brevity, this ratio will be referred to as the "inelastic dissipation ratio." The quartz phase transformation can decrease the energy dissipated through inelastic deformation by up to 9.3% as compared to the baseline results. At a given aggregate volume fraction, the inelastic dissipation ratio is highest at low porosity volume fractions and high fiber volume fractions. In particular, the highest inelastic dissipation ratio of 0.99 is seen at 10% aggregate, 0% porosity, and 7.5% fibers. The lowest is seen at 40% aggregate, 5% porosity, and 0% fibers.

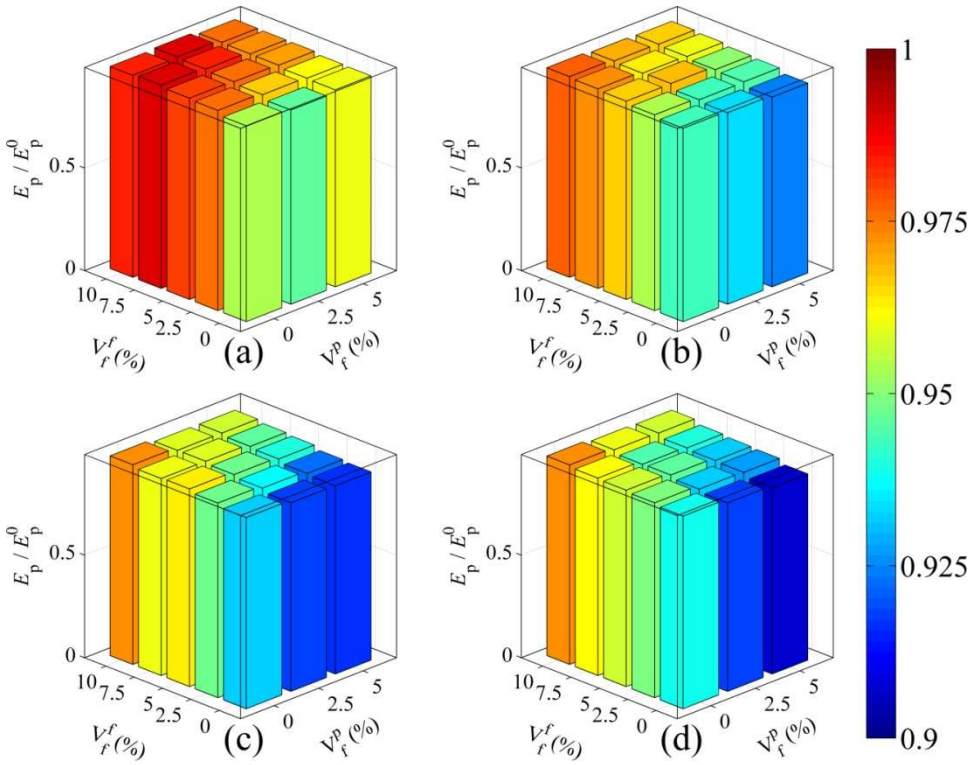

Figure 34. Ratio of energy dissipated through inelastic deformation as calculated from simulations with account of quartz phase transformation to the energy dissipated through inelastic deformation as calculated from baseline simulations with linear elastic quartz properties in microstructures with (a) 10% aggregate, (b) 20% aggregate, (c) 30% aggregate, and (d) 40% aggregate.

Note that at a given aggregate and fiber volume fraction, larger porosity volume fractions lead to lower inelastic dissipation ratios. This suggests that, in the absence of the quartz phase transformation, increasing the porosity leads to more plastic dissipation compared with the case with transformation.

3.2.3. Microstructure Performance Relation Maps

In the first part of this thesis, a set of microstructure-performance relation maps that relate the volume fractions of the constituents to the load-carrying and energy-dissipation capacities were developed. Such structure-property/response maps provide quantification

that can be used in top-down materials design, where performance objectives are specified and the necessary material attributes are then identified. An updated microstructure-performance relation map is shown in Figure 35, accounting for the effects of the quartz phase transformation. To facilitate comparison with the relations developed without consideration of the phase transformation, the results of η_1, η_2, and η_3 are superimposed over Figure 35(a), (b), and (c), respectively.

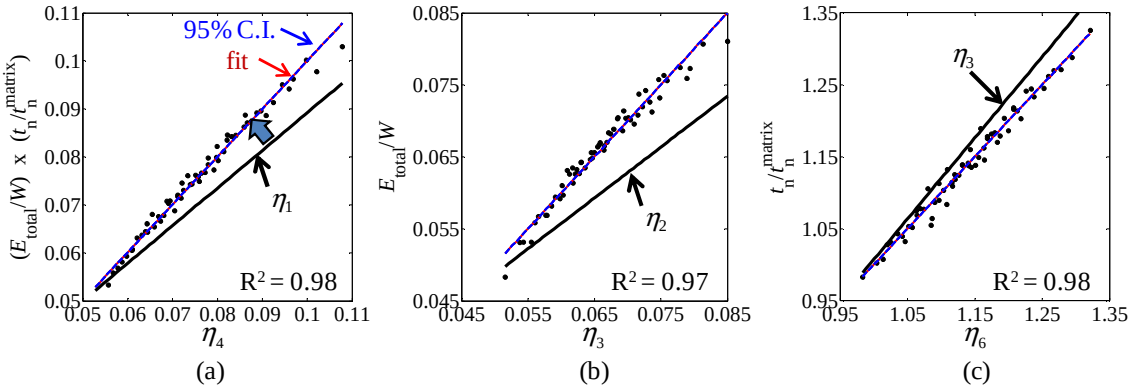

Figure 35. Microstructure performance relation map relating (a) energy-dissipation and load-carrying capacities and load-carrying capacity to volume fractions of constituents, (b) energy-dissipation capacity to volume fractions of constituents, and (c) load-carrying capacity to volume fractions of constituents.

In Figure 35(a) the vertical axis shows a combined performance metric defined as the product of the energy-dissipation capacity and the load-carrying capacity. Here, the energy-dissipation capacity is expressed as the total energy dissipation normalized by the total external work, that is, the total work dissipated as a fraction of the total work imparted into the material. The load-carrying capacity is expressed as the traction on the upper surface of a given microstructure normalized by the traction on the upper surface of a microstructure comprised of 100% cementitious matrix. The horizontal axis is a parameter that depends on

the traction carried by the material and the volume fractions of the constituents in microstructures. This parameter is obtained through a linear regression analysis and takes the form of

$$\eta_4 = \frac{0.049}{\left(1-V_f^a\right)^{0.76}\left(1-V_f^f\right)^{2.8}\left(1-V_f^p\right)^{2.1}}, \tag{32}$$

which provides the best description of the correlation among dissipation, loading carried, and microstructure. The chart in Figure 35(a) can be used to select a desired microstructure setting for any given combination of load-carrying capacity and energy-dissipation capacity.

The relations also illustrate the trade-offs between energy dissipation and strength in microstructure design. Figure 35(b) relates the energy-dissipation capacity to the volume fractions of constituents. The parameter that provides the best description of the correlation between the dissipation and microstructure is

$$\eta_5 = \frac{0.049}{\left(1-V_f^a\right)^{0.45}\left(1-V_f^f\right)^{1.6}\left(1-V_f^p\right)^{2.9}}. \tag{33}$$

Figure 35(c) relates the load-carrying capacity to microstructure. The parameter that provides the best description of the correlation between the load carried and microstructure is

$$\eta_6 = \frac{0.99\left(1-V_f^p\right)^{0.81}}{\left(1-V_f^a\right)^{0.45}\left(1-V_f^f\right)^{1.6}}. \tag{34}$$

These microstructure-performance relations bear many similarities to those presented in the first part of this thesis. A key difference, however, is that the in the first part of this study, η_1 (which corresponds to η_4 here) has exponents of 0.47, 3.0, and 2.6 for the

aggregate, fiber, and porosity phases, respectively. This illustrates that the phase transformation alters the significance of the aggregate and porosity in the dynamic response of UHPC, while the significance of the fibers is relatively unchanged. This difference demonstrates that the phase transformation lends the aggregate a much stronger influence on energy dissipation and should be accounted for in the design of UHPC structures to better mitigate the threats of dynamic loading with high pressures.

Figure 35(a) shows that for a given level of energy-dissipation and load-carrying capacity, a larger value of η_1 is required as compared to η_4. A similar trend can be observed in Figure 35(b). In Figure 35(c), for a given load-carrying capacity, a larger value of η_6 is required as compared to η_3. Because of the nature of the parametric expressions, the relationship between volume fractions of the constituents and the parameters is not one-to-one. That is, multiple microstructural compositions can yield the same parameter value. Figure 36 shows the values of the microstructure performance parameters obtained by the microstructure instantiations analyzed in this thesis. Each point in Figures 36(a)-(f) represents one of the 60 unique combinations of volume fractions of the constituents. The color of each point corresponds to the value of the parameter as indicated by the appropriate legend. The lowest values of η_1 and η_4 are seen at low volume fractions of aggregate, fibers, and porosity. Microstructures with high aggregate, high fiber, and low porosity content show parameter values similar to microstructures with high aggregate, low fiber, and high porosity content. Parameters η_2 and η_5 show similar relationships. Microstructures with high aggregate and high fiber volume fractions show the highest values of η_3 and η_6 with only a minor influence from porosity. Microstructures with low aggregate and low fiber volume fractions show the lowest values of η_3 and η_6.

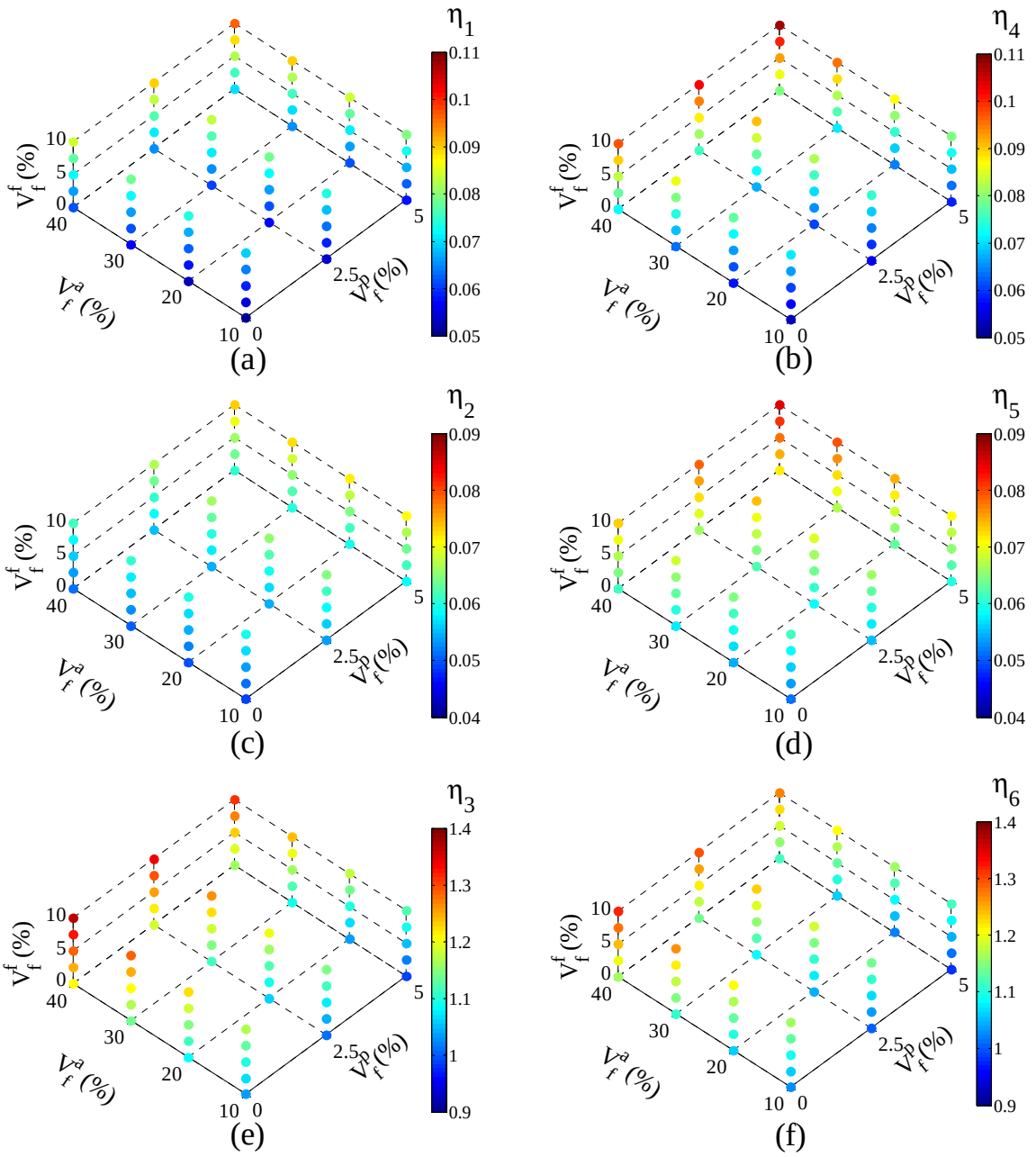

Figure 36. Values taken by the microstructure performance parameters for the microstructure instantiations analyzed in this thesis: (a) η_1, (b) η_2, (c) η_3, (d) η_4, (e) η_5, and (f) η_6.

CHAPTER IV

CONCLUSIONS AND FUTURE WORK

4.1. CONCLUSIONS

A material must balance strength with an ability to dissipate energy to be most effective in blast- and impact-resistant protective structures. UHPC is a building material that provides the benefits of traditional concrete along with increased strength and durability. However, due to the novelty of UHPC and its large range of possible microstructures, the dynamic behavior of UHPC is not fully understood. In an effort to provide useful information for materials' design, the load-carrying and energy-dissipation capabilities of ultra-high-performance concrete under dynamic loading were evaluated over a parametric range of volume fractions of constituent phases. With this motivation in mind, a series of dynamic numerical simulations was conducted in this thesis in which the volume fractions of quartz aggregate, steel fibers, and porosity were explicitly modeled and systematically varied.

The conclusions of this study as they relate to the load-carrying and energy-dissipation capacities are the following:

(1) The volume fractions of constituent phases have a significantly larger influence on the energy-dissipation capacity than on the load-carrying capacity of UHPC. The load-carrying capacity is largely related to density, which affects the longitudinal elastic wave speed and the elastic stiffness of the material. These quantities in turn determine the reaction stress carried by the material.

(2) The propagating stress wave does not show appreciable attenuation in magnitude for the size and time scales considered in this study. This is likely due to the fact that all

microstructures dissipate less than 10% of the external work. Active dissipation occurs primarily at the wave front, partly due to the high level of confinement or stress triaxiality of the nominally uniaxial strain deformation condition.

(3) Fibers and porosity have competing effects on energy dissipation through interface fracture and friction, while aggregate and porosity have a synergistic effect on the energy dissipated through interface fracture. Furthermore, porosity alters the role played by fibers in the frictional dissipation process. At low porosity and aggregate levels, increasing the fiber volume fraction can increase frictional dissipation between the fibers and cementitious matrix by over 12%. At high porosity and aggregate levels, increasing the fiber volume fraction arrests crack propagation facilitated by the presence of porosity and can decrease frictional dissipation by over 17%. At low aggregate levels, increasing the porosity can increase frictional dissipation by almost 30%. At higher aggregate levels, increasing the porosity can increase frictional dissipation by almost 40%.

(4) Inelastic deformation (granular flow of the matrix and plastic deformation of the fibers) contributes approximately 70% - 85% of the total energy dissipation, interfacial frictional dissipation contributes approximately 15% - 30%, and damage accounts for less than 0.5%. Efforts to increase the energy absorbency of UHPC should focus on enhancing inelastic deformation and internal friction, as improvements to these two energy dissipation components have much larger effects than improvements to the interface fracture energy.

Higher temperatures result from high strain-rate dynamic loading, leading to thermally driven events in materials. The analysis reported here does not account for processes such as temperature-induced phase transformation in the quartz aggregate and

thermal softening of the steel fibers or cementitious matrix. The high pressures resulting from the dynamic loading can also induce phase transformations in the constituents. Proper accounting of such phase transformations can allow materials design to take advantage of these mechanisms in order to tailor structural response for specific load applications. This thesis has provided a phenomenological model that accounts for the effects of the transformation of α-quartz into coesite on the behavior of UHPC. This phenomenological model is employed within the framework of a cohesive finite element model to quantify the relations between the load-carrying and energy-dissipating capacities of microstructures with different volume fractions of phases. The quantification covers a range of the microstructure parameters. In addition to microstructure-response relations that can be used in materials' design and selection, the conclusions of this study that pertain to the effects of phase transformation on the load-carrying and energy-dissipation capacities are the following:

(1) Under the conditions of nominally uniaxial strain that involve high stress triaxiality, the α-quartz-to-coesite phase transformation decreases the load-carrying capacity of the material relative to the case without transformation, although this effect is relatively small.

(2) The phase transformation increases the total energy-dissipation capacity of materials by up to 18.5% , even though the transformation itself dissipates less than 2% of the total energy input into the material during a loading event. This disproportional influence is a result of the effect of the transformation on fracture. Specifically, the phase transformation can increase the energy dissipated through crack surface friction by 100% by enhancing the development of cracks. Higher porosity levels and higher fiber volume fractions can reduce this effect of phase transformation, with the effect of fibers being more pronounced.

(3) The phase transformation decreases the energy dissipated through inelastic deformation, and this influence diminishes as aggregate and porosity volume fraction increase.

4.2. RECOMMENDATIONS FOR FUTURE WORK

Due to the elevated temperatures experienced during high strain-rate impact events, thermal effects should be considered in future work to obtain a clearer understanding of the behavior of UHPC under dynamic loading. The current thesis does not account for temperature-induced phase transformation in the quartz aggregate, thermal softening of the steel fibers or cementitious matrix, or other thermal effects. Elevated pressures can also induce phase transformations in the constituents. This thesis considers only the phase change of α-quartz into coesite; other transformations may be relevant to dynamic loading of UHPC, including α-quartz into β-quartz, as well as decarbonation and dehydroxylation of calcium-silicate-hydrates within the cementitious matrix.

This thesis considers only a single set of properties for the cohesive elements. A parametric study using different peak traction or fracture energy values will provide insight into the influence of the interfaces on the dynamic response and potentially motivate research into improving interface strength between phases.

Finally, it should be pointed out that, although the study here concerns only one form of UHPC, the framework developed is applicable to other heterogeneous materials. For example, interest has increased in using polymeric fibers (e.g., PVA and polypropylene) or carbon nanofibers instead of steel fibers in UHPC. Similar studies for such material systems can be conducted using this framework.

APPENDIX A

COMPLETE LISTING OF MICROSTRUCTURES

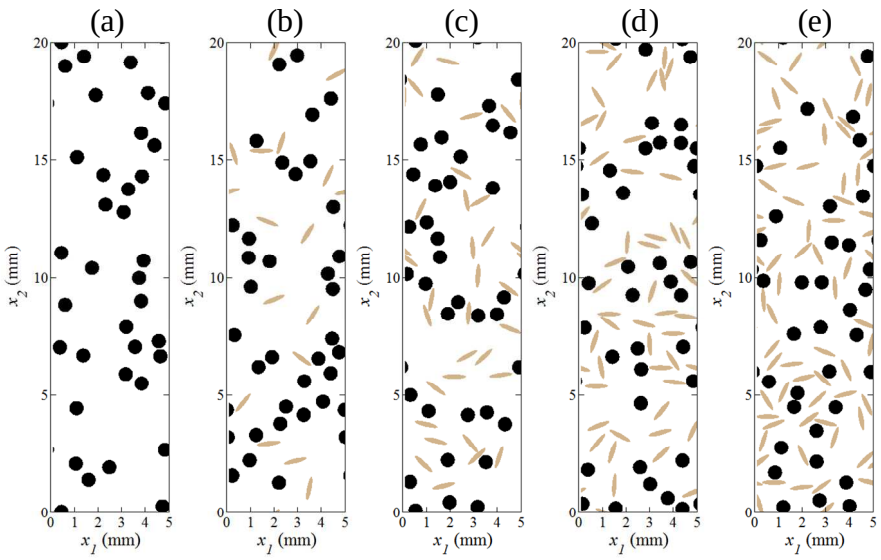

Figure 37. Microstructures with 10% aggregate, 0% porosity, and (a) 0% fibers, (b) 2.5% fibers, (c) 5% fibers, (d) 7.5% fibers, and (e) 10% fibers.

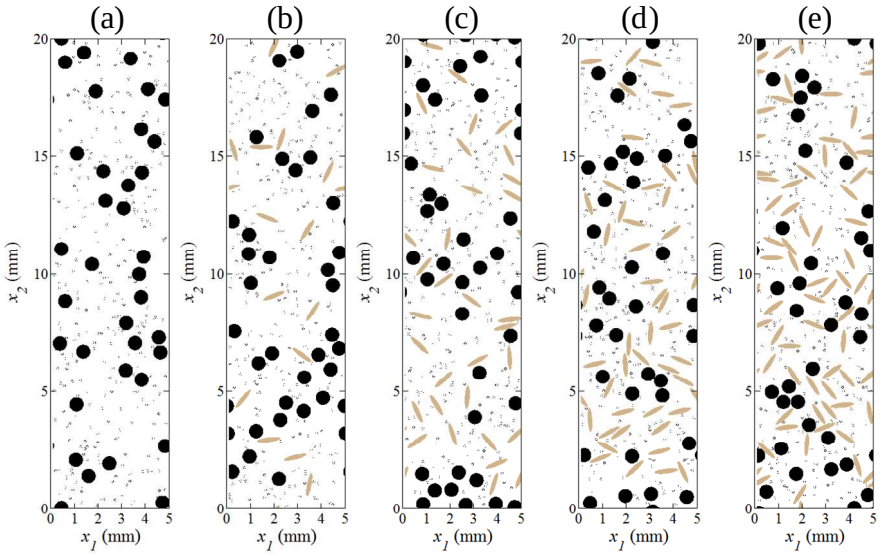

Figure 38. Microstructures with 10% aggregate, 2.5% porosity, and (a) 0% fibers, (b) 2.5% fibers, (c) 5% fibers, (d) 7.5% fibers, and (e) 10% fibers.

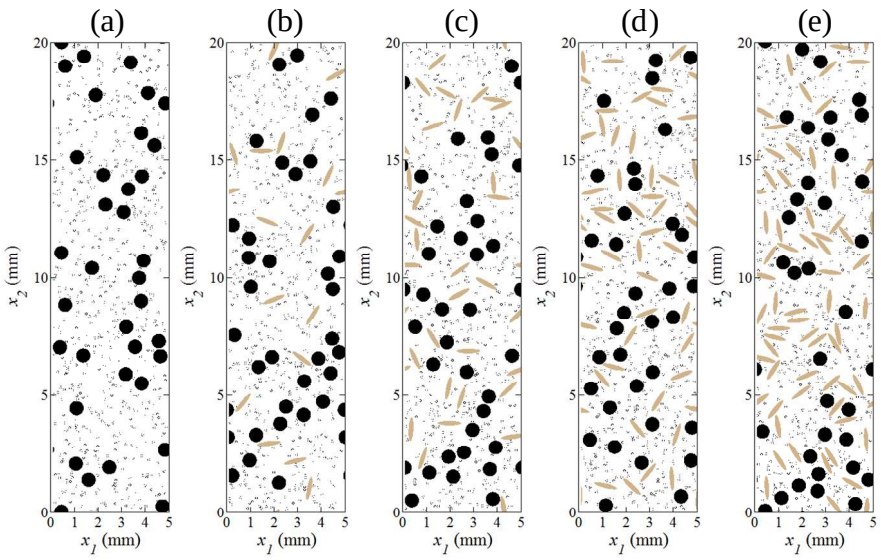

Figure 39. Microstructures with 10% aggregate, 5% porosity, and (a) 0% fibers, (b) 2.5% fibers, (c) 5% fibers, (d) 7.5% fibers, and (e) 10% fibers.

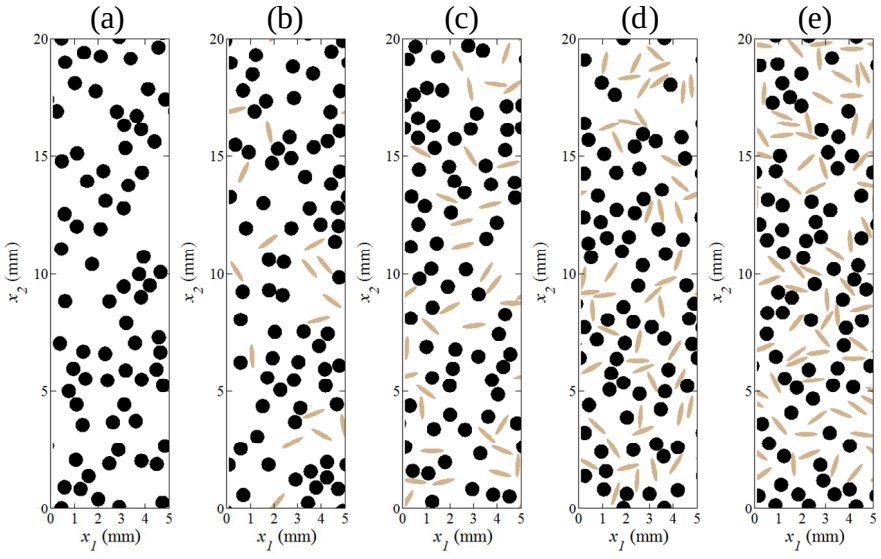

Figure 40. Microstructures with 20% aggregate, 0% porosity, and (a) 0% fibers, (b) 2.5% fibers, (c) 5% fibers, (d) 7.5% fibers, and (e) 10% fibers.

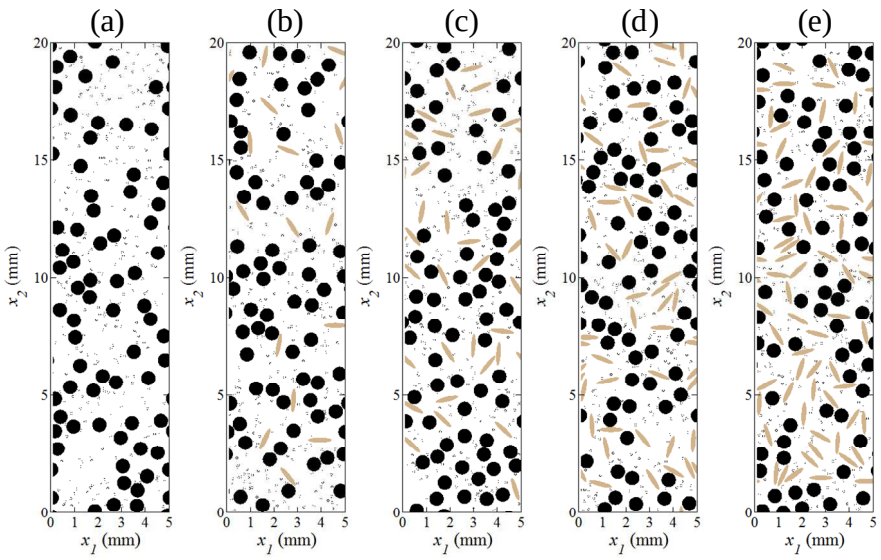

Figure 41. Microstructures with 20% aggregate, 2.5% porosity, and (a) 0% fibers, (b) 2.5% fibers, (c) 5% fibers, (d) 7.5% fibers, and (e) 10% fibers.

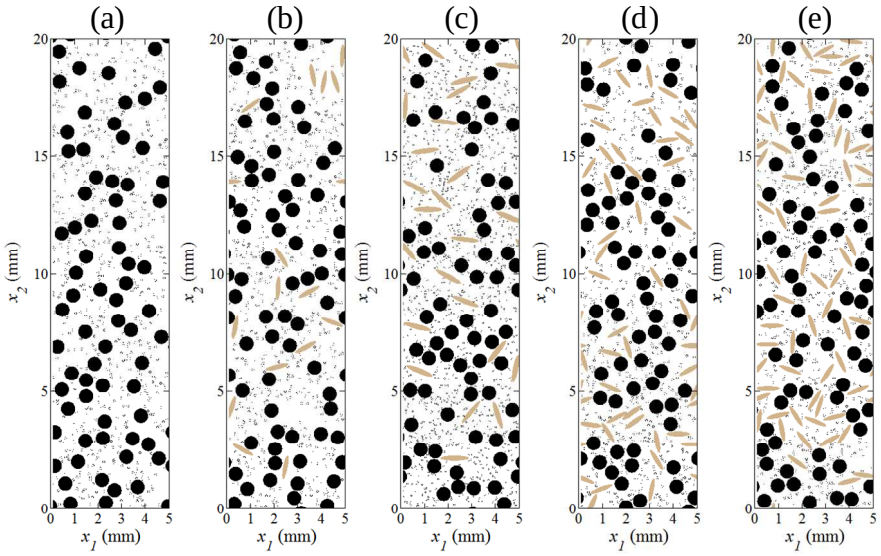

Figure 42. Microstructures with 20% aggregate, 5% porosity, and (a) 0% fibers, (b) 2.5% fibers, (c) 5% fibers, (d) 7.5% fibers, and (e) 10% fibers.

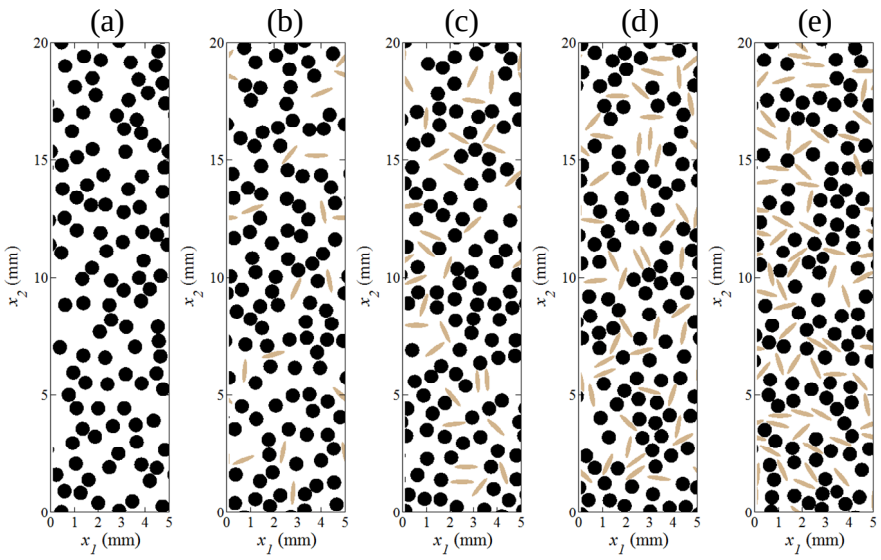

Figure 43. Microstructures with 30% aggregate, 0% porosity, and (a) 0% fibers, (b) 2.5% fibers, (c) 5% fibers, (d) 7.5% fibers, and (e) 10% fibers.

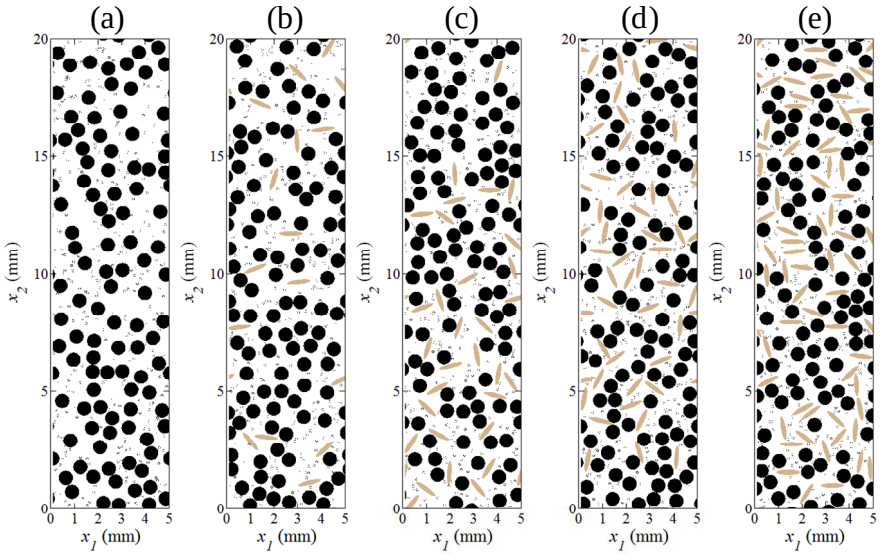

Figure 44. Microstructures with 30% aggregate, 2.5% porosity, and (a) 0% fibers, (b) 2.5% fibers, (c) 5% fibers, (d) 7.5% fibers, and (e) 10% fibers.

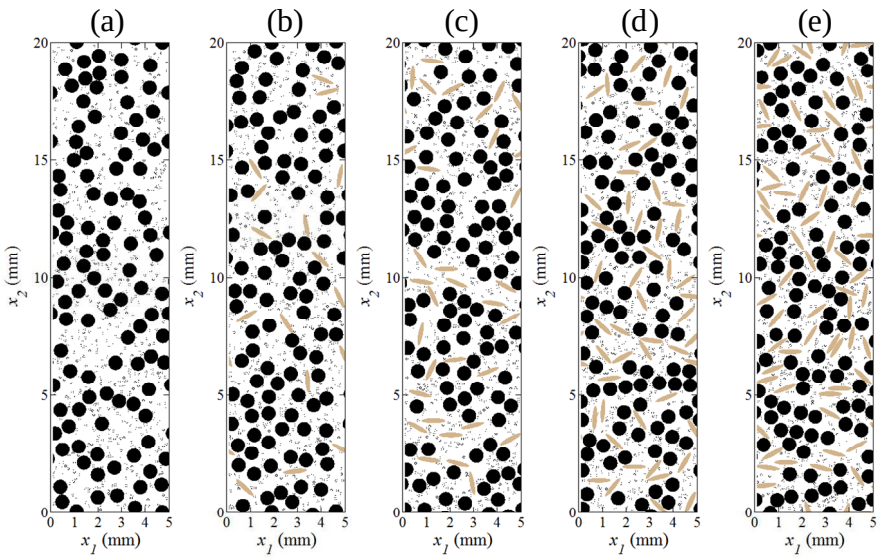

Figure 45. Microstructures with 30% aggregate, 5% porosity, and (a) 0% fibers, (b) 2.5% fibers, (c) 5% fibers, (d) 7.5% fibers, and (e) 10% fibers.

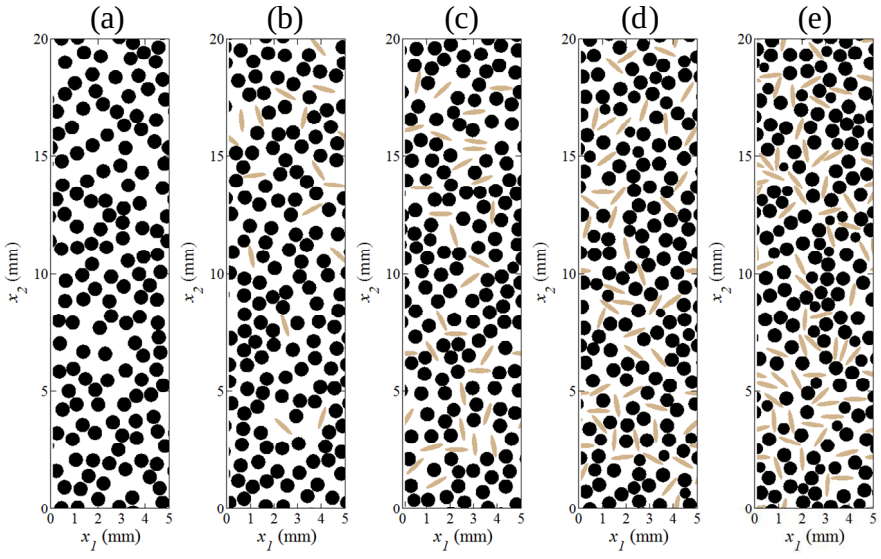

Figure 46. Microstructures with 40% aggregate, 0% porosity, and (a) 0% fibers, (b) 2.5% fibers, (c) 5% fibers, (d) 7.5% fibers, and (e) 10% fibers.

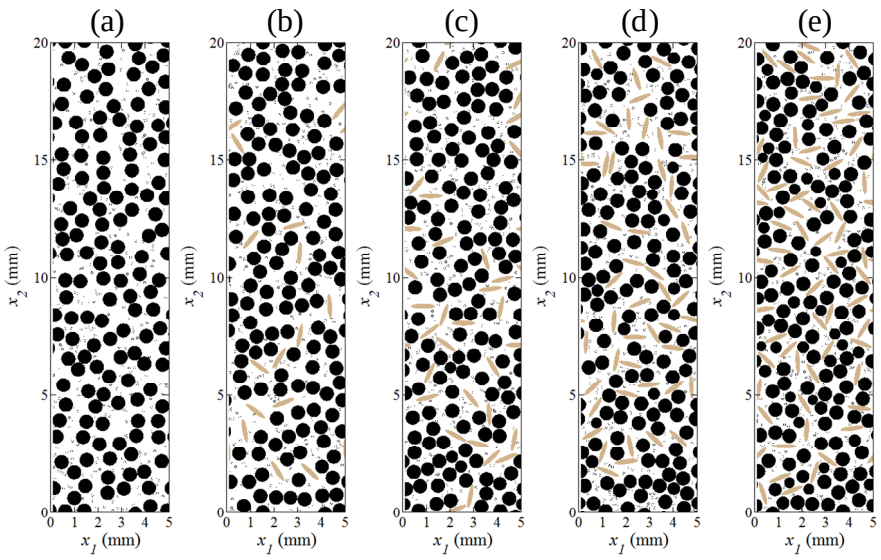

Figure 47. Microstructures with 40% aggregate, 2.5% porosity, and (a) 0% fibers, (b) 2.5% fibers, (c) 5% fibers, (d) 7.5% fibers, and (e) 10% fibers.

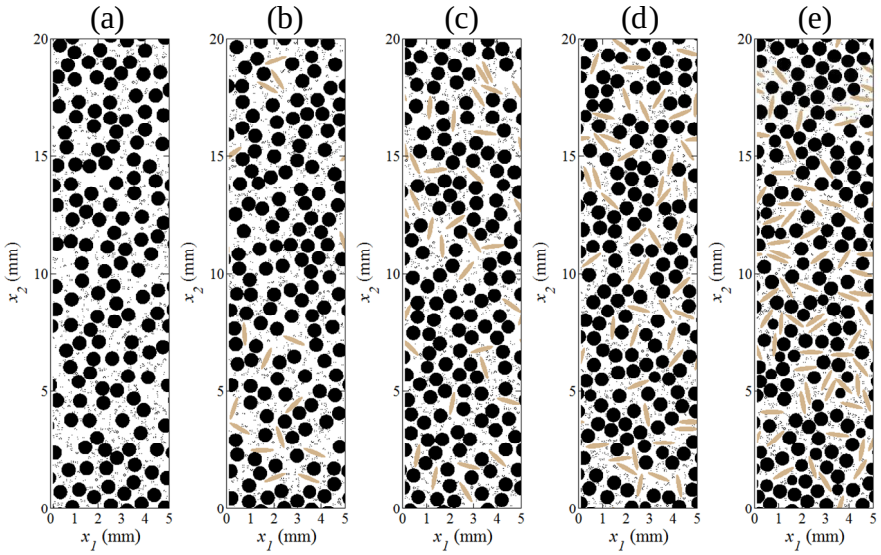

Figure 48. Microstructures with 40% aggregate, 5% porosity, and (a) 0% fibers, (b) 2.5% fibers, (c) 5% fibers, (d) 7.5% fibers, and (e) 10% fibers.

REFERENCES

1. Rong, Z., W. Sun, and Y. Zhang, *Dynamic compression behavior of ultra-high performance cement based composites.* International Journal of Impact Engineering, 2010. **37**(5): p. 515-520.

2. Sun, W., and J. Lai, *Dynamic mechanical behavior and durability of ultra high-performance cementitious composite.* Key Engineering Materials, 2009. **400**: p. 3-15.

3. Schleyer, G.K., S.J. Barnett, S.G. Millard, and G. Wright, *Modeling the response of UHPFRC panels to explosive loading.* In International Conference on Structures under Shock and Impact. 2010. Tallinn, Estonia: WIT Press.

4. Rebentrost, M., and G. Wight. *Behavior and resistance of ultra high-performance concrete to blast effects.* In Second International Symposium on Ultra High-Performance Concrete. 2008. Kassel, Germany: Kassel University Press.

5. Cavil, B., M. Rebentrost, and V. Perry. *Ductal - An ultra-high performance material for resistance to blast and impacts.* In 1st Specialty Conference on Disaster Mitigation. 2006. Calgary, Alberta, Canada.

6. Wang, J.-A.J., C.H. Mattus, and F. Ren, DHS counter improvised explosive device effects basic research. 2010. Vicksburg, MS: U.S. Army Engineer Research and Development Center.

7. Mroz, Z., and M. Angelillo. *Rate-Dependent Degradation Model for Concrete and Rock.* In International Symposium on Numerical Models in Geomechanics. 1982. Zurich.

8. Voyiadjis, G.Z., and Z.N. Taqieddin, *Elastic plastic and damage model for concrete materials: Part I - theoretical formulation.* International Journal of Structural Changes in Solids, 2009. **1**(1): p. 31-59.

9. Fanella, D., and D. Krajcinovic, *A micromechanical model for concrete in compression.* Engineering Fracture Mechanics, 1988. **29**(1): p. 49-66.

10. Tu, Z., and Y. Lu, *Evaluation of typical concrete material models used in hydrocodes for high dynamic response simulations.* International Journal of Impact Engineering, 2009. **36**(1): p. 132-146.

11. Park, S.W., Q. Xia, and M. Zhou, *Dynamic behavior of concrete at high strain rates and pressures: II. numerical simulation.* International Journal of Impact Engineering, 2001. **25**(9): p. 887-910.

12. Aragao, F.T.S., Y. Kim, J. Lee, and D. Allen, *Micromechanical model for heterogeneous asphalt concrete mixtures subjected to fracture failure.* Journal of Materials in Civil Engineering, 2011. **23**(1): p. 30-38.

13. Xu, Z., H. Hao, and H.N. Li, *Mesoscale modelling of fibre reinforced concrete material under compressive impact loading.* Construction and Building Materials, 2012. **26**(1): p. 274-288.

14. Lammi, C., D. McDowell, and M. Zhou, *Computation of the mesoscale dynamic fracture and dissipation behavior of concrete.* Manuscript submitted for publication. 2011.

15. Ellis, B., D. McDowell, and M. Zhou, *Energy dissipation and evolving strength of ultra-high-performance fiber-reinforced concrete (UHPFRC).* In 3rd International Symposium on Ultra-High Performance Concrete and Nanotechnology for High Performance Construction Materials. 2012. Kassel, Germany.

16. Flynn, D.R., *Response of High Performance Concrete to Fire Conditions: Review of Thermal Property Data and Measurement Techniques.* 1998. Gaithersburg, MD: National Institute of Standards and Technology.

17. Morsy, M.S., S.H. Alsayed, and M. Aqel, *Effect of elevated temperature on mechanical properties and microstructure of silica flour concrete.* International Journal of Civil & Environmental Engineering, 2010. **10**(1): p. 1-6.

18. Omer, A., *Effects of elevated temperatures on properties of concrete.* Fire Safety Journal, 2007. **42**(8): p. 516-522.

19. Naus, D.J., A Compilation of Elevated Temperature Concrete Material Property Data and Information for Use in Assessments of Nuclear Power Plant Reinforced Concrete Structures. 2010. Oak Ridge, TN: Oak Ridge National Laboratory.

20. Handoo, S.K., S. Agarwal, and S.K. Agarwal, *Physiochemical, mineralogical, and morphological characteristics of concrete exposed to elevated temperatures.* Cement and Concrete Research, 2002. **32**(7): p. 1009-1018.

21. Lammi, C., D. McDowell, and M. Zhou. *Prediction of damage initiation in ultra high-performance concrete during rapid heating.* In U.S. National Congress on Computational Mechanics. 2011. Minneapolis, MN.

22. Farnam, Y., S. Mohammadi, and M. Shekarchi, *Experimental and numerical investigations of low velocity impact behavior of high-performance fiber-reinforced cement based composite.* International Journal of Impact Engineering, 2010. **37**(2): p. 220-229.

23. Bencardino, F., L. Rizzuti, G. Spadea, and R. Swamy, *Stress-strain behavior of steel fiber-reinforced concrete in compression.* Journal of Materials in Civil Engineering, 2008. **20**(3): p. 255-263.

24. ABAQUS Theory Manual. 2010. Providence, RI: Simulia.

25. Drucker, D.C., and W. Prager, *Soil mechanics and plastic analysis or limit design.* Quarterly of Applied Math, 1952. **10**: p. 157-165.

26. Swamy, V.S., B. Sundman, and J. Zhang, *A thermodynamic assessment of the silica phase diagram.* Journal of Geophysical Research, 1994. **99**: p. 8.

27. Calderon, E., M. Gauthier, F. Decremps, G. Hamel, G. Syfosse, and A. Polian, *Complete determination of the elastic moduli of a-quartz under hydrostatic pressure up to 1 GPa: an ultrasonic study.* Journal of Physics: Condensed Matter, 2007. **19**: p. 1-13.

28. Zhou, Y., *An experiment study of quartz-coesite transition at differential stress.* Chinese Science Bulletin, 2005. **50**(5): p. 445-51.

29. Boettger, J.C., and S.P. Lyon, New Multiphase Equation of State for Polycrystalline Quartz. 1990. Los Alamos, NM: Los Alamos National Laboratory.

30. Bose, K., and J. Ganguly, *Quartz Coesite Transition Revisited.* American Mineralogist, 1995. **80**: p. 231-238.

31. Renner, J., A. Zerbian, and B. Stockhert, *Microstructures of synthetic polycrystalline coesite aggregates. The effect of pressure, temperature, and time.* Lithos, 1997. **41**: p. 169-184.

32. Hill, R., *The elastic behavior of a crystalline aggregate.* Proceedings of the Physical Society, Section A, 1952. **65**(5): p. 349-354.

33. Kimizuka, H., S. Ogata, and J. Li, *Hydrostatic compression and high-pressure elastic constants of coesite silica.* Journal of Applied Physics, 2008. **103**(053506): p. 1-4.

34. Blacic, J.D., and J.M. Christie, *Plasticity and hydrolitic weakening of quartz single crystals.* Journal of Geophysical Research., 1984. **89**(B6): p. 4223-4239.

35. Abaqus v6.10 Theory Manual. 2010. Providence, RI: Simulia.

36. Zhou, X.Q., V.A. Kuznetsov, H. Hao, and J. Waschl, *Numerical prediction of concrete slab response to blast loading.* International Journal of Impact Engineering, 2008. **35**(10): p. 1186-1200.

37. Li, V., *Determination of interfacial debond mode for fiber-reinforced cementitious composites.* Journal of Engineering Mechanics, 1994. **120**(4): p. 707-720.

38. Shen, B., and G.H. Paulino, *Identification of cohesive zone model and elastic parameters of fiber-reinforced cementitious composites using digital image correlation and a hybrid inverse technique.* Cement and Concrete Composites, 2011. **33**(5): p. 572-585.

39. Camanho, P.P., C.G. Davila, and M.F. de Moura, *Numerical simulation of mixed-mode progressive delamination in composite materials.* Journal of Composite Materials, 2003. **37**(16): p. 1415-1438.

40. Benzeggagh, M.L., and M. Kenane, *Measurement of mixed-mode delamination fracture toughness of unidirectional glass/epoxy composites with mixed-mode bending apparatus.* Composites Science and Technology, 1996. **56**(4): p. 439-449.

41. Camacho, G.T., and M. Ortiz, *Computational modelling of impact damage in brittle materials.* International Journal of Solids and Structures, 1996. **33**(20-22): p. 2899-2938.

42. Building Code Requirements for Structural Concrete (ACI 318-95). 1995. Farmington Hills, MI: American Concrete Institute. p. 369.

43. Sayers, C.M., and M. Kachanov, *A simple technique for finding effective elastic constants of cracked solids for arbitrary crack orientation statistics.* International Journal of Solids and Structures, 1991. **27**(6): p. 671-680.

44. Homand, F., D. Hoxha, T. Belem, M. Pons, and N. Hoteit, *Geometric analysis of damaged microcracking in granites.* Mechanics of Materials, 2000. **32**(6): p. 361-376.